X-RAY ABSORPTION AND EMISSION SPECTROSCOPY OF MANGANESE COMPLEXES RELEVANT TO PHOTOSYSTEM II

A Dissertation

Presented to the Faculty of the Graduate School

of Cornell University

In Partial Fulfillment of the Requirements for the Degree of

Doctor of Philosophy

by

Martha Anne Beckwith

January 2013

X-RAY ABSORPTION AND EMISSION SPECTROSCOPY OF MANGANESE COMPLEXES RELEVANT TO PHOTOSYSTEM II

Martha Anne Beckwith, Ph. D.

Cornell University 2013

A series of high-spin Mn monomers has been investigated by Mn Kβ x-ray emission spectroscopy (XES) and by Mn K-edge x-ray absorption spectroscopy (XAS). The XES and XAS were coupled with density functional theory (DFT) calculations. The XES Kβ main lines are dominated by 3p-3d exchange correlation effects and the DFT calculations show that the valence to core spectra are dominated by Mn *n*p to 1s electric dipole allowed transitions, and are sensitive to metal spin state, oxidation state, ligand identity, and metal-ligand bond lengths. The time-dependent DFT (TDDFT) calculations reveal that all experimentally observed XAS pre-edge features correspond either to Mn 1s to 3d transitions, or to metal-to-ligand charge transfer features that correspond to transitions into empty π* orbitals of either π-donor or π-acceptor ligands. The ability of TDDFT to reproduce the experimentally observed features at the correct relative energies depends on the nature of the transition. XAS, XES, and DFT calculations were also used to evaluate the protonation states of the $(\mu\text{-}O)_2$ bridges in a $[Mn_2(IV)(\mu\text{-}O)_2(salpn)_2]$ dimer. The XAS spectra exhibit distinct differences in the pre-edge region while maintaining the same edge energy, and the XES valence to core regions show significant changes in peak position and intensity upon protonation, particularly in the satellite region. The most intense pre-edge features in the XAS result from transitions into the unoccupied orbitals of local e_g character, while the $K\beta_{2,5}$ and satellite peaks in the XES arise primarily from ligand 2p to Mn 1s and ligand 2s to Mn 1s transitions, respectively. The extended x-ray absorption fine structure (EXAFS), and the corresponding first principle calculated EXAFS, were also examined for another series of

seven Mn monomers and dimers. The first shell distances are generally well predicted, although there are larger variations in the multiple scattering contributions. The largest deviations between calculated and experimental EXAFS are in the Debye-Waller (DW) factors, although slightly better agreement is obtained by modeling DW factors using the Dynamical Matrix method, as opposed to the more traditional Correlated Debye method. These findings have important implications for applications to manganese active sites in biological and chemical catalysis.

BIOGRAPHICAL SKETCH

Martha Anne Beckwith received her B. A. degree from Goucher College in Towson, Maryland in 2008, with a major in Chemistry and a minor in Music. In the summer of 2007 she conducted research in interstellar ice chemistry at the Sackler Laboratory at Leiden Observatory, Leiden, the Netherlands, after which she completed her honors thesis project at Goucher College under the direction of Dr. Scott Sibley studying insulin aggregation kinetics. She received her M. S. in Chemistry from Cornell University in January 2011 while working with Dr. Serena DeBeer.

For my family.

ACKNOWLEDGMENTS

There are many people that I would like to thank for their support and encouragement throughout the course of my doctoral work. First and foremost, I would like to thank my advisor, Dr. Serena DeBeer, whose steadfast encouragement and enthusiasm were invaluable as I was conducting my research. My remaining committee members, Drs. H. Floyd Davis and Brian Crane, also deserve thanks, particularly Floyd Davis, who was very kind and supportive when I decided to switch to Serena's group early on in my graduate school career.

I would also like to thank the graduate students, and former and current postdocs, in the DeBeer group: Chris, Chantal, Chandru, Kyle, Mario, Fred, and Vlad, for the interesting scientific, and often philosophical, discussions in the office that brought new perspectives to my research. Dr. Frank Neese, as well as two members of his group, Michael and Vera, deserves acknowledgment for helping me with DFT and many of the theoretical aspects of my doctoral work. I'd like to thank my other collaborators as well: Drs. Carole DuBoc and Marie-Noëlle Collomb for synthesizing the complexes for which I obtained spectroscopic data, the beamline scientists at SSRL and ESRF for help during data collection, Dr. Ken Finkelstein at CHESS for teaching me about the XES experimental setup, Dr. Junko Yano for providing the XAS and XES data of the salpn dimers and the EXAFS data of the OEC, and Dr. William Ames and Fernando D. Vila for help with EXAFS data analysis.

Last but not least, I would especially like to thank my family: my mother, father, and brother, without whose love and support throughout my life would this doctoral work have been possible.

TABLE OF CONTENTS

LIST OF FIGURES

LIST OF FIGURES (CONTINUED)

LIST OF FIGURES (CONTINUED)

LIST OF FIGURES (CONTINUED)

LIST OF TABLES

LIST OF ABBREVIATIONS

XAS = X-ray Absorption Spectroscopy

XES = X-ray Emission Spectroscopy

EXAFS = Extended X-ray Absorption Fine Structure

XANES = X-ray Absorption Near-Edge Structure

XRD = X-ray Diffraction

ESRF = European Synchrotron Radiation Facility

SSRL = Stanford Synchrotron Radiation Laboratory

OEC = Oxygen Evolving Complex

PSII = Photosystem II

DFT = Density Functional Theory

TD-DFT (also abbreviated TDDFT) = Time-Dependent Density Functional Theory

SOC = Spin-Orbit Coupling

HF = Hartree-Fock

fosc = oscillator strength

MO = Molecular Orbital

MLCT = Metal-to-Ligand Charge Transfer

LMCT = Ligand-to-Metal Charge Transfer

EPR = Electron Paramagnetic Resonance

ENDOR = Electron Nuclear Double Resonance

IWAE = Intensity-Weighted Average Energy

DW = Debye-Waller

CD = Correlated Debye

DM = Dynamical Matrix

DMDW = Dynamical Matrix Debye-Waller

VDOS = Vibrational Density of States

FT = Fourier Transform

MS = Multiple Scattering

acac = acetyl acetonate

bpea = *N,N*-bis(2-pyridylmethyl)-ethylamine

Me_3-TACN = 1,4,7-trimethyl-1,4,7-triazacyclononane

salen = ethylenebis(salicylimine)

terpy = 2,2':6',2"-terpyridine

tbu_3terpy = 4,4',4"-tritert-butyl-2,2':6',2"-terpyridine

tolylterpy = 4'-(4-methylphenyl)-2,2':6',2"-terpyridine

phenylterpy = 4'-phenyl-2,2':6',2"-terpyridine

tpa = tris-2-picolylamine

LIST OF SYMBOLS

Z_{eff} = effective nuclear charge

k = photoelectron wavevector

$\chi(k)$ = EXAFS amplitude in k-space

S_0^2 = overall many-body amplitude factor

N = number of similar scatterers

$f_{eff}(k)$ = effective scattering amplitude

R = absorber-scatterer distance in Å

σ^2 = variance in absorber-scatterer distance, R

λ_k = mean free path of the photoelectron

ϕ_k = total phase shift for the photoelectron wave interaction with the absorber and scatterer

m_e = mass of an electron

E_0 = ionization threshold energy

h = Planck's constant

$\hbar = h/2\pi$

$\rho_R(\omega)$ = vibrational density of states

w_D = Debye frequency

θ_D = Debye temperature

c = Debye approximation to the speed of sound

$|Q_R\rangle$ = Lanczos seed state representing a normalized, mass-weighted displacement of atoms along the path *R*

D_{KL} = dynamical matrix of force constants (a.k.a. mass-weighted Hessian matrix)

$|\mathbf{k}\rangle$ = an eigenvector of the mass-weighted Hessian matrix

d_k = k'th eigenvalue of the mass-weighted Hessian matrix

ω = vibrational frequency

X_K = Cartesian displacement of atom *K* from the equilibrium position

LIST OF SYMBOLS (CONTINUED)

M_K = mass of atom K

E = total internal energy of the system

$\sigma^2_R(T)$ = Debye-Waller factor for a given pathway as a function of temperature

μ_R = reduced mass associated with the given scattering path R

D = total transition dipole moment

ψ_c = metal core-1s orbital

ψ_v = valence orbital

z_M = z-coordinate position operator measured relative to the metal center

f_{IF} = oscillator strength of a transition between the initial and final states $|I\rangle$ and $|F\rangle$

E_{IF} = transition energy between the initial and final states $|I\rangle$ and $|F\rangle$

α = fine structure constant

$\hat{\boldsymbol{\mu}}$ = electric dipole moment operator

$\widehat{\boldsymbol{M}}$ = magnetic dipole moment operator

$\hat{\boldsymbol{Q}}$ = electric quadrupole moment operator

CHAPTER ONE

Introduction

Manganese plays an essential role in catalyzing a number of important reactions such as alkane hydroxylation, olefin epoxidation, O-O bond formation, and O-O bond cleavage.[1-4] Biologically, Mn is also present in the active sites of enzymes such as Mn superoxide dismutase,[5] which is responsible for the breakdown of superoxide, and in a cofactor of *Chlamydia trachomatis* ribonucleotide reductase,[6] which catalyzes the reduction of ribonucleotides to deoxyribonucleotides, the building blocks of DNA. Another enzyme that contains manganese is the oxygen-evolving complex (OEC) of photosystem II (PSII), which possesses a Mn_4Ca cluster in its active site and is responsible for the photosynthetic water oxidation reaction that produces atmospheric oxygen as a byproduct in photosynthesis.[7]

Generally the small molecule catalysts are monomers or dimers (either homovalent or mixed valent dimers).[8, 9] The enzyme active sites mentioned above are also generally mononuclear (Mn superoxide dismutase)[10] or dinuclear (*Chlamydia trachomatis* ribonucleotide reductase contains one Mn ion and one Fe ion),[6] with the exception of the tetranuclear OEC. All of the complexes and enzymes mentioned above contain Mn(II), Mn(III), or Mn(IV) centers that undergo at least one oxidation or reduction during the reaction cycles that they catalyze. As such, the reaction cycles usually involve high-valent intermediates, such as Mn(V) porphyrins which, due to the integer spin state of the Mn(V) center, cannot be analyzed by certain spectroscopic techniques such as EPR. In all of these reactions, understanding the geometric and electronic structure of the Mn is important for understanding the transformations that take place. Specifically regarding PSII, methods that can provide information on changes in the ligand coordination environment, as well as the metal oxidation states, could elucidate the general understanding of PSII, and potentially also provide insight into understanding other biological and chemical catalysts that

contain Mn.

The Oxygen-Evolving Complex of Photosystem II

PSII is part of a complex network of proteins in plants that is responsible for the photosynthetic reactions that convert energy from sunlight into chemical energy. In addition to sunlight, the overall reaction also uses CO_2 and water, releasing oxygen as a product into the earth's atmosphere. The OEC of PSII catalyzes one of the "light reactions," by using four photons of sunlight to oxidize two water molecules into an oxygen molecule, four protons, and four electrons. Before the water oxidation reaction occurs, the Mn atoms in the OEC undergo a series of oxidations themselves via the sunlight photons. Only after the fourth oxidation of the OEC cluster does the water splitting reaction take place, after which the OEC returns to its original oxidation state, thus restarting the cycle. This oxidation cycle of the OEC is known as the Kok cycle,[11] depicted in Figure 1.1, and the successive oxidation states of the OEC cluster within the Kok cycle are numbered S_0-S_4, where the subscript indicates the number of stored oxidation equivalents. The electronic structures of the S_0-S_3 states have been experimentally characterized, while the nature of the S_4 state remains elusive.

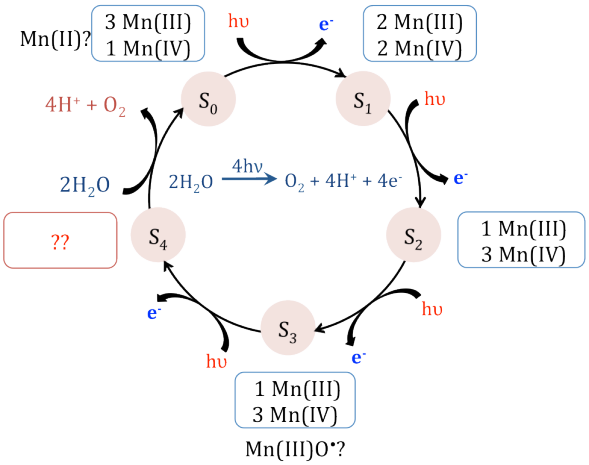

Figure 1.1. Depiction of the Kok cycle with the photosynthetic water oxidation reaction in the center. The known Mn oxidation states are given for each S-state.

After the initial discovery of the Kok cycle around 1970, many of the first studies of the geometric structure of the OEC consisted of extended x-ray absorption fine structure (EXAFS)

experiments of the various S-states, with one of the earliest being an EXAFS study of the S_1 state.[12] From the Mn EXAFS, researchers concluded that the OEC contained multiple Mn-O interactions at distances of ~1.8 Å, Mn-Mn interactions at ~2.7 Å, and Mn-Ca interactions at ~3.3 Å.[13, 14] Ten structures for the OEC were proposed based on the EXAFS, ranging from many different "dimer of dimers" models with various oxo bridging motifs, to cubane-like models (Figure 1.2).[13]

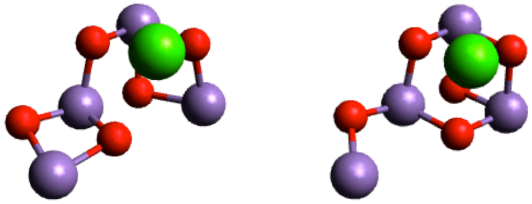

Figure 1.2. One example each of structures similar to the "dimer of dimers" and the cubane structural motifs proposed for the OEC based on EXAFS. Mn atoms are shown in purple, O atoms in red, and the Ca atom in green.

Early EPR studies of the S_2 state showed a distinct multiline signal, which was the first evidence for a multinuclear form of a manganese complex, and a signal at g = 4.1 was thought to arise from a Mn dimer exchange-coupled to a radical species.[15] From the ENDOR data of MeOH and NH_3 treated PSII in this same study, a "trimer-monomer" coupling scheme for the four Mn atoms was proposed.

Much of this ambiguity concerning the OEC structure was reduced in 2001, when the first XRD structure of the OEC was obtained at 3.8 Å resolution.[16] This XRD, along with even higher resolution structures obtained a few years later (3.5 Å in 2004[17] and 3.0 Å in 2005[18]), allowed for many of the models proposed based on early EXAFS experiments to be ruled out, and instead a "3+1" model for the Mn atoms in the OEC was proposed, where the Mn atoms formed a pseudo Y shape in the cluster with the Ca atom above the plane formed by the four Mn atoms. Despite the XRD ruling out many of the earlier models however, the concern of the x-ray

radiation possibly damaging the PSII samples[19] during the XRD data collection prompted J. Yano's group to conduct a study of the polarized EXAFS of single crystals of the OEC in the S_1 state, taking care to minimize radiation damage of the samples during a series of difficult experiments.[20] By comparing these polarized EXAFS to those calculated using computational models, they proposed multiple plausible models similar to "dimer of dimers" models for the S_1 state. A few years later, when comparing the same polarized EXAFS data to calculated EXAFS of DFT geometry optimized OEC models, Batista and coworkers proposed a distorted cubane model with a "dangler" Mn atom as opposed to the models suggested by Yano et. al. that were similar to earlier proposed "dimer of dimers" models.[21]

Around the same time, computational models for the S_2 state were also proposed by the groups of Barber and Murray[22] that were similar to the model suggested by Batista, and by the group of Siegbahn[23] that agreed with the model proposed by Yano. In a recent computational study, Pantazis et. al. concluded that not only are both the Siegbahn model and the cubane model of Barber viable S_2 state structures, but that both structures potentially coexist in the S_2 state, and are likely interconvertible depending on the experimental conditions.[24] This result explains many of the experimental phenomena observed over the years, most notably that the EPR of the S_2 state contains both a characteristic multiline signal at g = 2.0, and a broader signal at g = 4.1. According to Pantazis et. al., these two signals are thought to arise from the structural motif similar to the Siegbahn model (g = 2.0 multiline sigal), and from the structure similar to the cubane model (g = 4.1 signal). The possibility of interconversion between the two models also suggests that the experimental EXAFS of the S_2 state may reflect the coexistence of the two models, allowing both to be consistent with the same experimental EXAFS data. However, because the two groups of Yano and Batista reached different conclusions using the same experimental data prior to this computational study, the predictive ability of the calculated

EXAFS is explored in more detail in Chapter 5.

In 2011 Umena et. al. obtained an XRD of the OEC at 1.9 Å resolution.[25] Here, the positions of all four of the Mn atoms and the Ca atom were obtained with certainty, as well as much of the surrounding protein structure, and the obtained structure is similar to the earlier proposed "distorted cubane" structures. In addition, the positions of four ligated water molecules were proposed near the Ca atom and the "dangler" Mn atom. Despite the high resolution, there is still some ambiguity in the proposed structure because the structure is thought to correspond to a reduced form of the OEC due to x-ray damage, and the positions of the oxygen atoms cannot be reliably obtained at 1.9 Å resolution. As such, there is some question as to the protonation state and position of one of the bridging oxyens (labeled O5, Figure 1.3) that is located between the dangler Mn atom and the overall cubane structure created by the other Mn, Ca and O atoms. Because of the ambiguity in the position of this oxygen atom, both the "dimer of dimers" like models, as well as the distorted cubane models previously proposed are still viable options for the structure of the OEC.

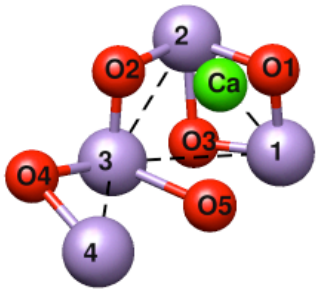

Figure 1.3. Depiction of the core of the OEC based on the 1.9 Å XRD.

While research over the years has thus made great strides in elucidating the structure of the OEC, many questions remain concerning the structure itself and the mechanism of the photosynthetic water oxidation reaction. Between the two viable models, those similar to the "dimer of dimers" or the cubane structure, which model best represents the active form of the OEC? What is the nature of the bridging oxygens in the OEC (O^{2-} vs. OH^- vs. OH_2)? Specifically what is the protonation state of O5 in the 1.9 Å XRD model, and where is it located

in the structure? What are the exact oxidation state assignments in all the S states of the Kok cycle? What is the nature of the S_4 state, both geometrically and electronically, and how does this influence the mechanism of water splitting and O-O bond formation? As stated earlier, methods that can provide information on changes in the ligand environment could elucidate our general understanding of PSII, and also provide insight into understanding other Mn containing biological and chemical catalysts.

X-ray Absorption Spectroscopy

A collection of methods that can potentially shed light on the questions above is x-ray spectroscopy. Like other spectroscopies, it can provide information about the electronic and geometric structure of matter through its interaction with x-ray photons. While many other spectroscopies involve excitations of valence level electrons, the energies of x-ray photons are such that core level electrons are excited. These spectroscopic methods are highly element-specific as a result: the excitation of an iron 1s electron, for example, occurs at energies hundreds of eV higher than those required to eject a manganese 1s electron.

X-ray absorption spectroscopy (XAS) is a technique that looks at the transitions of core level electrons to partially occupied or unoccupied valence energy levels. While it can be applied to many elements, the following discussion will be limited to XAS of transition metals. As the incident x-ray energy is scanned across the binding energy of the core electron of a metal, one sees a sharp increase in the absorption intensity, termed the "absorption edge." In the x-ray community nomenclature, XAS spectra involving transitions originating from the 1s level are known as K-edges, while those originating from the 2s and 2p levels are known as L-edges, and those originating from the 3s, 3p and 3d levels are known as M-edges. The sharp increase in intensity at the edge is due to dominantly dipole allowed transitions (1s to 4p transitions in the case of a first row transition metal K-edge). The oscillatory structure at higher energies after the edge jump is known as the EXAFS region, and will be discussed in more detail in the next section. In many cases, there is also a smaller amount of intensity at energies below the edge in

a region known as the pre-edge region, which corresponds to 1s to 3d transitions for first row transition metal K-edges (Figure 1.4). This decreased intensity compared to the edge results from the dominantly quadrupole allowed transitions that occur in this region. Although formally dipole forbidden, the pre-edge transitions can gain intensity via 3d-4p mixing.

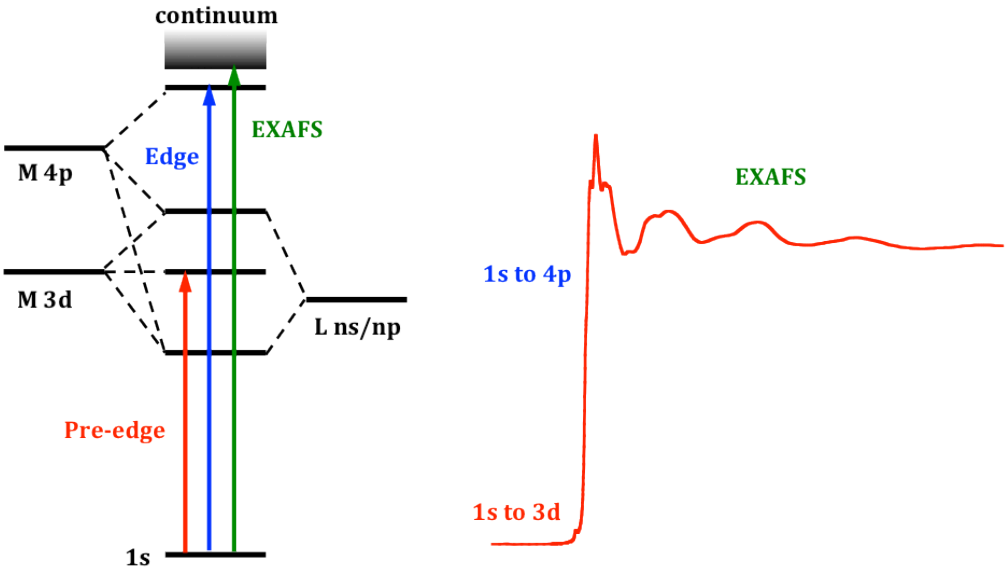

Figure 1.4. Energy level diagram depicting the relevant transitions in transition metal K-edge XAS (left) and the Mn K-edge XAS spectrum of [Mn(III)terpyCl$_3$] (right).

In general the edge shifts to higher energies upon oxidation of the metal, with a typical shift of ~1 eV per oxidation state increase (e.g. the edge of a Mn(III) compound will occur at an energy that is ~1 eV higher than that of a Mn(II) compound) due to the increased binding energy of the 1s electron for Mn(III) complexes relative to Mn(II) complexes. The pre-edge will generally shift as well, although the shift may not be as significant as that of the edge itself depending on how the interaction with coordinated ligands affects the metal valence levels. The pre-edge region in particular is also sensitive to changes in symmetry and metal coordination number. A five-coordinate complex, for example, will generally have larger pre-edge intensity than a six-coordinate complex with similar ligation (Figure 1.5) because the geometry of the five-coordinate complex allows for more Mn 4p mixing into the Mn 3d shell. This increases the amount of dipole allowed character for the transition, and thus increases the pre-edge intensity as

well. The pre-edge is particularly useful in transition metal K-edges because the partially occupied *n*d energy levels that are being examined in this region are involved in chemical bonding with coordinated ligands. The contributions to the XAS spectra, particularly contributions to the pre-edge region from site symmetry and metal coordination number, of Mn monomer and dimer model complexes will be discussed in more detail in Chapters 3 and 4.

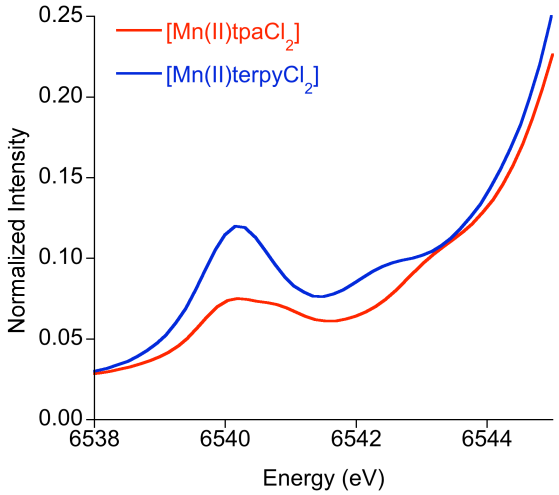

Figure 1.5. Pre-edges for the Mn K-edge XAS spectra of [Mn(II)tpaCl_2] (red) and [Mn(II)terpyCl_2] (blue). The five-coordinate complex [Mn(II)terpyCl_2] has a larger pre-edge intensity than the six-coordinate complex [Mn(II)tpaCl_2].

Mn XAS can aid in the electronic structure determination of the S-states of the OEC. The element specificity makes XAS an ideal technique for analyzing a complex protein such as the OEC, as the ligands immediately surrounding the Mn_4Ca cluster can be examined independent of the rest of the protein environment. All oxidation states and spin states of the Mn atoms can be probed using XAS (in contrast to EPR techniques, which have limited applicability to integer spin systems). In addition, both solid and dilute solution samples can be measured, which is advantageous for the analysis of proteins. The EXAFS region, discussed below, also provides information on the metrical structure of the OEC.

The EXAFS region

The oscillatory structure that occurs after the XAS edge jump is known as the EXAFS region. While the pre-edge and edge regions primarily give electronic structural information, the EXAFS

region reveals more information about the metrical structure of a compound. The EXAFS region corresponds to transitions of core electrons of the photoabsorber to the continuum (Figure 1.4). When a photoelectron has been excited to the continuum, it can be approximated as a free electron that propagates out from the photoabsorber and is subsequently backscattered by the electron density of the neighboring atoms in the molecule. As the incident photoelectron wavevectors encounter the nearby atoms and are reflected back, the constructive and destructive interference of the reflected waves with the incident waves (Figure 1.6) gives rise to the peaks and troughs seen in the EXAFS.

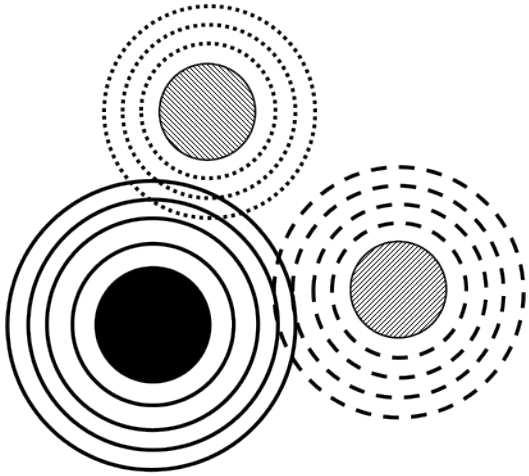

Figure 1.6. Diagram of the interference encountered between the incident photoelectron wavevectors (solid) propagating from the photoabsorber (solid black) and the backscattered wavevectors from neighboring atoms (dashed/dotted). Constructive and destructive interference between incident and backscattered wavevectors results in peaks and troughs seen in the EXAFS region of the XAS spectrum.

The EXAFS amplitude, $\chi(k)$, is modeled by[26]

$$\chi(k) = S_0^2 \sum_R N \frac{|f_{eff}(k)|}{kR^2} \sin(2kR + \phi_k) e^{-2kR/\lambda_k} e^{-2\sigma^2 k^2} \tag{1.1}$$

where S_0^2 is the overall many-body amplitude factor, N is the number of similar scatterers, $|f_{eff}(k)|$ is the effective scattering amplitude, R is the absorber-scatterer distance, $\exp(-2\sigma^2 k^2)$ is a Debye-Waller like factor, λ_k is the mean free path of the photoelectron, and ϕ_k is the total phase shift for the photoelectron wave interaction with the absorber and the scatterer. Using this

equation, information about a molecule's geometric structure can be obtained from the EXAFS data through the distance parameter, R, the coordination number parameter, N, and the Debye-Waller factor, $\exp(-2\sigma^2 k^2)$, which contains a term for the variance in absorber-scatter distance (σ^2). The EXAFS are expressed in terms of the photoelectron wavevector space, k, as opposed to energy space. The relationship between k ($Å^{-1}$) and energy (eV) is given by

$$k = \sqrt{\frac{2m_e(E-E_0)}{\hbar^2}} \approx \sqrt{0.262(E-E_0)} \tag{1.2}$$

where E_0 is the ionization threshold energy for the photoelectron and represents the point at which the EXAFS start (i.e. k=0). Expressing the EXAFS in k space can make data analysis difficult if one wishes to directly extract geometric information from the EXAFS, so they are often Fourier transformed to give spectra in R space (Å) so that distances in particular can be more easily obtained.

As the identity of the backscatterer will affect both the phase and the amplitude of the EXAFS signal, EXAFS can be used for determining the identity of atoms coordinated to the photoabsorber. However, because similar backscatterers will have similar phase and amplitude parameters, EXAFS cannot distinguish between carbon, nitrogen, and oxygen (however it can distinguish nitrogen and sulfur because of the greater differences in the electron density between these two atoms). In general, for first row elements, atomic numbers of Z±1 cannot be distinguished by EXAFS.

X-ray Emission Spectroscopy

A complementary technique to XAS is x-ray emission spectroscopy (XES). As in the earlier discussion of XAS, this description will be limited to XES of first row transition metals, although the technique can be applied to many elements as well. Like XAS, XES involves excitation of core electrons, however instead of observing transitions of the excited core electron into unoccupied energy levels, transitions of other electrons from occupied energy levels into the

core hole are examined. In this way XES is complementary to XAS such that a map of sorts of the occupied levels can be obtained from XES, while a similar map of the unoccupied levels can be obtained from XAS. A similar nomenclature used for XAS applies to XES (i.e. the 1s level is termed the K shell).

The most intense features in the XES spectrum arise from transitions from the metal 2p to the metal 1s level and are termed the Kα features. Two features are seen because of spin-orbit coupling of the 2p electron (i.e. the interaction between the electron's orbital angular momentum and its spin). Because the Kα features involve transitions from the 2p shell, which is not directly involved in chemical bonding and thus provides little useful chemical information, they will not be discussed further. Peaks corresponding to metal 3p to 1s transitions (Figure 1.7, left), termed the Kβ main line, occur at higher energies and are less intense than the Kα peaks. The splitting between the two Kβ main line peaks, the Kβ' (lower intensity) and $K\beta_{1,3}$ (higher intensity) features (Figure 1.7, center), is due to the 3p-3d exchange interaction.[27] While 3p spin-orbit coupling is present, the magnitude of the 3p-3d exchange is comparatively much greater, and thus the split between the Kβ' and $K\beta_{1,3}$ peaks is largely due to exchange. In some cases, the splitting between the $K\beta_1$ and $K\beta_3$ features due to spin-orbit coupling is observed, however for first row transition metals the individual $K\beta_1$ and $K\beta_3$ peaks cannot be resolved because of the much smaller magnitude of the 3p spin-orbit coupling. The highest energy and least intense features are termed the Kβ" and $K\beta_{2,5}$ features, collectively known as the valence to core region. They arise mainly from ligand ns and np to metal 1s transitions, and as such are much less intense than the Kβ main line, however they gain intensity through metal np mixing into the valence orbitals.[28, 29]

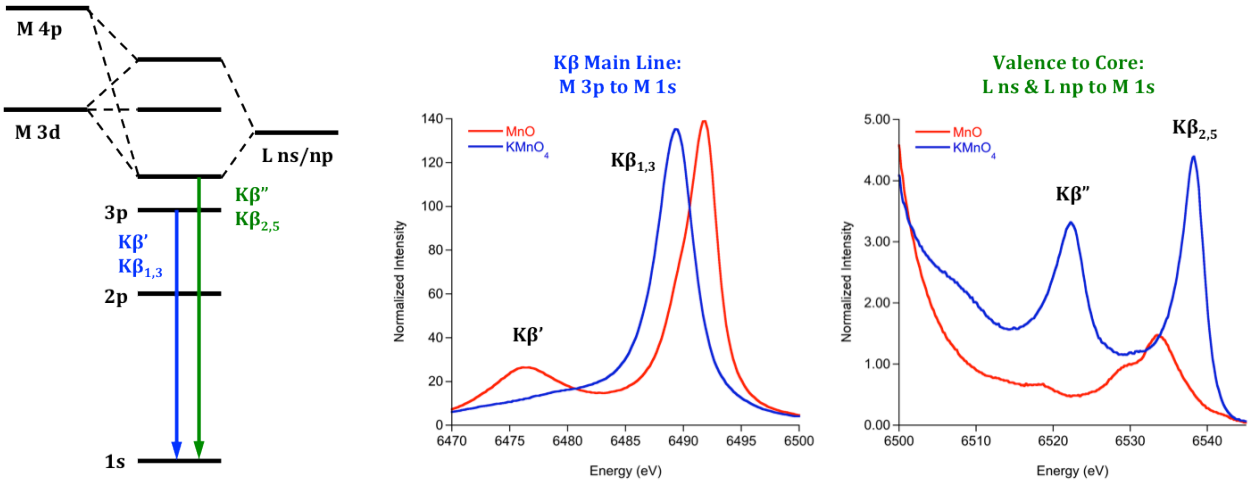

Figure 1.7. Energy level diagram depicting the relevant transitions in transition metal Kβ XES (left) and Kβ main line (center) and valence to core region (right) of the Mn XES spectra of MnO (red) and $KMnO_4$ (blue). The Kβ' and $K\beta_{1,3}$ features are clearly resolved in the main line of the high-spin complex MnO, whereas only the $K\beta_{1,3}$ feature is resolved in the low-spin complex $KMnO_4$.

In general, the Kβ main line is used as a fingerprint for the spin state of the metal. For high spin complexes both the Kβ' and $K\beta_{1,3}$ features are clearly resolved. For low spin complexes, however, the 3p-3d exchange splitting decreases and only the $K\beta_{1,3}$ feature is clearly seen, although it is more asymmetric due to contributions from the Kβ' feature (Figure 1.7, center). Because of this decreased 3p-3d exchange splitting, the $K\beta_{1,3}$ energies of low spin complexes occur at slightly lower values compared to high spin complexes, and the features may be slightly more intense for low spin complexes than for high spin complexes. This intensity difference between low spin and high spin complexes is more dramatic in the valence to core region (Figure 1.7, right).

Mn XES can aid in the structure determination of the S-states of the OEC for reasons similar to those for XAS: the element specificity, the absence of oxidation or spin state limitations, and the ability to measure solid and dilute solution samples. In addition, because the valence to core region provides a unique probe of ligand identity, XES can potentially further aid in the determination of the changes in the ligand environment immediately surrounding the Mn_4Ca cluster for each S-state.

XAS Data Collection

XAS experiments generally involve the use of synchrotron facilities that can provide a wide range of x-ray wavelengths for various types of experiments. Figure 1.8 diagrams a typical experimental setup for XAS at a synchrotron source. Before entering the "experimental hutch", where the experiment is conducted, the x-ray beam passes through a double crystal monochromator that is used for energy selection during the experiment. Ionization chambers placed before and after the sample are used to measure the absorption intensity of the sample during scanning (transmission mode). The sample is typically placed inside a liquid He flow cryostat that maintains the temperature at ~10 K to minimize photoreduction due to the x-ray beam. In the case of fluorescence detected XAS spectra (typical for dilute samples), a solid-state detector that measures the number of fluorescent photons is placed after the sample at a 90˚ angle to the incident x-ray beam. Kα fluorescence (2p to 1s hole fluorescence) is most commonly used for detection because Kα fluorescence is the most probable (i.e. intense) event. Here it is assumed that the number of fluoresced Kα photons is proportional to the number of absorbed photons. A metal foil placed between the second and third ionization chambers after the sample is measured simultaneously with the sample as a means of internal energy calibration for both transmission and fluorescence detection.

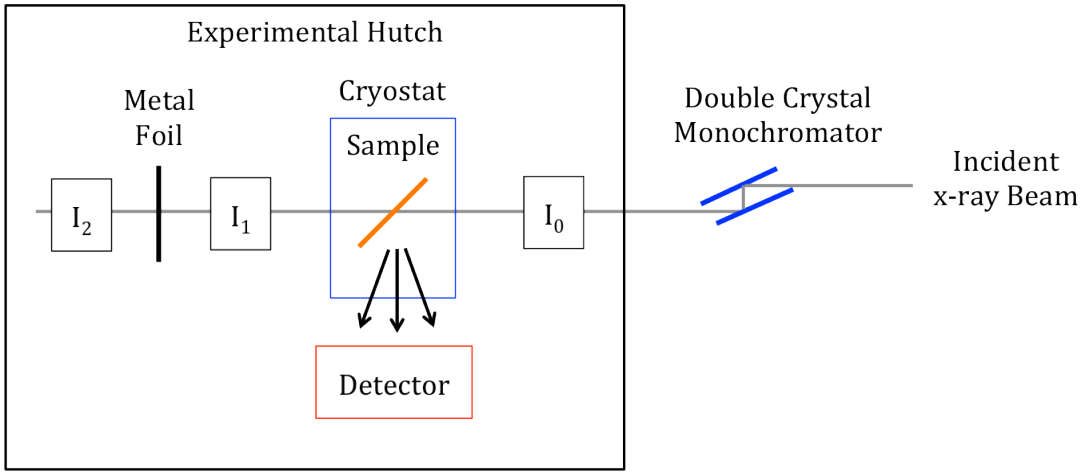

Figure 1.8. Depiction of the XAS experimental setup at a beamline at a synchrotron source.

XES Data Collection

The experimental setup for XES is similar to that for XAS, however there is a key difference in terms of the detector for XES. The detector setup consists of multiple analyzer crystals and a detector arranged in a Rowland geometry with the sample (Figure 1.9),[30] which allows the valence to core region to be resolved as well as the main line.

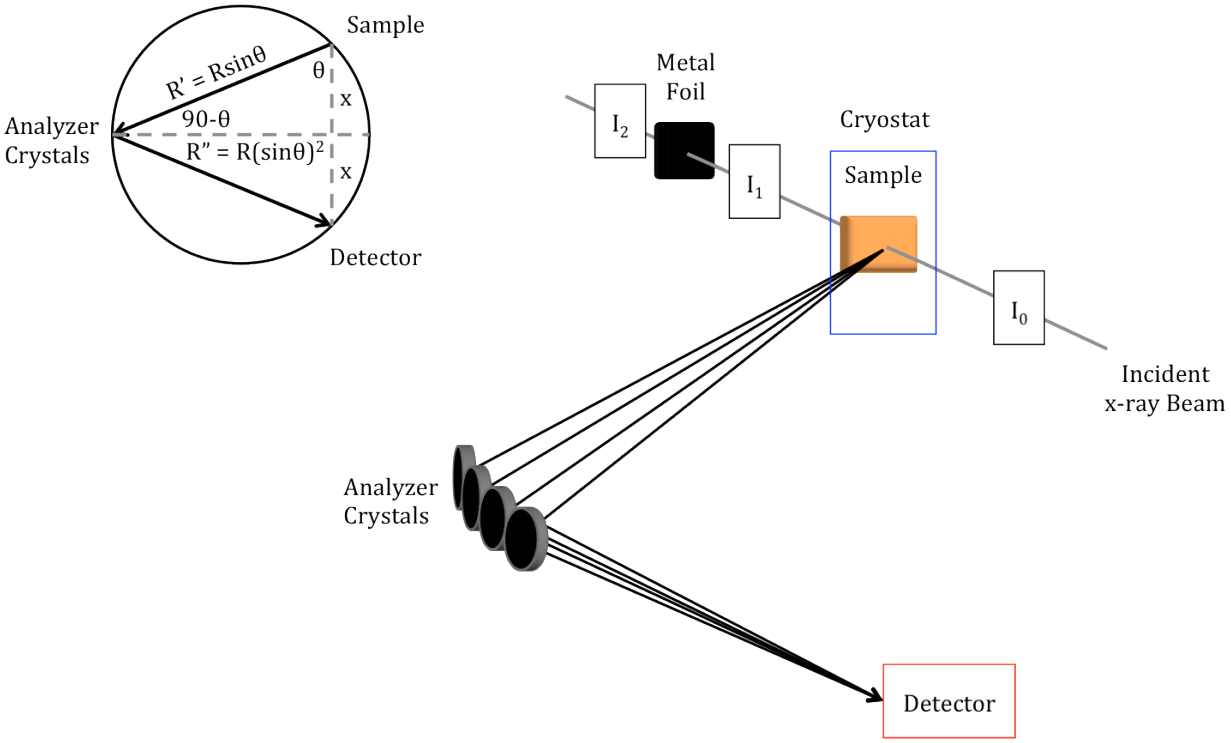

Figure 1.9. Depiction of the XES experimental setup utilizing the Rowland geometry for the sample, analyzer crystals and detector. In the simplified Rowland circle on the left, the incident x-ray beam is in a plane perpendicular to the plane of the Rowland circle.

The Rowland geometry arrangement of the sample, analyzer crystals, and detector allows for finer control over the fluorescence energy selection. The fluorescence energies are selected by moving both the analyzer crystals and the detector vertically. Because of Bragg's law, $n\lambda = 2d\sin\theta$, changing the analyzer crystal and detector positions changes the angle θ of the path of the fluorescent photons. This change in the angle thus changes the selected wavelength, λ, and by extension, the selected fluorescence energy.

In this work, XAS and XES have been applied to small molecule Mn complexes in order to

understand further how the spectra are affected by changes in metal oxidation state, coordination environment, site symmetry and ligand identity. Chapters 2 and 3 address the XES and XAS spectra of a series of Mn monomers. Chapter 4 discusses the XAS and XES of a series of Mn dimers that differ solely in the protonation states of the $(\mu\text{-}O)_2$ bridging ligands. Chapter 5 examines the ability of EXAFS to be used as a predictive tool for determining geometric structure when applied to a series of Mn monomers and dimers, as well as to proposed models for the OEC of PSII.

References

1. Gupta, K. C.; Sutar, A. K.; Lin, C. C., *Coord. Chem. Rev.* **2009,** *253*, 1926.
2. McLain, J. L.; Lee, J.; Groves, J. T., In *Biomimetic Oxidation Catalyzed by Transition Metal Complexes*, Meunier, B., Ed. Imperial College Press: London, 2000; pp 91.
3. Palucki, M.; Finney, N. S.; Pospisil, P. J.; Güler, M. L.; Ishida, T.; Jacobsen, E. N., *J. Am. Chem. Soc.* **1999,** *120*, 948.
4. Jin, N.; Lahaye, D. E.; Groves, J. T., *Inorg. Chem.* **2010,** *49*, 11516.
5. Fridovich, I., *Annu. Rev. Biochem.* **1995,** *64*, 97.
6. Jiang, W.; Yun, D.; Saleh, L.; Bollinger, J. M.; Krebs, C., *Biochemistry* **2008,** *47*, 13736.
7. Pecoraro, V. L.; Hsieh, W.-Y., In *Manganese and Its Role in Biological Processes*, Sigel, A.; Sigel, H., Eds. Marcel Dekker Inc: New York, 2000; Vol. 37, pp 429.
8. Das, S.; Brudvig, G. W.; Crabtree, R. H., *J. Am. Chem. Soc.* **2008,** *130*, 1628.
9. de Boer, J. W.; Browne, W. R.; Brinksma, J.; Alsters, P. L.; Hage, R.; Feringa, B. L., *Inorg. Chem.* **2007,** *46*, 6353.
10. Miller, A. F., *Curr. Opin. Chem. Biol.* **2004,** *8*, 162.
11. Kok, B.; Forbush, B.; McGloin, M., *Photochem. Photobiol.* **1970,** *11*, 457.
12. Yachandra, V. K.; Guiles, R. D.; McDermott, A.; Britt, R. D.; Dexheimer, S. L.; Sauer, K.; Klein, M. P., *Biochim. Biophys. Acta* **1986,** *850*, 324.
13. Derose, V. J.; Mukerji, I.; Latimer, M. J.; Yachandra, V. K.; Sauer, K.; Klein, M. P., *J. Am. Chem. Soc.* **1994,** *116*, 5239.
14. Yachandra, V. K.; Derose, V. J.; Latimer, M. J.; Mukerji, I.; Sauer, K.; Klein, M. P., *Science* **1993,** *260*, 675.
15. Peloquin, J. M.; Britt, R. D., *BBA-Bioenergetics* **2001,** *1503*, 96.
16. Zouni, A.; Witt, H. T.; Kern, J.; Fromme, P.; Krauss, N.; Saenger, W.; Orth, P., *Nature* **2001,** *409*, 739.
17. Ferreira, K. N.; Iverson, T. M.; Maghlaoui, K.; Barber, J.; Iwata, S., *Science* **2004,** *303*, 1831.
18. Loll, B.; Kern, J.; Saenger, W.; Zouni, A.; Biesiadka, J., *Nature* **2005,** *438*, 1040.
19. Yano, J.; Kern, J.; Irrgang, K. D.; Latimer, M. J.; Bergmann, U.; Glatzel, P.; Pushkar, Y.; Biesiadka, J.; Loll, B.; Sauer, K.; Messinger, J.; Zouni, A.; Yachandra, V. K., *Proc. Natl. Acad. Sci. U. S. A.* **2005,** *102*, 12047.
20. Yano, J.; Kern, J.; Sauer, K.; Latimer, M. J.; Pushkar, Y.; Biesiadka, J.; Loll, B.; Saenger, W.; Messinger, J.; Zouni, A.; Yachandra, V. K., *Science* **2006,** *314*, 821.
21. Sproviero, E. M.; Gascon, J. A.; McEvoy, J. P.; Brudvig, G. W.; Batista, V. S., *J. Am. Chem. Soc.* **2008,** *130*, 6728.
22. Barber, J.; Murray, J. W., *Philos. Trans. R. Soc. B-Biol. Sci.* **2008,** *363*, 1129.
23. Siegbahn, P. E. M., *Acc. Chem. Res.* **2009,** *42*, 1871.
24. Pantazis, D. A.; Ames, W.; Cox, N.; Lubitz, W.; Neese, F., *Angew. Chem. Int. Ed.* **2012,** *51*, 9935.
25. Umena, Y.; Kawakami, K.; Shen, J. R.; Kamiya, N., *Nature* **2011,** *473*, 55.
26. Rehr, J. J.; Kas, J. J.; Prange, M. P.; Sorini, A. P.; Takimoto, Y.; Vila, F., *C. R. Phys.* **2009,** *10*, 548.
27. Beckwith, M. A.; Roemelt, M.; Collomb, M. N.; DuBoc, C.; Weng, T.-C.; Bergmann, U.; Glatzel, P.; Neese, F.; DeBeer, S., *Inorg. Chem.* **2011,** *50*, 8397.
28. Lee, N.; Petrenko, T.; Bergmann, U.; Neese, F.; DeBeer, S., *J. Am. Chem. Soc.* **2010,** *132*, 9715.

29. Pollock, C. J.; DeBeer, S., *J. Am. Chem. Soc.* **2011,** *133*, 5594.
30. Glatzel, P.; Bergmann, U., *Coord. Chem. Rev.* **2005,** *249*, 65.

CHAPTER TWO

Manganese Kβ X-Ray Emission Spectroscopy as a Probe of Metal-Ligand Interactions[1]

Introduction

Manganese-containing active sites play essential roles in biological and chemical catalysis. Biologically, manganese enzymes are responsible for a wide variety of reactions, ranging from the breakdown of superoxide (by Mn superoxide dismutase)[1-3] to photosynthetic water oxidation (by the Mn_4Ca cluster in Photosystem II).[4, 5] In chemical catalysis, small molecule manganese complexes enable a range of oxidative transformations, including alkane hydroxylation and olefin epoxidation.[6-9] In all these reactions, there is fundamental interest in understanding the transformations that occur at the manganese active site, and hence an interest in directly probing the Mn electronic structure. EPR spectroscopy has proven to be a powerful tool,[10] particularly in the study of Photosystem II (PSII).[11-13] However the applicability of EPR to systems with integer ground state spin is limited. This motivates the development of other methods, such as x-ray absorption spectroscopy (XAS). Considerable effort has gone into the application of XAS to Mn systems, as all oxidation states and spin states of Mn may be probed by x-ray core level spectroscopy.[14-18] For PSII, this has allowed for spectra of the S_0 to S_3 states of the Mn_4Ca cluster to be obtained, thus providing significant insights into the oxidative transformations that occur in the cycle.[19-21] However, despite the advances reported in these studies, questions about the exact nature of some of the S-states remain, and there is a clear need for additional spectroscopic insights in order to fully assess changes in the electronic structure. In particular, a

[1] Adapted with permission from Beckwith, M. A.; Roemelt, M.; Collomb, M. N.; DuBoc, C.; Weng, T.-C.; Bergmann, U.; Glatzel, P.; Neese, F.; DeBeer, S., *Inorg. Chem.* **2011,** *50*, 8397. Copyright 2011 American Chemical Society.

method that allows one to better assess changes in the ligand environment could provide key insights into our understanding of PSII and would also generally benefit our understanding of biological and chemical catalysis by complexes that contain Mn.

A method that shows potential promise in this regard is Mn Kβ x-ray emission spectroscopy (XES).[22, 23] The so called Mn Kβ main line corresponds to a dipole allowed Mn 3p to 1s transitions, which exhibits pronounced sensitivity to spin state.[11, 24-26] To higher energy is the valence to core region, which corresponds to transitions from valence orbitals into the Mn 1s core hole.[27, 28] Recently, systematic studies of Fe Kβ XES spectra have shown that the intensity of the valence to core features are mediated by Fe *n*p mixing into the filled ligand orbitals.[29] The resultant spectra have a pronounced sensitivity to metal spin state, oxidation state, and identity of the bound ligand (including ionization state, protonation state, and hybridization).[29] Smolentsev et al. have carried out a limited subset of studies on Mn complexes,[30] which show parallel trends to the iron study. However, to the author's knowledge a detailed, systematic investigation of Mn complexes with varied oxidation states and ligand environments has not yet been reported in the literature. These studies are of particular interest, as Mn Kβ XES valence to core data are already available for the S_1 state of the Mn_4Ca cluster in PSII.[31] The data show that the S_1 state has several μ-oxo bridged Mn-O bonds, however at this stage only an empirical assessment of the data can be made. A more quantitative analysis of the data requires a systematic study of a range of compounds and correlation of these data to theory.

Here a systematic study of the Kβ XES spectra of sixteen high-spin mononuclear Mn(II), Mn(III) and Mn(IV) complexes (Chart 2.1 and Table 2.1) is presented. The oxidation and spin state contributions to both the Kβ main line and the valence to core region are assessed. While the spin state dependence of the Kβ main line has been previously investigated, to the author's knowledge the spin state contribution to the valence to core region has not been examined in

detail. In addition, the contributions of oxidation state and ligand identity to the valence to core region are investigated and quantitatively evaluated.

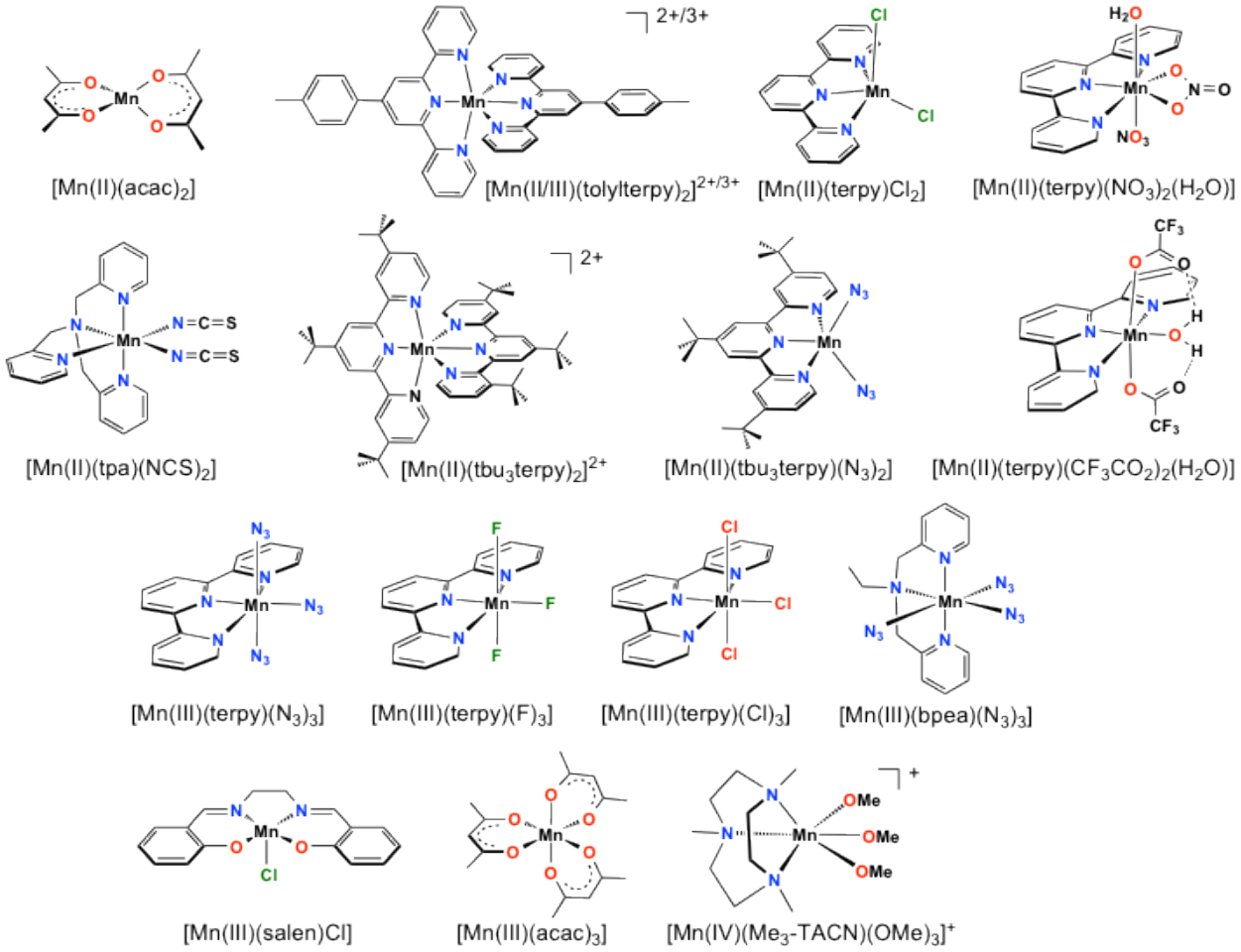

Chart 2.1. The sixteen high-spin mononuclear manganese complexes investigated in this study.

The experimental valence to core transitions are compared to those calculated using a straight-forward density functional theory (DFT) approach, as previously applied in Fe XES studies.[29] The strong correlation between experiment and theory indicates that these calculated spectra can be used for a quantitative analysis of valence orbital composition. This also allows the contributions of spin state, ligand identity, and metal-ligand bond lengths to be assessed in an *in silico* fashion. The potential of these methods for probing questions in biological manganese catalysis is highlighted.

Experimental

Sample preparation. [Mn(II)$(acac)_2$], [Mn(III)$(acac)_3$] and [Mn(III)(salen)Cl] were purchased from Strem Chemicals and used without further purification. All other manganese reference samples were synthesized according to published procedures by the groups of Drs. Carole Duboc and Marie-Noëlle Collomb.[32-43] The references for the syntheses and the crystal structures are provided in Table 2.1. The following abbreviations have been used for the ligands: acac = acetyl acetonate; bpea = *N,N*-bis(2-pyridylmethyl)-ethylamine; Me_3-TACN = 1,4,7-trimethyl-1,4,7-triazacyclononane; salen = ethylenebis(salicylimine); tbu_3terpy = 4,4',4"-tritert-butyl-2,2':6',2"-terpyridine; terpy = 2,2':6',2"-terpyridine; tolylterpy = 4'-(4-methylphenyl)-2,2':6',2"-terpyridine; tpa = tris-2-picolylamine (see also Chart 2.1). Samples were measured as powders, diluted in boron nitride, pressed into pellets and sealed into Al spacers with 38 micron Kapton tape. All samples were loaded into a liquid helium cryostat and maintained at a temperature of ~20 K throughout the course of data collection.

XES measurements. All XES data were obtained at beam line ID26 of the European Synchrotron Radiation Facility (ESRF). A pair of Si crystals in 311 reflection was used upstream for energy selection and was fixed at an incident energy of 6700 eV. The incident flux was 10^{13} photons/second in a 0.2 x 1.5 mm^2 beam footprint on the sample. Kβ x-ray emission spectra were measured using the 440 reflection of five spherically bent (R = 1m) Si crystal analyzers in combination with a silicon drift detector aligned in a Rowland geometry, as described previously.[30] The overall energy bandwidth of the x-ray emission spectrometer was 0.8 eV. The data were normalized with respect to the incident flux. The space between the sample, the spherical analyzers and the detector was filled with helium in order to minimize attenuation of the fluorescence. In order to assess the rate of photoreduction, short Kβ detected XANES scans were run to determine the acceptable dwell time per sample spot. For all samples data were

obtained on multiple spots. Only those scans which showed no evidence for photoreduction were included in the final averages. Both short and long scans of the XES data were obtained. The long scans included both the Kβ main line (6478-6550 eV) and the valence to core region, whereas the short scans (6505 – 6550 eV) included only the valence to core region.

The experimental spectra were obtained by first separately averaging long scans and short scans in PyMCA[44] and then merging the resultant average scans together to obtain the full spectra. For each of the averaged spectra, the total integrated area was set to a value of 1000, and the valence to core region was fit using the program EDG_FIT.[45] The background tail from the Kβ main line, and the valence to core features, were modeled using a combination of Gaussian and Lorenztian functions. The background from the Kβ main line was subtracted from the reported valence to core areas. The reported areas represent the best fit based on minimized error, with the standard deviations of all reasonable fits reported in parentheses (Table 2.1).

XES Calculations. All calculations have been carried out with ORCA quantum chemistry program package using the methods developed in reference 29. Geometry optimizations were performed starting from x-ray crystal structures (when available and as referenced in Table 2.1). The BP86 functional,[46, 47] the zero'th order regular approximation for relativistic effects (ZORA)[48] following the model potential implementation of van Wüllen[49] and the scalar-relativistically recontracted def2-TZVP(-f) basis set were used in all of these calculations.[50] Solvation effects were accounted for by the conductor-like screening model (COSMO)[51] using the dielectric constant of dichloromethane (ε = 9.08). A dense grid (ORCA Grid4) was used for the numerical integration of the exchange-correlation potential. All geometry optimizations except those of [Mn(II)(terpy)$(NO_3)_2(H_2O)$], [Mn(III)(salen)Cl], and (Mn(III)$(acac)_3$] were performed by Michael Roemelt.

All Mn K-edge XES calculations presented in this study have been conducted using the

theoretical protocol described above. In contrast to the previously described method for calculating XES spectra,[29] the molecular orbitals used were corrected for spin-orbit-coupling (SOC). The calculated XES spectra using SOC are similar to those without SOC in the region of interest for the complexes studied. The SOC operator is approximated by the spin-orbit mean-field method (SOMF)[52], resulting in SOC corrected orbital energies. For more information see reference 52 and the reference from which this chapter is adapted.[53]

Results and Discussion

Kβ XES Main Line Spectra.

Mn Kβ emission data were obtained for a series of high-spin mononuclear Mn(II) and Mn(III) complexes, in addition to one Mn(IV) complex, as summarized in Table 2.1. The Kβ main line corresponds to a Mn 3p to 1s transition and its energy should be affected by contributions from both 3p-3d exchange, variations in the effective nuclear charge (Z_{eff}) of the manganese centers, and perhaps also smaller contributions from SOC arising from the $3p^5$ final state configuration. The Kβ main line spectra for the complexes investigated in this study are given in Figures 2.1A to 2.1D. The energy positions of the intensity maxima of the $K\beta_{1,3}$ features are given in Table 2.1.

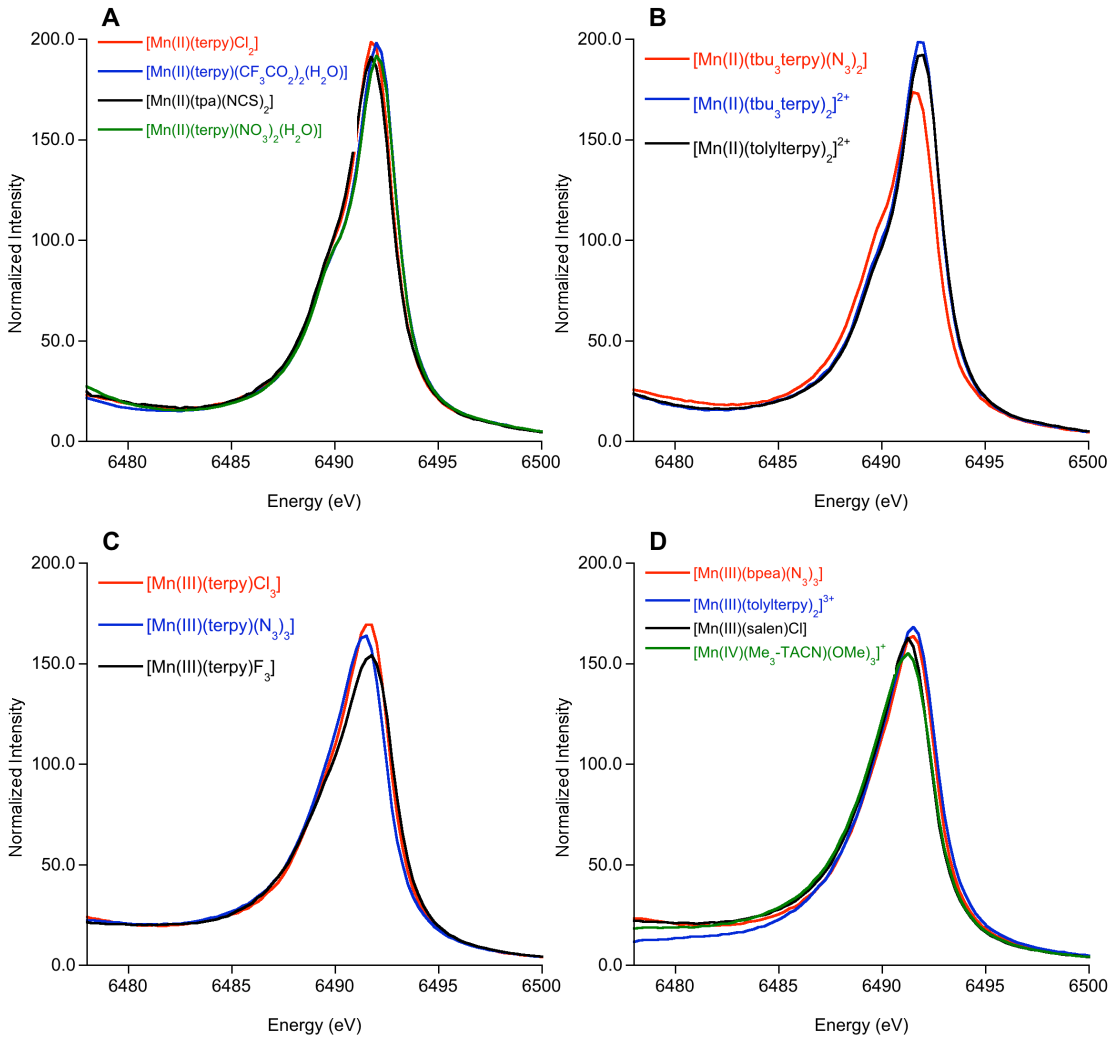

Figure 2.1. (A and B) XES Kβ main lines for Mn(II) complexes. (C and D) XES Kβ main lines for Mn(III) and Mn(IV) complexes.

Table 2.1. $K\beta_{1,3}$ peak energies, $K\beta_{2,5}$ intensity-weighted average energies and background-subtracted valence to core areas of the Mn model complexes studied.

Complex	$K\beta_{1,3}$ Energy (eV)[a]	$K\beta_{2,5}$ Energy (eV)[b]	Area (valence to core region)[c]	Reference[d]
		Mn(II) Complexes		
$[Mn(acac)_2]$	6491.85	6531.9 (0.01)	12.02 (0.41)	-
$[Mn(tolylterpy)_2]^{2+}$	6491.89	6533.04 (0.05)	16.12 (0.12)	42, 43
$[Mn(terpy)Cl_2]$	6491.83	6533.45 (0.02)	11.37 (0.09)	36
$[Mn(terpy)(NO_3)_2(H_2O)]$	6492.04	6532.47 (0.17)	13.20 (0.52)	32
$[Mn(tbu_3terpy)_2]^{2+}$	6491.87	6532.82 (0.09)	14.71 (0.64)	34
$[Mn(tbu_3terpy)(N_3)_2]$	6491.6	6532.31 (0.10)	18.36 (0.11)	39
$[Mn(terpy)(CF_3CO_2)_2(H_2O)]$	6492.03	6532.85 (0.01)	14.37 (0.13)	41
$[Mn(tpa)(NCS)_2]$	6491.76	6532.68 (0.01)	13.91 (0.16)	34
		Mn(III) Complexes		
$[Mn(acac)_3]$	6491.53	6531.62 (0.13)	17.47 (1.06)	-
$[Mn(tolylterpy)_2]^{3+}$	6491.48	6532.83 (0.01)	25.90 (0.31)	43
$[Mn(terpy)(N_3)_3]$	6491.42	6532.09 (0.01)	21.52 (0.18)	35
$[Mn(terpy)F_3]$	6491.71	6532.85 (0.04)	19.03 (0.75)	38
$[Mn(terpy)Cl_3]$	6491.63	6533.19 (0.15)	17.10 (0.55)	37
$[Mn(bpea)(N_3)_3]$	6491.43	6532.35 (0.01)	18.91 (0.04)	38
[Mn(salen)Cl]	6491.25	6532.15 (0.05)	21.01 (0.70)	-
		Mn(IV) Complexes		
$[Mn(Me_3\text{-}TACN)(OMe)_3]^{+}$	6491.25	6532.78 (0.04)	20.06 (0.70)	33, 40

[a] Estimated error in the $K\beta_{1,3}$ energy is ±0.1 eV.
[b] Intensity-weighted average energies were determined using the $K\beta_{2,5}$ region (6525 – 6540 eV). Satellite features in the < 6525 eV range are not included in the reported areas as these are generally poorly resolved from the background and thus have larger errors associated with the determination of the areas. The reported values for the energies and areas are those obtained from the best fit, with the standard deviations based on all reasonable fits reported in parentheses.
[c] Reported areas are out of 1000 units of normalized intensity.
[d] Synthesis and crystallographic structure references.

The Kβ' feature, which appears on the low energy side of the Kβ main line, could not be obtained due to constraints on the geometry imposed by the cryostat windows. As this region is not the primary focus of the current study the truncation of the data range does not significantly impact the reported data. However, it should be noted that the absence of the Kβ' feature may result in a slightly larger error in the normalized valence to core areas (*vide infra*). Even in the absence of the Kβ' feature, interesting trends may be observed in the $K\beta_{1,3}$ main line energies. As shown in Table 2.1, the $K\beta_{1,3}$ main line shifts to slightly lower energy upon oxidation of Mn(II) to Mn(III). This is most clearly illustrated by comparing the data of $[Mn(II)(tolylterpy)_2]^{2+}$ to that of $[Mn(III)(tolylterpy)_2]^{3+}$, which have Kβ main line energies of 6491.9 and 6491.5 eV,

respectively. This 0.4 eV decrease in energy is the result of two primary contributions: 1) the change in Z_{eff} upon oxidation (which should tend to *increase* the energy of the $K\beta_{1,3}$ main line, due to a greater stabilization of the Mn 1s orbital relative to the Mn 3p orbitals) and 2) the change in spin state from $S = 5/2$ for Mn(II) to $S = 2$ for Mn(III) (which will tend to *decrease* the 3d-3p exchange splitting, thus decreasing the $K\beta'$:$K\beta_{1,3}$ splitting and lowering the energy of the main line feature). The observed overall decrease in energy indicates that the exchange splitting is the larger contributor in these compounds, a trend generally observed for high spin Mn systems.

This observation is different from what has been observed for Fe Kβ emission data, where the $K\beta_{1,3}$ feature shifts to *higher* energy (by ~0.8 eV) upon oxidation of Fe(II) to Fe(III). This is correlated to the fact that for high spin Fe(II) oxidation results in an increase in spin state from $S = 2$ to $S = 5/2$. Thus for a high-spin Fe(II)/Fe(III) redox couple the Kβ main lines spin state and Z_{eff} effects have an additive effect upon oxidation, resulting in a larger overall increase in the Kβ main line energy, whereas for a high spin Mn(II)/Mn(III) redox couple these effects oppose each other. Based on these observations, one can *roughly* estimate the increased 3p-3d exchange contribution resulting from increasing the Mn spin state by one electron. Assuming that the contributions for an increase in Z_{eff} by one oxidation state are approximately equal for Fe and Mn then a ~0.2 eV increase in the Kβ main line energy to the Z_{eff} change at the metal is obtained. This then indicates a ~0.6 eV change due to an increase in spin state by one half unit of spin angular momentum brought about by an additional unpaired electron. This is reasonably consistent with the ~2 eV increase in energy observed on going from low spin ferrous or ferric complexes to the corresponding high spin complexes (i.e an increase of 4 in multiplicity). It should be noted, however, that these values are simply rough estimates to explain observed experimental trends in closely related molecular complexes, and additional factors, such as

metal-ligand covalency may also play a role.[54] However, the general trends indicate that the energies of Kβ main lines provide useful markers for changes in the spin state of a system, as also indicated previously.[23]

Kβ XES Valence to Core Spectra.

Figures 2.2A-B and 2C-D present the valence to core spectra for the Mn(II) and Mn(III) complexes, respectively, investigated in this study. Representative fits of the valence to core spectra of [Mn(II)(tbu_3terpy)(N_3)$_2$] and [Mn(III)(tolylterpy)$_2$]$^{3+}$ are shown in Figures 2.3 and 2.4. Table 2.1 reports the intensity-weighted average energies for the Mn XES valence to core spectra and the corresponding areas.

Valence to Core Energies. Upon oxidation of Mn(II) to Mn(III), there is a slight shift to lower energy when comparing complexes with identical ligands (Table 2.1). For example, on going from [Mn(II)(tolylterpy)$_2$]$^{2+}$ to [Mn(III)(tolylterpy)$_2$]$^{3+}$ the valence to core region of the spectra shifts down in energy by 0.2 eV. This shift is smaller than the shift in the Mn Kβ main line (~0.4 eV) for the same set of complexes and may reflect a slightly larger contribution from the change in Z_{eff} to the valence to core energies. The shift for the Mn complexes is again significantly smaller than what has been observed for Fe complexes, where an ~1.2 eV increase in energy is observed upon oxidation. The energy of the mononuclear Mn(IV) complex, [Mn(IV)(Me_3-TACN)($OMe)_3$]$^+$, falls within the range of the Mn(III) complexes, however, without a comparison to a complex in an analogous ligation sphere, a more quantitative assessment is not possible.

Valence to Core Areas. The experimental areas for the valence to core region span ~11-18 units of intensity for the Mn(II) complexes and increase to 17-26 units of intensity for the Mn(III) complexes. When comparing [Mn(II)(tolylterpy)$_2$]$^{2+}$ to [Mn(III)(tolylterpy)$_2$]$^{3+}$, an

increase in intensity by a factor of 1.6 is observed upon oxidation. This is attributed to the shorter Mn-ligand bond lengths which provide a mechanism for increased Mn *n*p mixing into the ligand orbitals.[29]

$[Mn(IV)(Me_3\text{-}TACN)(OMe)_3]^+$, however, does not show the most intense peaks in this region despite having the highest oxidation state. This likely reflects the relatively long average Mn(IV)-ligand bond lengths for this complex, which fall within the range of the Mn(III) complexes, thus resulting in comparable peak intensities.

It is again of interest to note that this is in contrast to previous observations for Fe valence to core XES spectra, where high-spin ferrous and ferric complexes exhibited similar areas, with only an ~10% increase in intensity upon oxidation. This in part reflects the more substantial structural change on going from Mn(II) to Mn(III), as the latter is subject to a large Jahn Teller distortion.

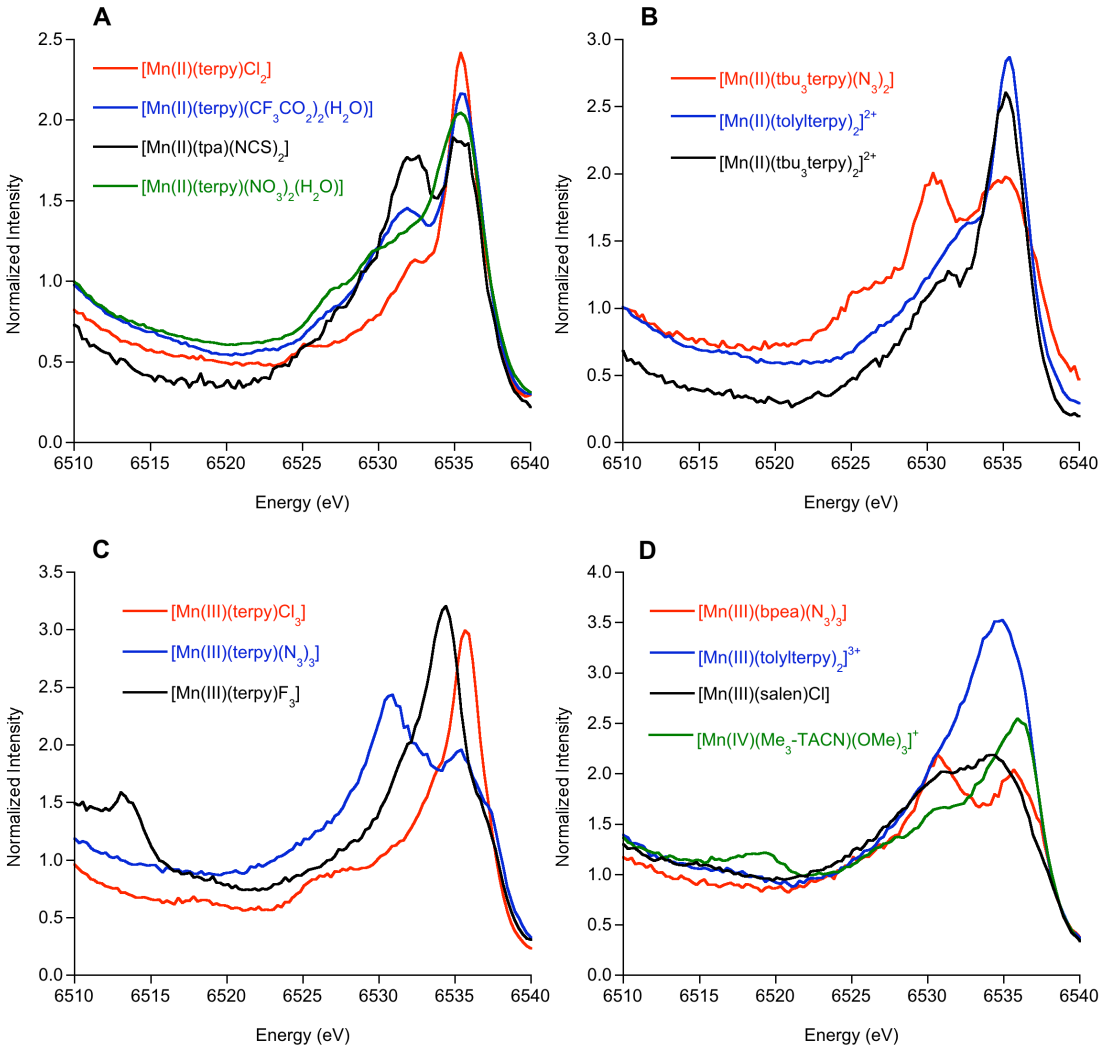

Figure 2.2. (A and B) Valence to core region for Mn(II) complexes. (C and D) Valence to core region for Mn(III) and Mn(IV) complexes.

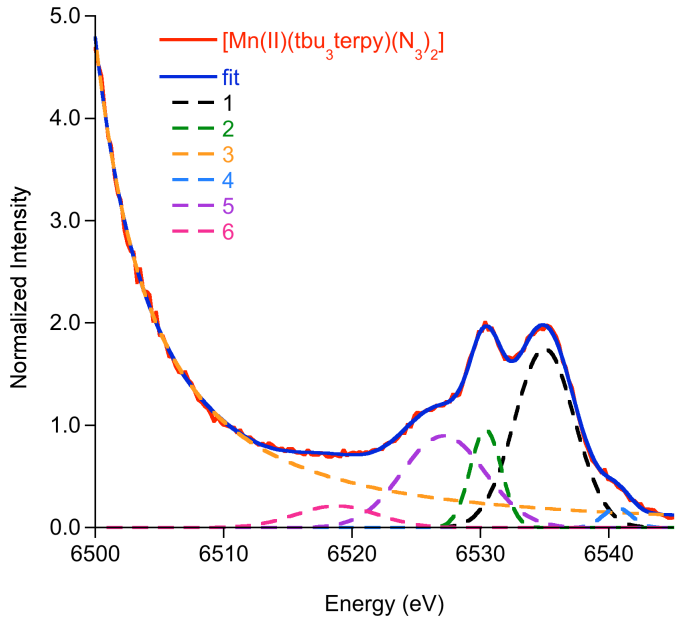

Figure 2.3. Representative fit to the valence to core region of [Mn(II)(tbu_3terpy)(N_3)$_2$].

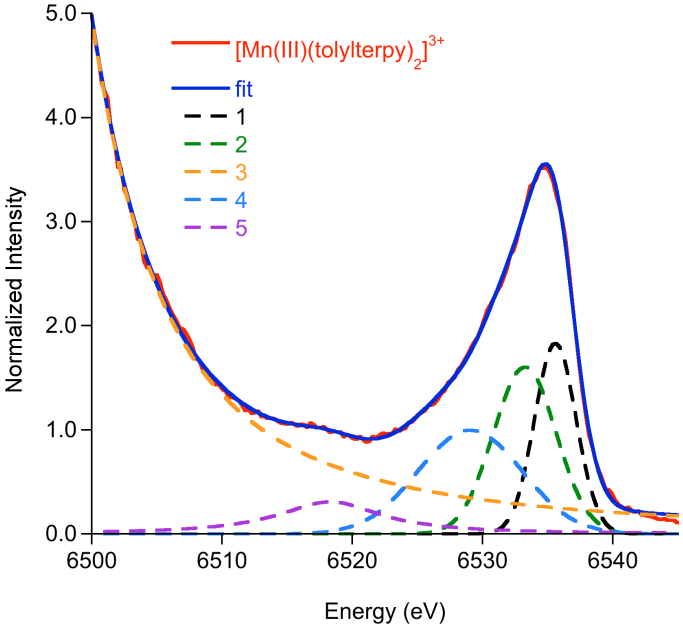

Figure 2.4. Representative fit to the valence to core region of [Mn(III)(tolylterpy)$_2$]$^{3+}$.

Valence to Core Spectral Features. In addition to the changes in the areas and energies, the valence to core region also shows pronounced changes in the number and distribution of spectral features. This is in contrast to the K$\beta_{1,3}$ main line spectra (Figure 2.1) which are very similar, and highlights the sensitivity of the valence to core spectra to the chemical environment. Note, that

due to the richly featured nature of the $K\beta_{2,5}$ region, it is difficult to pick a single peak maximum and therefore the intensity-weighted average energy of the $K\beta_{2,5}$ features (6525 – 6540 eV) is reported (Table 2.1). For the Mn(III) series, [Mn(III)(terpy)F_3], [Mn(III)(terpy)Cl_3], and [Mn(III)(terpy)$(N_3)_3$] shown in Figure 2.2C, the energies of both the more intense $K\beta_{2,5}$ features (~6525-6540 eV) and the satellites (~6510-6525 eV) reflect the differences in ionization energies of the bound ligands. It is also interesting to note that there are two intense features in the spectrum of [Mn(III)(terpy)$(N_3)_3$] (at 6530 and 6535 eV), possibly reflecting differences between the coordination of the nitrogen atoms from the terpy and azide ligands. Similar trends are observed for the spectra shown in Figure 2.2D, with the spectrum of [Mn(III)(bpea)$(N_3)_3$] showing a similar intense bimodal feature to higher energy.

There are also subtle differences in the spectra of the two Mn(II) complexes $[Mn(II)(tbu_3terpy)_2]^{2+}$ and $[Mn(II)(tolylterpy)_2]^{2+}$ (Figure 2.2B), despite the fact that in both complexes the atoms directly bound to the metal are all terpy nitrogens. This suggests that the overall nature of the ligand affects the observed spectral features. The spectra of [Mn(II)(tbu_3terpy)$(N_3)_2$] and [Mn(II)(tpa)$(NCS)_2$] both show the intense bimodal feature similar to [Mn(III)(terpy)$(N_3)_3$]. These spectra are in contrast to the homoleptic spectra for $[Mn(II)(tbu_3terpy)_2]^{2+}$ and $[Mn(II)(tolylterpy)_2]^{2+}$ and suggest that the valence to core spectra may allow for the separation of different ligand contributions within heteroleptic environments.

Calculation of Valence to Core XES Spectra.

In order to better understand the observed trends in the experimental data, DFT calculations were used to model the valence to core regions of the XES spectra. As noted above, the reported experimental energies (Table 2.1) correspond to the intensity-weighted average energy of the $K\beta_{2,5}$ features (6525 – 6540 eV) in the valence to core region. Analogous intensity-weighted average energies were obtained for the calculated data by first applying a constant energy shift

and then weighting the calculated intensity over the same region. Only the $K\beta_{2,5}$ feature was used to calculate the valence to core intensity-weighted average energies due to the strong background from the Kβ main line in the experimental spectra, which in many cases obscures the satellite features. Table 2.2 shows the calculated valence to core energies and the areas for the calculated spectra.

Analogous calculations were not used to predict the Kβ main lines because it was previously found that DFT underestimates the core-level spin polarization and therefore also strongly underestimates the 3p-3d exchange splitting.[55] In addition, the relative intensity ratios between the Kβ' and the $K\beta_{1,3}$ features cannot be accurately reproduced within a one-electron DFT picture due to the multi-configurational nature of these transitions. Thus, refined methods are needed in order to theoretically assess this region of the spectra. Progress has been made using multiplet calculations, though a considerable number of empirical parameters are required to simulate the spectra using such an approach and thus limits the predictive capability.[23, 56] In contrast, for the valence to core transitions there usually is a very good correlation between the calculated and experimental spectral shapes. However, in some cases peaks are present in the experimental spectra that cannot be modeled by the simple one-electron picture used in the calculations. These features will be discussed separately below.

The calculated energies are underestimated for all of the complexes studied here. Using the Mn(II), Mn(III) and Mn(IV) complexes as calibrations, an average energy shift of ~59.2 ± 0.7 eV was required to align theory with experiment. The necessity of applying a constant shift that is specific for each density functional and basis set combination but independent of the nature of the chemical species has been discussed at length before and is analogous for XAS and XES calculations.[29, 57, 58]

Table 2.2. $K\beta_{2,5}$ intensity-weighted average energies and valence to core areas for the calculated spectra of the Mn model complexes studied. The theoretical transition moments include the electric-dipole, electric quadrupole and magnetic dipole contributions.

Complex	$K\beta_{2,5}$ Intensity-weighted Average Energy (eV)[a]	Transition Moment	Predicted Experimental Area[b]
	Mn(II) Complexes		
$[Mn(acac)_2]$	6531.98	8.50×10^{-3}	12.89
$[Mn(tolylterpy)_2]^{2+}$	6532.34	8.44×10^{-3}	14.52
$[Mn(terpy)Cl_2]$	6533.12	7.93×10^{-3}	14.26
$[Mn(terpy)(NO_3)_2(H_2O)]$	6532.02	7.13×10^{-3}	12.20
$[Mn(tbu_3terpy)_2]^{2+}$	6532.29	8.49×10^{-3}	14.53
$[Mn(tbu_3terpy)(N_3)_2]$	6531.75	9.83×10^{-3}	16.84
$[Mn(terpy)(CF_3CO_2)_2(H_2O)]$	6531.85	7.42×10^{-3}	12.85
$[Mn(tpa)(NCS)_2]$	6531.71	8.56×10^{-3}	14.54
	Mn(III) Complexes		
$[Mn(acac)_3]$	6532.2	1.16×10^{-2}	22.51
$[Mn(tolylterpy)_2]^{3+}$	6533.24	1.31×10^{-2}	23.75
$[Mn(terpy)(N_3)_3]$	6532.21	1.27×10^{-2}	22.22
$[Mn(terpy)F_3]$	6533.15	1.15×10^{-2}	24.70
$[Mn(terpy)Cl_3]$	6534.01	1.00×10^{-2}	18.96
$[Mn(bpea)(N_3)_3]$	6532.3	1.21×10^{-2}	21.24
[Mn(salen)Cl]	6532.96	1.55×10^{-2}	30.06
	Mn(IV) Complexes		
$[Mn(Me_3\text{-}TACN)(OMe)_3]^+$	6533.07	1.55×10^{-2}	30.97

[a]Intensity-weighted average energies determined using the $K\beta_{2,5}$ peaks (6525 – 6540 eV eV). Satellite features in the < 6525 eV range are not included in the reported areas. A 59.2 eV energy shift has been applied to all calculated energies.

[b]Predicted experimental areas determined using the calculated areas and an area correlation fit line, $y = (5.73 \times 10^{-4})x + 6.79 \times 10^{-4}$.

Using only the Mn(II) complexes, the energy shift is ~59.7 ± 0.3 eV, while using only the Mn(III) complexes the energy shift is ~58.6 ± 0.4 eV. Hence, the calculated spectra show a shift to slightly higher energy upon oxidation of Mn(II) to Mn(III), which is in contrast to what was observed experimentally. It may be speculated that this results from the underestimated core level spin polarization that is intrinsic to pure DFT functionals, which incompletely cancels the contributions to the variations brought about by the changes in the effective nuclear charge of the manganese center (*vide supra*). However, the author refrains from introducing oxidation state specific shifts and hence tolerates a slightly larger error obtained by averaging the shift over all oxidation states.

The relationship between the calculated and experimental areas is shown in Figure 2.5. The calculated area is proportional to the calculated oscillator strength, which is composed of electric dipole, electric quadrupole, and magnetic dipole contributions. A closer inspection reveals that, as expected, the oscillator strength is dominated by electric dipole transitions (~96% on average). The relationship between the experimental and calculated areas for the valence to core region was found to be fairly linear, with a slope of $6.10 \times 10^{-4} \pm 8.97 \times 10^{-5}$ units of intensity/calculated fosc. The calculation faithfully reproduces the trend in experimental areas, with the Mn(II) complexes having smaller areas and the Mn(III) areas increasing.

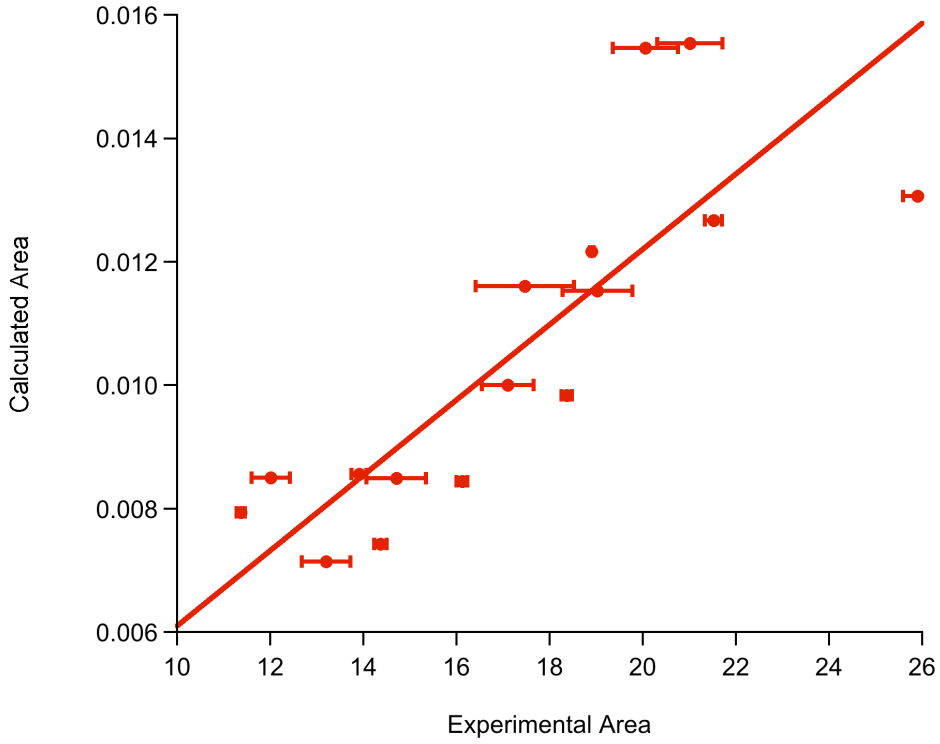

Figure 2.5. Calculated vs. experimental valence to core areas. The line has been forced through the origin and gives a slope of $6.10 \times 10^{-4} \pm 8.97 \times 10^{-5}$ units of intensity/calculated fosc. Error bars represent one standard deviation.

With a reasonably linear correlation established between the calculated and experimental energies and intensities, it is interesting to compare the experimental and theoretical spectra more closely. Figures 2.6 and 2.7 show the comparisons between the experimental valence to core

spectra in Figure 2.2 to their respective calculated spectra. A constant shift of 59.2 eV and a broadening of 2.5 eV have been applied to all of the calculated spectra. These comparisons demonstrate that the calculations reasonably predict the spectral shapes in terms of relative splittings and intensity distributions of observed valence to core features.

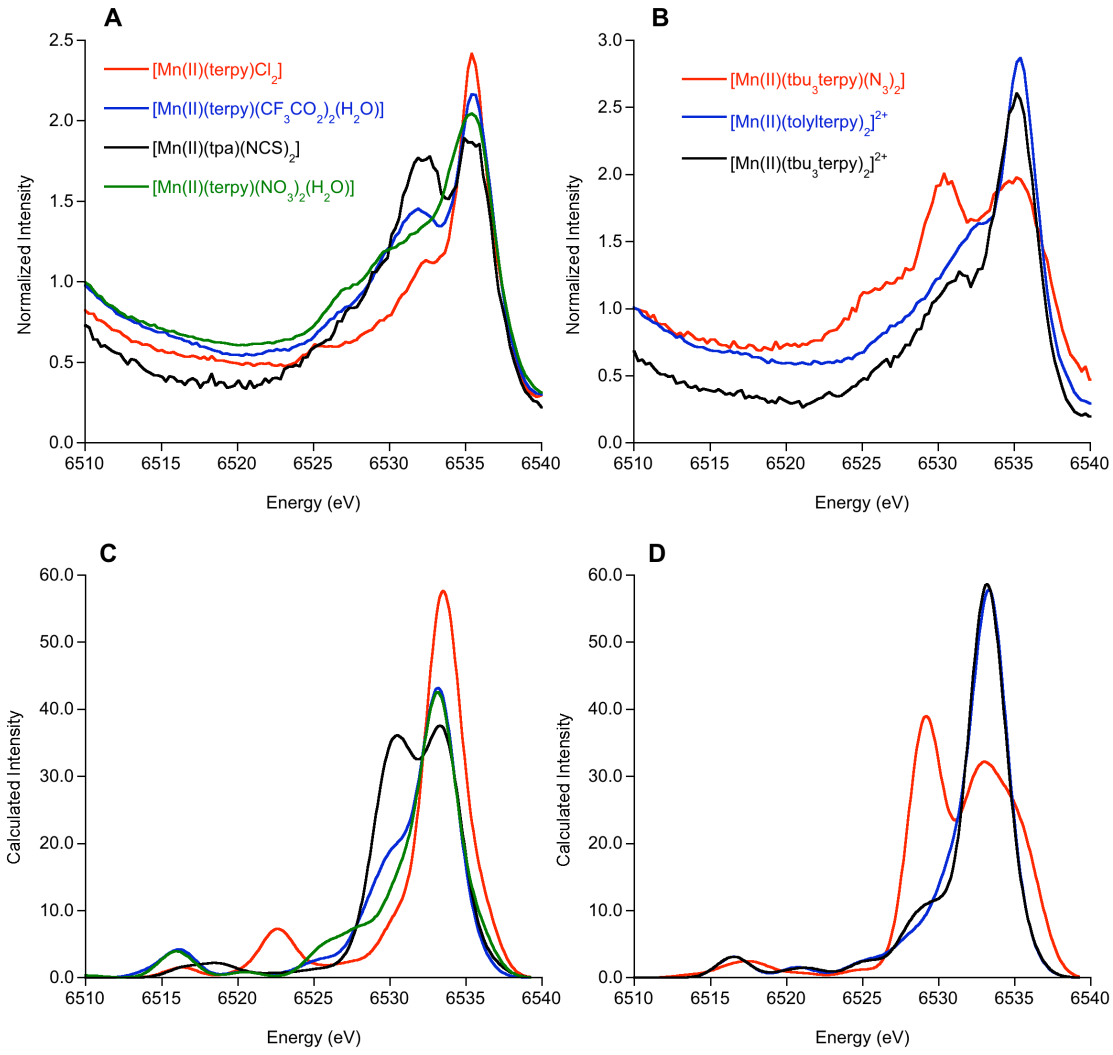

Figure 2.6. (A and B) Experimental valence to core region for Mn(II) complexes. (C and D) The corresponding calculated spectra. A constant shift of 59.2 eV and a 2.5 eV broadening have been applied to all calculated spectra.

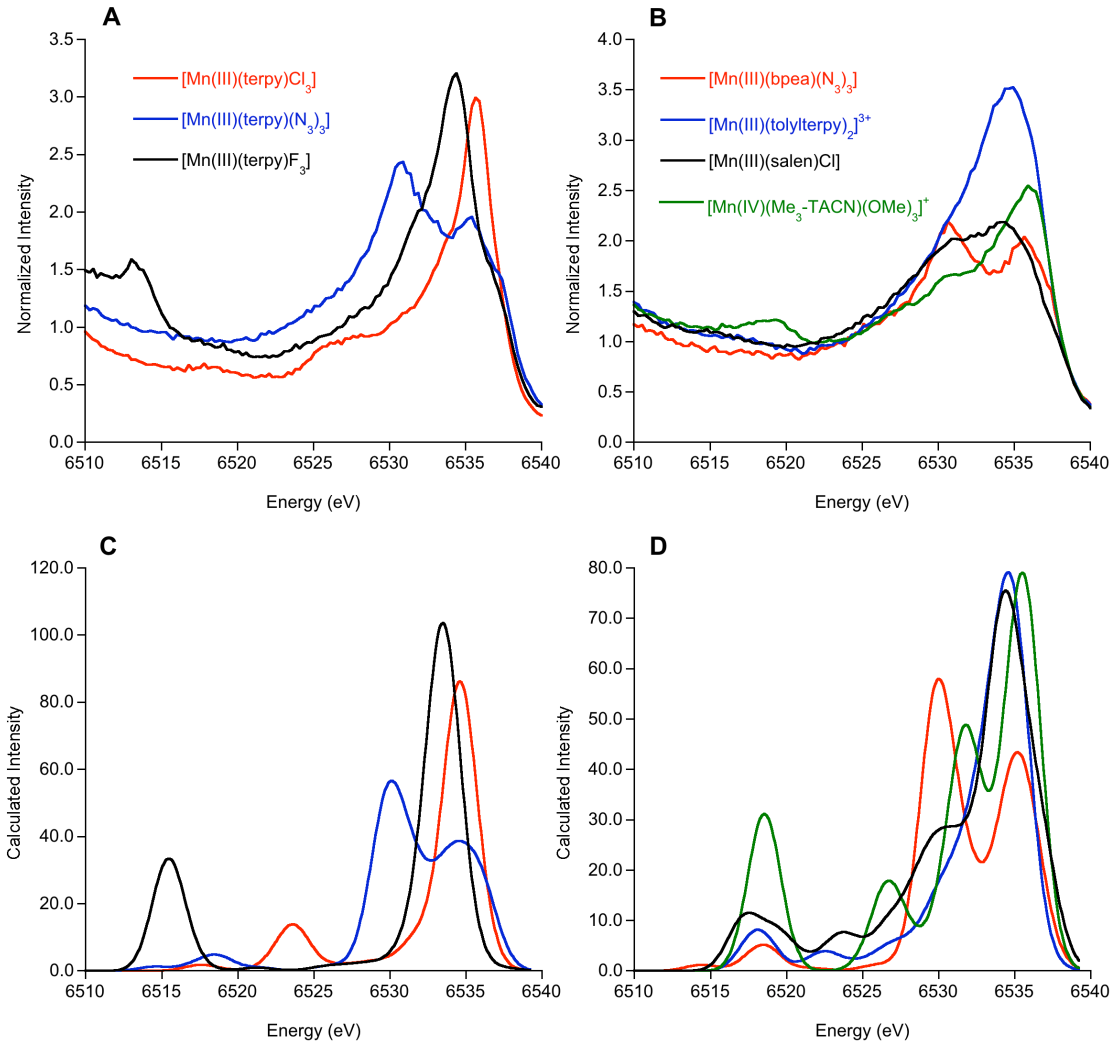

Figure 2.7. (A and B) Experimental valence to core region for Mn(III) and Mn(IV) complexes. (C and D) The corresponding calculated spectra. A constant shift of 59.2 eV and a 2.5 eV broadening have been applied to all calculated spectra.

In some cases features calculated in the 6510 – 6525 eV satellite region are very weak or even absent in the experimental spectra, whereas in other cases satellite features with similar calculated intensities are clearly observed. This is most easily seen when comparing the experimental and calculated spectra of [Mn(III)(terpy)Cl_3] and [Mn(III)(terpy)$(N_3)_3$] in Figures 2.7A and C, respectively. For [Mn(III)(terpy)Cl_3] even the very weak feature at ~6518 eV (with ~4 units of calculated intensity) is observed experimentally, while for [Mn(III)(terpy)$(N_3)_3$] the

calculated feature at 6518 (with ~8 units of intensity) is not observed. This may in part be attributed to variations in the strong background from the Kβ main line, which may obscure weaker features in the experimental spectra. These observations provide insight into an intensity threshold that is needed in the calculated spectra in order for satellite features to be clearly seen above the background in the experiment. Assuming similar background contributions from the Kβ main line, as with the spectra in Figure 2.7B, it is conservatively estimated that at least ~15–20 calculated intensity units are needed in order for a calculated satellite feature to be observed experimentally. This estimate will change, of course, with varying degrees of background intensity, but represents a helpful rule of thumb when one is aiming at using the calculated spectra in a predictive fashion.

Nature of the Valence to Core Features.

[Mn(III)(terpy)Cl_3]. As mentioned previously, the valence to core spectra are dominated by dipole allowed Mn *n*p to Mn 1s transitions. Within the chosen approach, the calculated XES spectra exclusively reflect the single particle spectrum of the system under investigation. Thus, all features can be interpreted in terms of molecular orbitals rather than many electron states. This greatly simplifies the discussion although the author is aware that experimentally only the many particle wavefunctions and states are being probed.

Figure 2.8 shows the calculated spectrum of [Mn(III)(terpy)Cl_3] as well as representative MOs that predominately contribute to each feature. The most intense peak at ~6535 eV (Figure 2.8, feature C) arises from MOs that are primarily composed of Cl-p character, with smaller contributions from C-p and N-p oribtals. A very weak shoulder at ~6539 eV (Figure 2.8, feature D) corresponds to transitions from the manganese 3d-based t_{2g} set of orbitals, which gains intensity due to ~0.2% Mn p mixing. The lower energy satellite feature at ~6525 eV (Figure 2.8,

feature B) corresponds to transitions from MOs that are dominantly Cl-3s character, while the less intense satellite feature at ~6518 eV (Figure 2.8, feature A) corresponds to transitions from orbitals that are primarily composed of N-s and C-s character. The most intense features arise from 5-7% Mn-*n*p character mixed into each of the MOs. It should be noted that the satellite feature at ~6525 eV is approximately half as intense as the analogous satellite feature in [Mn(III)(terpy)F_3]. This is likely due to the differences in the average Mn-Cl and Mn-F bond lengths (2.28 and 1.83 Å, respectively). As discussed previously in the case of iron complexes,[29] the shorter bond length in [Mn(III)(terpy)F_3] increases the amount of Mn-p character that is mixed into the MOs associated with the satellite feature, and this increase in Mn-p mixing raises the intensity of the observed feature.

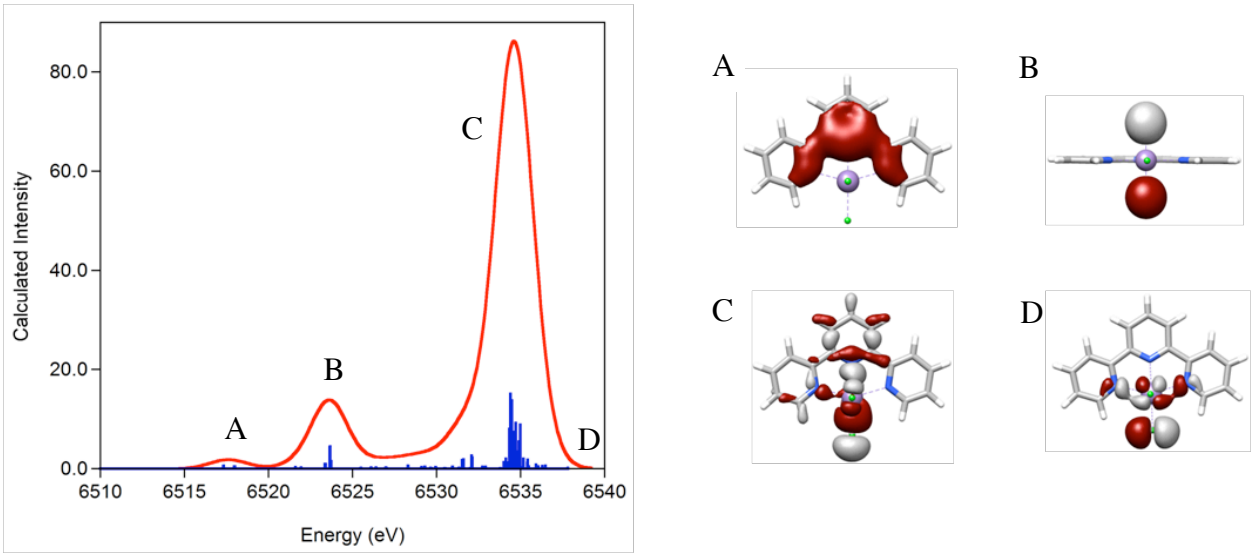

Figure 2.8. Calculated valence to core spectrum of [Mn(III)(terpy)Cl_3] (left) and predominant molecular orbitals that contribute to the observed transitions (right).

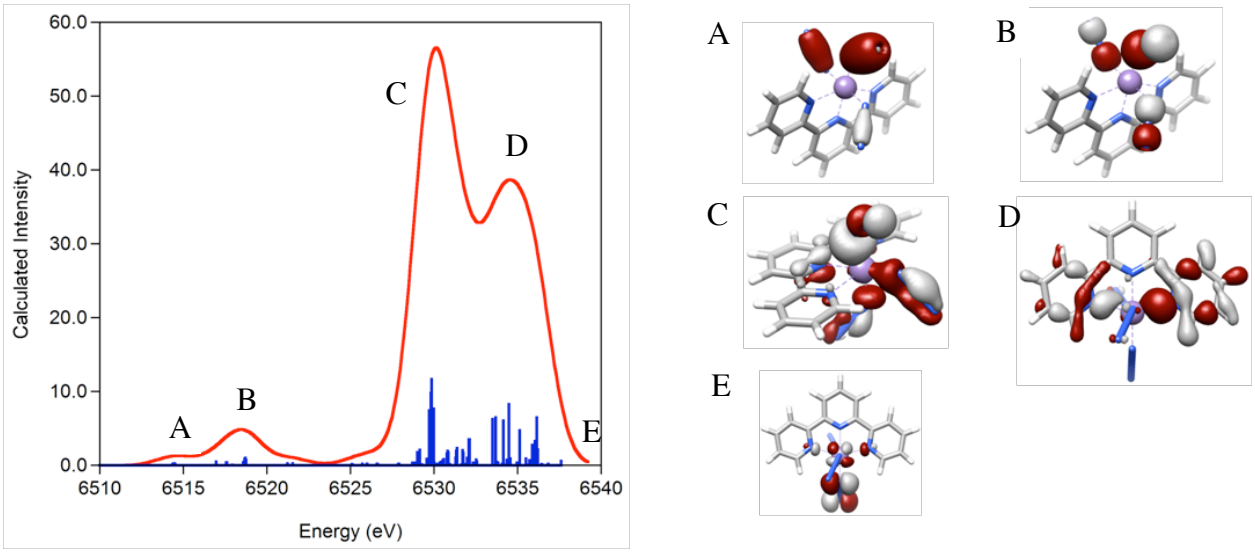

Figure 2.9. Calculated valence to core spectrum of [Mn(III)(terpy)$(N_3)_3$] (left) and predominant molecular orbitals that contribute to the observed transitions (right).

[Mn(III)(terpy)$(N_3)_3$]. Figure 2.9 shows the calculated spectrum of [Mn(III)(terpy)$(N_3)_3$] together with representative MOs that dominantly contribute to the observed features. Analogous to [Mn(III)(terpy)Cl_3], the valence to core spectrum is composed of transitions from predominantly ligand p-orbitals, with 1-7% Mn-p character thus providing a viable intensity mechanism. The most intense feature at a lower energy of ~6530 eV (Figure 2.9, feature C) arises from transitions that are predominantly azide N-p and N-s based (48.1% N-p, 19.5% N-s). The orbitals from which these particular transitions originate are primarily metal azide sigma-bonding orbitals with two nodal planes. The lower intensity cluster of transitions between ~6530 – 6531 eV also corresponds to sigma-bonding orbitals, however the orbitals in this region contain four nodal planes as opposed to two, and thus the emission transitions occur at slightly higher energies. Regardless of the number of nodal planes, these transitions from metal azide p-sigma bonding orbitals occur at lower energies than the analogous chlorine p-orbitals that form sigma bonds with the metal in [Mn(III)(terpy)Cl_3]. This shift to lower energy is a reflection of the difference in the Cl-3p and N-2p ionization energies.

The intense higher energy feature at ~6535 eV (Figure 2.9, feature D) corresponds to

transitions from orbitals that are a mixture of azide N-p and terpy N-p and C-p, with the most intense transition resulting from dominantly terpy N-p and C-p sigma bonding molecular orbitals. The transitions between ~6535 – 6536 eV result from azide π-orbitals interacting with the metal. A lower energy satellite feature at ~6520 eV (Figure 2.9, feature B) corresponds to transitions from azide N-s and N-p orbitals, with one nodal plane within the azide. This feature is shifted by ~5 eV relative to the most intense satellite feature in [Mn(III)(terpy)Cl_3] and reflects the difference in the Cl-3s and N-2s ionization energies. A lower intensity satellite feature at ~6515 eV (Figure 2.9, feature A) corresponds to transitions from azide N-s orbitals with no nodal planes within the azide. The feature at ~6518 eV in [Mn(III)(terpy)Cl_3] that corresponds to transitions from terpy N-s and C-s orbitals is also present in [Mn(III)(terpy)$(N_3)_3$], but it cannot be resolved at ~2.5 eV broadening. As in [Mn(III)(terpy)Cl_3], a cluster of transitions from the t_{2g} set of orbitals occurs at ~6538 eV (Figure 2.9, feature E). None of the intense transitions are associated with MOs that contain a significant amount of d-character. This observation once more supports the dominantly dipole allowed nature of these transitions.

As the valence to core XES spectra reflect ligand orbitals that are filled in the electronic ground state, the question arises as to whether or not the spectra could help to determine a 10Dq parameter (i.e. via the energy splitting between the dominantly ligand σ-bonding and π-bonding MOs). However, the results show that the intensity is dominantly associated with the transitions involving MOs that are σ-bonding between the metal and the ligands. Hence, the transitions involving π-bonding orbitals are difficult to identify. In addition, the little intensity that can be attributed to those transitions is often not completely separable from the σ-based intensity.[59]

Hypothetical Molecule Calculations.

As noted above, the areas of the experimental valence to core spectra increase significantly (by a factor of ~1.6) upon oxidation of Mn(II) to Mn(III). In contrast, upon going from a high-spin

Fe(II) complex to a high-spin Fe(III) complex only a modest (~1.1) increase in intensity is observed.[29] These effects are reproduced by the calculations and may offer insight into the physical origin of this differing behavior between the two metals. To this end, a series of calculations was performed on hypothetical molecules involving Mn and Fe in various oxidation states. Figures 2.10A and B show the calculated spectra for high-spin $[M(II)Cl_6]^{4-}$, $[M(III)Cl_6]^{3-}$ and $[M(IV)Cl_6]^{2-}$ (M=Mn, Fe). The bond lengths are provided in Table 2.3.

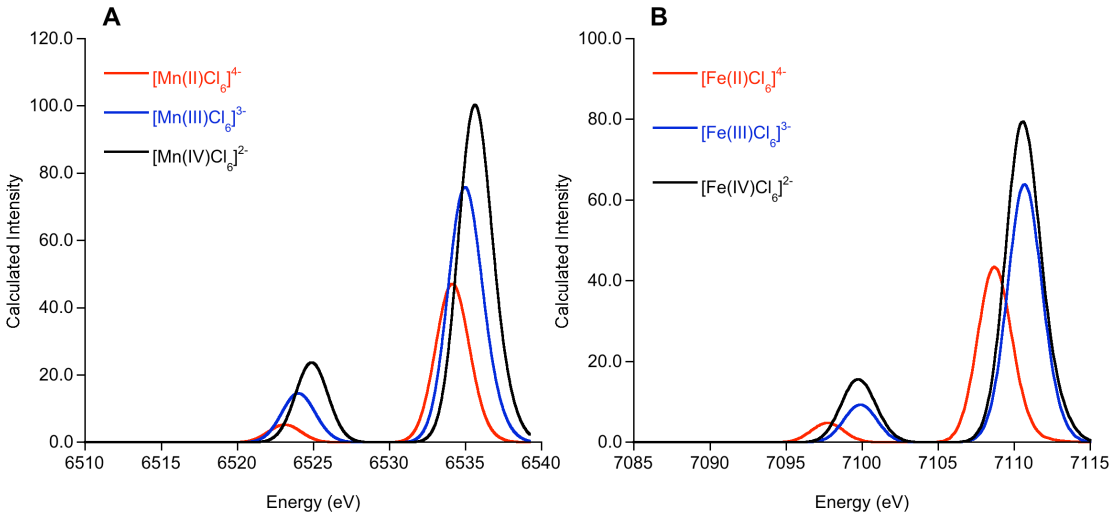

Figure 2.10. (A) Calculated valence to core spectra for high-spin $[Mn(II)Cl_6]^{4-}$, $[Mn(III)Cl_6]^{3-}$ and $[Mn(IV)Cl_6]^{2-}$. (B) Calculated valence to core spectra for high-spin $[Fe(II)Cl_6]^{4-}$, $[Fe(III)Cl_6]^{3-}$ and $[Fe(IV)Cl_6]^{2-}$. All calculated spectra have been energy shifted to match appropriate experimental values.

Table 2.3. M-Cl bond lengths (Å) for the optimized structures of the calculated high-spin $[M(II)Cl_6]^{4-}$, $[M(III)Cl_6]^{3-}$ and $[M(IV)Cl_6]^{2-}$ (M=Mn, Fe) complexes.

Bond (Å)	$[Mn(II)Cl_6]^{4-}$	$[Mn(III)Cl_6]^{3-}$	$[Mn(IV)Cl_6]^{2-}$	$[Fe(II)Cl_6]^{4-}$	$[Fe(III)Cl_6]^{3-}$	$[Fe(IV)Cl_6]^{2-}$
M-Cl(1)	2.64	2.72	2.31	2.56	2.45	2.51
M-Cl(2)	2.64	2.33	2.31	2.56	2.45	2.27
M-Cl(3)	2.64	2.33	2.31	2.64	2.45	2.28
M-Cl(4)	2.64	2.33	2.31	2.64	2.45	2.28
M-Cl(5)	2.64	2.33	2.31	2.56	2.45	2.27
M-Cl(6)	2.64	2.72	2.31	2.56	2.45	2.51

For the $[MnCl_6]^n$ series, there is a shift of all discernable spectral features to higher energy upon oxidation of Mn(II) to Mn(III) (by ~0.8 eV), and also upon subsequent oxidation of Mn(III) to Mn(IV). For the $[FeCl_6]^n$ series there is also a shift to higher energy when going from Fe(II)

to Fe(III) (by ~ 2eV), but there is essentially no change when Fe(III) is oxidized to Fe(IV). These support the experimental observations and suggest that there are competing Z_{eff} and spin state effects that contribute to the calculated valence to core energies.

Figure 2.11 shows the relationship between the calculated areas and the calculated bond distances for both series. The relationship is manifestly linear (blue fit line = Mn, red fit line = Fe). Previous studies on iron required an exponential fit for a similar series,[29] however, for the shorter range of distances presented here, both linear and exponential fits are equally good.

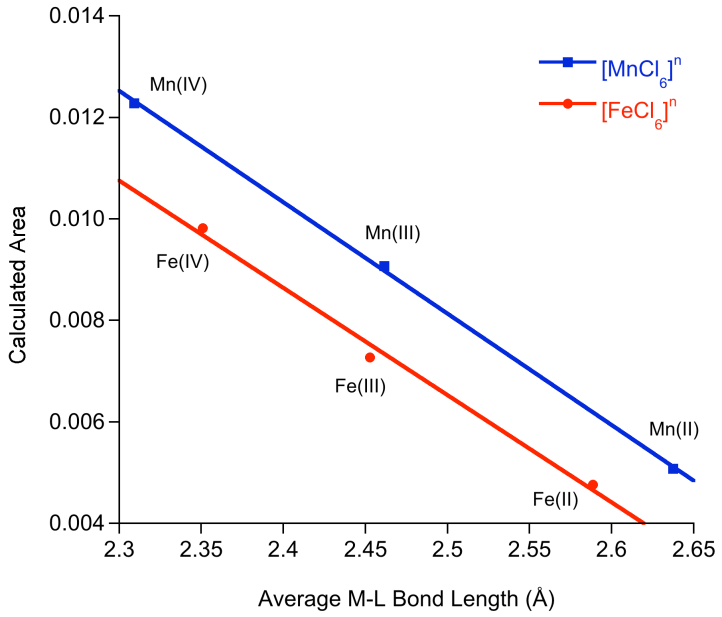

Figure 2.11. Calculated area vs. average bond length for the $[MnCl_6]^n$ series (blue squares) and for the $[FeCl_6]^n$ series (red circles). The fit for the $[MnCl_6]^n$ series gives a slope of -0.022 and the fit for the $[FeCl_6]^n$ series gives a slope of -0.021.

The calculated areas of the $[MnCl_6]^n$ complexes are on average ~1.2 times larger than the corresponding $[FeCl_6]^n$ complexes of the same metal oxidation state. For both series, the average bond length decreases as oxidation state increases, as expected; however the calculated intensity is always higher at Mn even given the same metal-ligand bond length. It should be noted that even if the differences in atomic radii are taken into account,[60] the calculated intensities for Mn are still higher than for Fe (see Figure 2.12) though the magnitude of the effect decreases to a

factor of ~1.1.

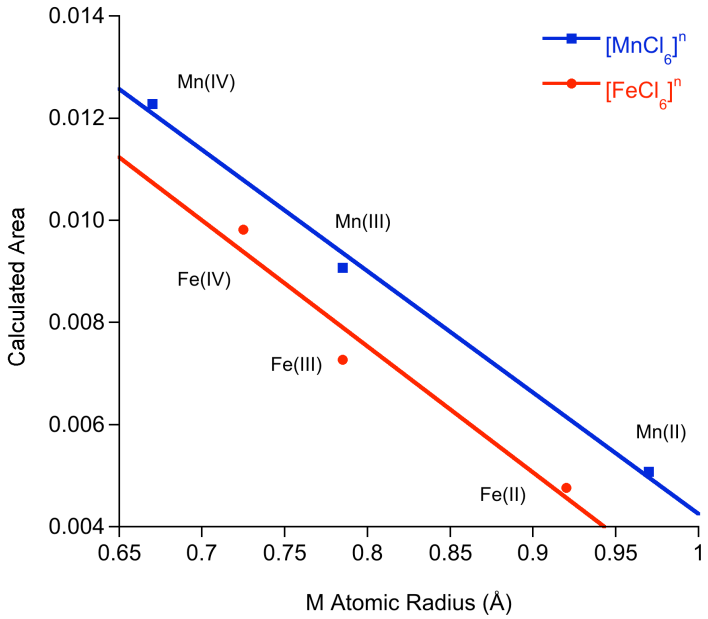

Figure 2.12. Calculated XES valence to core area vs. metal atomic radius for the $[MnCl_6]^n$ series (blue squares) and for the $[FeCl_6]^n$ series (red circles). The fit for the $[MnCl_6]^n$ series gives a slope of -0.024 and the fit for the $[FeCl_6]^n$ series gives a slope of -0.025.

In order to investigate this effect systematically and eliminate all secondary factors that could contribute to the observations, calculations on the hypothetical molecule $[M(H_2O)_5Cl]^{n+}$, $S = 5/2$ where for M = Fe n = 2+ and for M = Mn n = 1+. A common idealized geometry was used in which the M-Cl bond is 2.25 Å, the M-OH_2 is 2.15 Å long and all angles are perfectly octahedral.

In order to understand the intensity differences in more detail, the composition of the donor orbitals and the intensity contributions for two of the more intense transitions in the two test molecules were analyzed. The relevant part of the transition dipole moment between a metal core-1s orbital $\psi_C = \varphi_{M_{1s}}$ and a valence orbital $\psi_V = \sum_{\mu_A} c_{\mu V} \varphi_\mu^A$ is the one that contains metal p-character. Thus, one can decompose the transition moment into a local part that involves the metal p-character and a non-local part that involves other valence orbital contributions. For convenience a transition polarized along the z-axis is considered and the origin of the coordinate

system was chosen to coincide with the metal center.

$$\left\langle \psi_V \mid z_M \mid \psi_C \right\rangle = \underbrace{c^M_{M_p} \left\langle \varphi^M_p \mid z_M \mid \varphi^B_{M_{1s}} \right\rangle}_{local} + \underbrace{\sum_{\mu_A (A \neq M)} c_{\mu V} \left\langle \varphi^A_\mu \mid z_M \mid \varphi_{M_{1s}} \right\rangle}_{non-local} \tag{2.1}$$

Here z_M is the z-coordinate position operator measured relative to the metal center. The local part contains two contributions: the metal p-character mixed into the valence MO (measured by $(c^M_{M_p})^2$) and the local transition dipole moment $\left\langle \varphi^M_p \mid z_M \mid \varphi^B_{M_{1s}} \right\rangle$. From atomic calculations it was found that the local transition dipole moments for manganese and iron are very similar (e.g. 0.00776 a.u. for Mn^{2+}, 0.00755 a.u. for Fe^{2+} and 0.00765 a.u. for Fe^{3+}). These differences on the order of 1-2% cannot explain the differences in the observed valence to core intensities, which are an order of magnitude larger. However, because chemical bonding within a molecule distorts the atomic radial functions, the atomic transition dipole moment values will also be modified in a molecular environment. In order to understand the dominating factors in more detail, the two most intense transitions in the 3s and the 3p region of the of the XES spectra for $[M(H_2O)_5Cl]^{n+}$ are analyzed in Table 2.4.

Table 2.4. Analysis of the intensity mechanism for two XES transitions in the 3s (top) and 3p (bottom) region of the XES spectra of $[Mn(II)(H_2O)_5Cl]^{1+}$ and $[Fe(III)(H_2O)_5Cl]^{2+}$. Listed are the percentage metal character (%M), Cl character (%Cl) and remaining ligands (%L) in the XES donor orbitals, the gross metal p character ($\%M_p$), the overlap charge between the metal and all ligands (OVL), the total transition dipole moment squared (D^2, in $a.u.^2$), the local and non-local contributions to the transition dipole moment and the local radial expectation value of the position operator renormalized to unit metal p-character.

	Cl 3s-Donor MO								
	%M	**%Cl**	**%L**	**$\%M_p$**	**OVL**	**D^2**	**loc**	**Non-loc**	**$\langle z_M \rangle_{1s,p}$ ($x10^6$)**
Fe	18.1	81.1	0.9	0.18	0.05	316.5	311.7	4.1	7332.3
Mn	19.2	79.6	1.2	0.31	0.09	383.6	376.4	7.2	6702.5

	Cl 3p-Donor MO								
	%M	**%Cl**	**%L**	**$\%M_p$**	**OVL**	**D^2**	**loc**	**Non-loc**	**$\langle z_M \rangle_{1s,p}$ ($x10^6$)**
Fe	23.6	72.7	3.8	1.08	0.11	672.8	660.7	12.1	6333.6
Mn	15.6	82.2	2.3	0.94	0.11	731.7	7161.1	15.6	7346.1

The data in Table 2.4 demonstrates that the local contributions indeed dominate the transition dipole moment. The nonlocal terms account for about 1-3% of the total transition dipole, however their values are not drastically different for the two metals so they will not be addressed further. In the Cl 3s region of the XES spectra, the manganese contribution to the transition dipole moment stems from the larger amount of metal p-character mixed into the valence MO. The local transition dipole moment for manganese is actually considerably smaller than its atomic value, but the almost factor of two higher metal p-character than in the atomic case compensates for this in terms of an overall contribution from the manganese to the transition dipole moment. In the Cl 3p-region of the XES spectrum the situation is reversed: the metal p-character is similar for both metals but the local manganese transition dipole moment is over 10 times higher than in the iron case.

In both cases, the net result is that the intensity in the manganese spectrum is higher, which is in agreement with the experimental observations. The reasons, however, are fairly subtle and are related to both the distortion of the metal p-orbitals in the molecular environment, and the

amount of metal p-character mixed into the valence orbitals. It is evident from previous work that both the metal 3p and 4p character contribute to the intensity in the satellite region of the XES spectra. Obviously, the amount of mixing between the 3p and the 4p set of metal orbitals with the ligand orbitals depends on their energetic position relative to the ligand orbitals. This position in turn depends on the effective nuclear charge of the metal ion and varies with oxidation and spin state. However, the position also depends on the nature of the valence orbitals themselves. In the 3p set, the p-character in the valence orbitals is of an antibonding nature, which will tend to expand the radial wavefunction and increase the radial expectation value. For the 4p set, the mixed-in p-character will be of a bonding nature, which will tend to contract the radial wavefunction and decrease the radial expectation value. Both types of behavior are found in Table 2.4, illustrating the complexity of the problem. In addition, the metal p-character is very small and only amounts to a fraction of a percent (i.e. *two* orders of magnitude less than the total metal character in these orbitals). However, the calculations appear to reproduce the trends in the experimental data reasonably well which implies that, despite the fact that the effect is very small, the leading physically relevant contributions to the intensity are captured correctly.

Conclusions

A systematic experimental and computational study of Mn Kβ XES spectra for a series of high-spin mononuclear manganese complexes has been presented. The study has focused on the valence to core region of the XES spectra. This region shows a pronounced sensitivity to the chemical environment and reacts to differences in oxidation state, spin state, and ligand identity.

The generally good agreement between experimental and calculated spectra has allowed for a more detailed investigation of the orbital contributions to the experimental valence to core

spectra. As expected, the spectra are dominated by dipole allowed Mn *n*p to 1s transitions. The energy shifts observed in this region are a result of both the effective nuclear charge at the manganese and spin state effects. They have been shown to have opposing effects on the resulting spectra for the most common oxidation states of manganese (+2 to +4), thus resulting in smaller overall energetic differences than have previously been observed for Fe valence to core XES spectra.[29]

Based on the results reported here, the valence to core area appears to be a reliable indicator of Mn oxidation state: as the oxidation state increases, the area also increases significantly. This is in contrast to what has been observed for Fe, where the valence to core area did not change significantly upon oxidation of Fe complexes of the same spin state.[29] These differences between the trends for Mn and Fe areas are, in part, a result of the more pronounced bond length changes for Mn. They arise due to more significant Jahn-Teller effects in Mn complexes compared to Fe complexes – in Mn complexes the Jahn-Teller active configuration occurs at Mn(III) while in Fe it is Fe(II) which has much weaker metal-ligand bond distances. The differences between Mn and Fe are also partially due to differences in the distortions of the metal p-orbitals in a molecular environment, as well as differences in the amount of p-character mixed into the valence orbitals.

In addition to spin- and oxidation state, the Mn valence to core region is also sensitive to ligand identity, showing ligand *n*p and *n*s contributions, similar to what was seen previously in Fe complexes. Specifically for Mn, the valence to core spectra may allow for the separation of different ligand contributions within heteroleptic environments, as seen in the dramatic differences between the spectra of $[Mn(III)(tolylterpy)_2]^{3+}$, and $[Mn(III)(terpy)(N_3)_3]$, for example. This sensitivity to ligand environment, along with the strong correlation between experiment and theory, suggests that the valence to core region of the XES spectra may be a

useful predictive tool for examining Mn active sites in biological systems. The calibration study presented here forms the basis for future quantitative studies of the XES spectra in complex ligand environments, including the Mn_4Ca cluster in the active site of photosystem II.[11, 61, 62]

References

1. Abreu, I. A.; Cabelli, D. E., *BBA-Proteins Proteomics* **2010,** *1804*, 263.
2. Abreu, I. A.; Rodriguez, J. A.; Cabelli, D. E., *J. Phys. Chem. B* **2005,** *109*, 24502.
3. Fridovich, I., *Annu. Rev. Biochem.* **1995,** *64*, 97.
4. Pecoraro, V. L.; Hsieh, W.-Y., In *Manganese and Its Role in Biological Processes*, Sigel, A.; Sigel, H., Eds. Marcel Dekker Inc: New York, 2000; Vol. 37, pp 429.
5. Vrettos, J. S.; Brudvig, G. W., *Philos. Trans. R. Soc. London, Ser. B* **2002,** *357*, 1395.
6. Fu, B.; Yu, H. C.; Huang, J. W.; Zhao, P.; Liu, J.; Ji, L. N., *J. Mol. Catal. A-Chem.* **2009,** *298*, 74.
7. Gupta, K. C.; Sutar, A. K.; Lin, C. C., *Coord. Chem. Rev.* **2009,** *253*, 1926.
8. McLain, J. L.; Lee, J.; Groves, J. T., In *Biomimetic Oxidation Catalyzed by Transition Metal Complexes*, Meunier, B., Ed. Imperial College Press: London, 2000; pp 91.
9. Palucki, M.; Finney, N. S.; Pospisil, P. J.; Güler, M. L.; Ishida, T.; Jacobsen, E. N., *J. Am. Chem. Soc.* **1999,** *120*, 948.
10. Tabares, L. C.; Gatjens, J.; Un, S., *BBA-Proteins Proteomics* **2010,** *1804*, 308.
11. Messinger, J.; Robblee, J. H.; Bergmann, U.; Fernandez, C.; Glatzel, P.; Visser, H.; Cinco, R. M.; McFarlane, K. L.; Bellacchio, E.; Pizarro, S. A.; Cramer, S. P.; Sauer, K.; Klein, M. P.; Yachandra, V. K., *J. Am. Chem. Soc.* **2001,** *123*, 7804.
12. Su, J. H.; Lubitz, W.; Messinger, J., *J. Am. Chem. Soc.* **2008,** *130*, 786.
13. Su, J. H.; Messinger, J., *Appl. Magn. Reson.* **2010,** *37*, 123.
14. de Groot, F. M. F., *Chem. Rev.* **2001,** *101*, 1779.
15. Mukoyama, T., *Spectrochim. Acta B* **2004,** *59*, 1107.
16. Penner-Hahn, J. E., *Coord. Chem. Rev.* **2005,** *249*, 161.
17. Qian, Q.; Tyson, T. A.; Kao, C. C.; Croft, M.; Cheong, S. W.; Popov, G.; Greenblatt, M., *Phys. Rev. B* **2001,** *64*.
18. Strange, R. W.; Ellis, M.; Hasnain, S. S., *Coord. Chem. Rev.* **2005,** *249*, 197.
19. Yano, J.; Kern, J.; Irrgang, K. D.; Latimer, M. J.; Bergmann, U.; Glatzel, P.; Pushkar, Y.; Biesiadka, J.; Loll, B.; Sauer, K.; Messinger, J.; Zouni, A.; Yachandra, V. K., *Proc. Natl. Acad. Sci. U. S. A.* **2005,** *102*, 12047.
20. Yano, J.; Kern, J.; Sauer, K.; Latimer, M. J.; Pushkar, Y.; Biesiadka, J.; Loll, B.; Saenger, W.; Messinger, J.; Zouni, A.; Yachandra, V. K., *Science* **2006,** *314*, 821.
21. Yano, J.; Yachandra, V. K., *Inorg. Chem.* **2008,** *47*, 1711.
22. Bergmann, U.; Glatzel, P.; Robblee, J. H.; Messinger, J.; Fernandez, C.; Cinco, R.; Visser, H.; McFarlane, K.; Bellacchio, E.; Pizarro, S.; Sauer, K.; Yachandra, V. K.; Klein, M. P.; Cox, B. L.; Nealson, K. H.; Cramer, S. P., *J. Synchrot. Radiat.* **2001,** *8*, 199.
23. Glatzel, P.; Bergmann, U., *Coord. Chem. Rev.* **2005,** *249*, 65.
24. Glatzel, P.; Bergmann, U.; deGroot, F. M. F.; Cramer, S. P., *Phys. Rev. B* **2001,** *64*.
25. Peng, G.; deGroot, F. M. F.; Hamalainen, K.; Moore, J. A.; Wang, X.; Grush, M. M.; Hastings, J. B.; Siddons, D. P.; Armstrong, W. H.; Mullins, O. C.; Cramer, S. P., *J. Am. Chem. Soc.* **1994,** *116*, 2914.
26. Visser, H.; Anxolabéhère-Mallart, E.; Bergmann, U.; Glatzel, P.; Robblee, J. H.; Cramer, S. P.; Girerd, J.-J.; Sauer, K.; Klein, M. P.; Yachandra, V. K., *J. Am. Chem. Soc.* **2001,** *123*, 7031.
27. Bergmann, U.; Bendix, J.; Glatzel, P.; Gray, H. B.; Cramer, S. P., *J. Chem. Phys.* **2002,** *116*, 2011.
28. Bergmann, U.; Horne, C. R.; Collins, T. J.; Workman, J. M.; Cramer, S. P., *Chem. Phys. Lett.* **1999,** *302*, 119.

29. Lee, N.; Petrenko, T.; Bergmann, U.; Neese, F.; DeBeer, S., *J. Am. Chem. Soc.* **2010,** *132*, 9715.
30. Smolentsev, G.; Soldatov, A. V.; Messinger, J.; Merz, K.; Weyhermüller, T.; Bergmann, U.; Pushkar, Y.; Yano, J.; Yachandra, V. K.; Glatzel, P., *J. Am. Chem. Soc.* **2009,** *131*, 13161.
31. Pushkar, Y.; Long, X.; Glatzel, P.; Brudvig, G. W.; Dismukes, G. C.; Collins, T. J.; Yachandra, V. K.; Yano, J.; Bergmann, U., *Angew. Chem. Int. Ed.* **2010,** *49*, 800.
32. Baffert, C.; Romero, I.; Pécaut, J.; A.Llobet; Deronzier, A.; Collomb, M.-N., *Inorg. Chim. Acta* **2004,** *357*, 3430.
33. Duboc, C.; Collomb, M. N., *Chem. Comm.* **2009**, 2715.
34. Duboc, C.; Collomb, M. N.; Pécaut, J.; Deronzier, A.; Neese, F., *Chem.-Eur. J.* **2008,** *14*, 6498.
35. Limburg, J.; Vrettos, J. S.; Crabtree, R. H.; Brudvig, G. W.; Paula, J. C. d.; Hassan, A.; A.-L.Barra; Duboc-Toia, C.; Collomb, M.-N., *Inorg. Chem.* **2001,** *40*, 1698.
36. Mantel, C.; Baffert, C.; Romero, I.; Deronzier, A.; Pécaut, J.; Collomb, M. N.; Duboc, C., *Inorg. Chem.* **2004,** *43*, 6455.
37. Mantel, C.; Chen, H. Y.; Crabtree, R. H.; Brudvig, G. W.; Pécaut, J.; Collomb, M. N.; Duboc, C., *ChemPhysChem* **2005,** *6*, 541.
38. Mantel, C.; Hassan, A. K.; Pécaut, J.; Deronzier, A.; Collomb, M. N.; Duboc-Toia, C., *J. Am. Chem. Soc.* **2003,** *125*, 12337.
39. Mantel, C.; Philouze, C.; Collomb, M. N.; Duboc, C., *Eur. J. Inorg. Chem.* **2004**, 3880.
40. Quee-Smith, V. C.; DelPizzo, L.; Jureller, S. H.; Kerschner, J. L.; Hage, R., *Inorg. Chem.* **1996,** *35*, 6461.
41. Rich, J.; Castillo, C. E.; Romero, I.; Rodríguez, M.; Duboc, C.; Collomb, M. N., *Eur. J. Inorg. Chem.* **2010**, 3658.
42. Romain, S.; Baffert, C.; Duboc, C.; Lepretre, J. C.; Deronzier, A.; Collomb, M. N., *Inorg. Chem.* **2009,** *48*, 3125.
43. Romain, S.; Duboc, C.; Neese, F.; Rivière, E.; Hanton, L. R.; Blackman, A. G.; Philouze, C.; Leprêtre, J.-C.; Deronzier, A.; Collomb, M.-N., *Chem. Eur. J.* **2009,** *15*, 980.
44. Solé, V. A.; Papillon, E.; Cotte, M.; Walter, P.; Susini, J., *Spectrochim. Acta Part B* **2007,** *62*, 63.
45. George, G. N. *EXAFSPAK, SSRL, SLAC*, Stanford University: Stanford, CA, 2000.
46. Becke, A. D., *Am. Phys. Soc.* **1988,** *38*, 3098.
47. Perdew, J. P., *Phys. Rev. B* **1986,** *33*, 8822.
48. Lenthe, E. v.; Avoird, A. v. d.; Wormer, P. E. S., *J. Chem. Phys.* **1998,** *108*, 4783.
49. van Wüllen, C., *J. Chem. Phys.* **1998,** *109*, 392.
50. Pantazis, D. A.; Chen, X. Y.; Landis, C. R.; Neese, F., *J. Chem. Theory Comput.* **2008,** *4*, 908.
51. Klamt, A.; Schüürmann, G., *J. Chem. Soc. Perk. T. 2* **1993**, 799.
52. Hess, B. A.; Marian, C. M.; Wahlgren, U.; Gropen, O., *Chem. Phys. Lett.* **1996,** *251*, 365.
53. Beckwith, M. A.; Roemelt, M.; Collomb, M. N.; DuBoc, C.; Weng, T.-C.; Bergmann, U.; Glatzel, P.; Neese, F.; DeBeer, S., *Inorg. Chem.* **2011,** *50*, 8397.
54. Herrero-Martin, J.; Mirone, A.; Fernandez-Rodriguez, J.; Glatzel, P.; Garcia, J.; Blasco, J.; Geck, J., *Phys. Rev. B* **2010,** *82*.
55. Neese, F. *ORCA-an ab initio,density functional and semiempirical program package*, Version 2.7; University of Bonn: 2010.
56. de Groot, F. M. F., *Coord. Chem. Rev.* **2005,** *249*, 31.
57. George, S. D.; Petrenko, T.; Neese, F., *J. Phys. Chem. A* **2008,** *112*, 12936.
58. George, S. D.; Petrenko, T.; Neese, F., *Inorg. Chim. Acta* **2008,** *361*, 965.

59. Pollock, C. J.; DeBeer, S., *J. Am. Chem. Soc.* **2011**, null.
60. Shannon, R. D., *Acta Crystallogr. Sect. A* **1976,** *32*, 751.
61. Bergmann, U.; Grush, M. M.; Horne, C. R.; DeMarois, P.; Penner-Hahn, J. E.; Yocum, C. F.; Wright, D. W.; Dubé, C. E.; Armstrong, W. H.; Christou, G.; Eppley, H. J.; Cramer, S. P., *J. Phys. Chem. B* **1998,** *102*, 8350.
62. Glatzel, P.; Bergmann, U.; Yano, J.; Visser, H.; Robblee, J. H.; Gu, W. W.; deGroot, F. M. F.; Christou, G.; Pecoraro, V. L.; Cramer, S. P.; Yachandra, V. K., *J. Am. Chem. Soc.* **2004,** *126*, 9946.

CHAPTER THREE

Manganese K-Edge Absorption Spectroscopy as a Probe of the Metal-Ligand Interactions in Coordination Compounds[2]

Introduction

Transition metal K-edge absorption spectroscopy is a powerful tool for the investigation of the electronic and geometric structure of inorganic and bioinorganic coordination compounds.[1-4] It is a highly element-specific technique and therefore has been applied extensively to large systems containing transition metals, such as the active sites of enzymes. In conjunction with other spectroscopic techniques, it provides a means to experimentally assess the oxidation state, spin state, and symmetry of the respective transition metal absorber.[5-9] Transition metal K-edge spectra can be divided into two parts, each containing valuable information about the system under consideration. The extended x-ray absorption fine structure (EXAFS) region at higher energies is used to determine metal to ligand bond distances and coordination numbers of the metal centers. The pre-edge and edge regions of the spectrum, which appear at lower energies, contain information about the electronic structure and geometric parameters such as site symmetry. In most cases, the shape and position of a transition metal K-edge are used as a "fingerprint" for electronic structure parameters, where assignments of oxidation state and spin state are based on empirical comparisons with known model complexes. Nevertheless, extensive efforts have been made using both molecular orbital and multiple scattering based approaches in order to obtain a more quantitative analysis of the edge region. In particular, a recent study by

[2] Adapted with permission from Roemelt, M.; Beckwith, M. A.; Duboc, C.; Collomb, M. N.; Neese, F.; DeBeer, S., *Inorg. Chem.* **2012,** *51*, 680. Copyright 2012 American Chemical Society.

Jaszewski et. al. showed that TD-DFT reproduces the experimentally observed correlation between the Mn oxidation state for Mn K-edge and L-edge rising edge energies.[10] In the current study, the focus is on a detailed analysis of the pre-edge region.

The weak pre-edge features of transition metal K-edge spectra have been analyzed using qualitative arguments such as site symmetry and ligand-field strength for quite some time.[1, 2, 11-14] Recently, a more quantitative approach for the prediction of pre-edge energies and intensities of iron, chlorine and sulfur K-edges for model compounds has been developed using time-dependent density functional theory (TD-DFT).[15-17] Within this approach one solves the time-dependent linear response equations of singly excited Kohn-Sham determinants where only the metal (or ligand) 1s orbital is allowed to donate an electron to the empty valence shell. The method yields transition energies and oscillator strengths for a preset number of excited states, which are all mutually orthogonal to each other. The description of the core hole leads to a systematic error in the absolute transition energies which can be compensated by a constant energy shift.[15] This energy shift is characteristic for each functional and basis set and hence has to be calibrated for different computational approaches.[16, 17]

In this work, the existing method is extended to mononuclear manganese coordination complexes (many of which were also examined previously using XES[18]) in order to make it available for the prediction of XAS spectra of biologically relevant systems such as the oxygen evolving complex of photosystem II (PSII).[19, 20] The method is calibrated for one meta-GGA functional (BP) and three hybrid functionals in conjunction with the triple-zeta basis set TZVP. Furthermore, the interaction of π-donor and acceptor ligands with the central manganese ion is investigated and their effect on the pre-edge and edge region of the XAS spectrum is examined.

Experimental

A set of sixteen mononuclear manganese complexes was selected as a calibration set. The molecular formulas, synthetic procedures and structural references (when available) are given in Table 3.1. The following abbreviations have been used for the ligands: acac = acetyl acetonate; bpea = *N,N*-bis(2-pyridylmethyl)-ethylamine; salen = ethylenebis(salicylimine); tbu_3terpy = 4,4',4"-tritert-butyl-2,2':6',2"-terpyridine; terpy = 2,2':6',2"-terpyridine; tolylterpy = 4'-(4-methylphenyl)-2,2':6',2"-terpyridine; phenylterpy = 4'-phenyl-2,2':6',2"-terpyridine; tpa = tris-2-picolylamine. A schematic representation of the structures is given in Scheme 3.1.

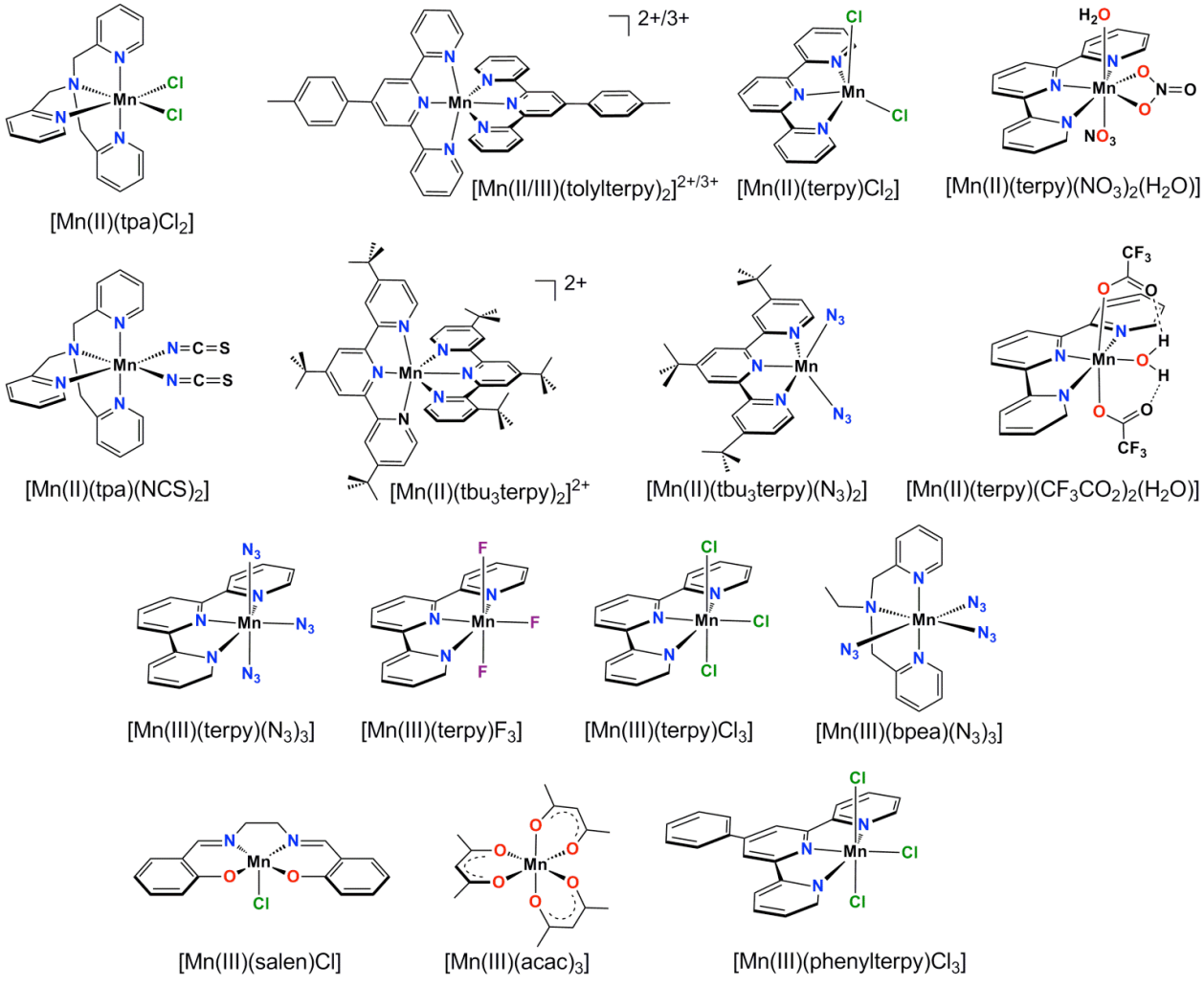

Scheme 3.1. The sixteen mononuclear manganese model complexes investigated in this study.

Sample Preparation

Samples were synthesized according to published procedures by the groups of Drs. Carole Duboc and Marie-Noëlle Collomb, as referenced in Table 3.1.[21-31] All XAS samples were prepared as dilutions in boron nitride, pressed in Al spacers and sealed with 38 micron Kapton windows. All samples were measured at 10 K in a liquid Helium cryostat.

XAS Measurements

All XAS data were recorded at the Stanford Synchrotron Radiation Laboratory (SSRL) on focused beam line 9-3, under ring conditions of 3 GeV and 80-100 mA. A Si(220) monochromator was used for energy selection. A Rh-coated mirror (set to a cutoff of 10 keV) was used for harmonic rejection, in combination with 25% detuning of the monochromator. All data were measured in transmission mode. Internal energy calibration was performed by simultaneous measurement of the absorption of a Mn foil placed between a second and third ionization chamber. The first inflection point of the Mn foil was assigned to 6539.0 eV. Samples were monitored for photoreduction throughout the course of data collection. Only those scans which showed no evidence of photoreduction were used in the final averages. The averaged data were processed as described previously.[32]

Computational Details

All DFT calculations presented in this work were performed using the ORCA program package.[33] Scalar relativistic effects were taken into account at the ZORA level.[34, 35] Open-shell species were treated with the spin-unrestricted Kohn-Sham method. All calculations used dense integration grids (ORCA Grid4).

Geometry optimizations

All molecular geometries were optimized using the BP86 functional[36, 37] together with scalar relativistically recontracted (SARC)[38] all electron def2-TZVP(-f) basis sets.[39] The Coulomb

fitting basis of Weigend[40] was used in uncontracted form. Dichloromethane was chosen as the solvent within the conductor like screening model[41] (COSMO, ε = 9.08). All geometry optimizations except those of [Mn(II)(terpy)$(NO_3)_2(H_2O)$], [Mn(III)(salen)Cl], and [Mn(III)$(acac)_3$] were performed by Michael Roemelt.

XAS Calculations

Manganese K-edge absorption spectra were investigated with a TD-DFT approach applying the Tamm-Dancoff approximation.[42] XAS calculations were performed with the BP[36, 37], B3LYP[43, 44] and the TPSSh[45] functional. XAS calculations using the B3LYP and TPSSh functionals were performed by Michael Roemelt. Additionally, a series of calculations with functionals of a hybrid form were also conducted by Michael Roemelt. More information regarding the hybrid functionals can be found in the reference from which this chapter is adapted.[46] The conductor-like screening model was used to model a solution environment with acetonitrile (ε = 36.6) as the solvent. Absorption spectra were obtained from the TD-DFT calculations by applying a Gaussian fit with a broadening of 1 eV. In calculating the oscillator strength f_{IF} of a given transition between the states $|I\rangle$ and $|F\rangle$, electric dipole, magnetic dipole and electric quadrupole contributions were included[16, 47]:

$$
\begin{aligned}
f_{IF} &= f_{IF}^{ed} + f_{IF}^{md} + f_{IF}^{eq} \\
f_{IF}^{ed} &= \frac{2}{3} E_{FI} \left| \langle I | \hat{\boldsymbol{\mu}} | F \rangle \right|^2 \\
f_{IF}^{md} &= \frac{2}{3} \alpha^2 E_{FI} \left| \langle I | \hat{\boldsymbol{M}} | F \rangle \right|^2 = \frac{2}{3} \alpha^2 E_{FI} \left| \langle I | \sum_i \frac{1}{2} \left(\hat{\boldsymbol{l}}(i) + 2\hat{\boldsymbol{s}}(i) \right) | F \rangle \right|^2 \\
f_{IF}^{eq} &= \frac{1}{20} \alpha^2 E_{FI}^3 \sum_{a,b}^{x,y,z} \left| \langle I | \hat{Q}_{ab} | F \rangle \right|^2
\end{aligned}
\tag{3.1}
$$

Here, E_{FI} is the transition energy and α the fine structure constant, whereas $\hat{\boldsymbol{\mu}}, \hat{\boldsymbol{M}}$ and $\hat{\boldsymbol{Q}}$ denote the electric dipole, magnetic dipole and electric quadrupole moments operators,

respectively. The calculated intensity of a given feature is obtained from the sum of the squares of transition moments of all contributing excited states:

$$I = c\sum_{F}\left(f_{0F}^{ed}\right)^2 + \left(f_{0F}^{md}\right)^2 + \left(f_{0F}^{eq}\right)^2 \tag{3.2}$$

Where $c = \frac{1}{4.33\cdot 10^{-9}}\frac{1}{\sqrt{\pi}}\frac{2\sqrt{\log 2}}{FWHM}$ and FWHM is the broadening factor which was chosen to be 1 eV.

Results and Analysis

The transition energies and intensities for the experimentally obtained Mn K-edge spectra of the sixteen model complexes, and the corresponding calculated parameters using the B3LYP functional together with the computational model described above, are summarized in Table 3.1. The calculated parameters using the functionals BP86, TPSSh and a purpose specific functional (BLYP + 22% HF exchange) described below, can be found in Table 3.2.

Table 3.1. Comparison of Experimental Energies and Intensities to Calculated Values using the B3LYP functional.

	Experimental			**Calculated**		
Compound	Energy (eV)	Area[a]	Reference[b]	Energy (eV)[c]	Intensity	Predicted Experimental Area[d]
$[Mn(III)(acac)_3]$	6540.2	4.5	-	6540.4	0.28	3.5
	6542.2	1.6		6541.9	0.14	2.6
$[Mn(III)(bpea)(N_3)_3]$	6540.5	4.8	21	6540.4	0.35	3.9
$[Mn(III)(phenylterpy)Cl_3]$	6540.3	3.8	22	6540.4	0.23	3.1
	6541.8	0.4		6541.6	0.10	2.4
[Mn(III)(salen)Cl]	6540.6	13.2	-	6541.2	2.04	14.0
	6542.6	0.6		6542.8	0.18	2.9
$[Mn(III)(terpy)Cl_3]$	6540.2	5.5	22	6540.4	0.24	3.2
$[Mn(III)(terpy)F_3]$	6540.7	4.2	21	6540.4	0.24	3.2
	6541.9	1.2		6541.9	0.31	3.7
$[Mn(III)(terpy)(N_3)_3]$	6540.2	4.1	23	6540.4	0.30	3.6
$[Mn(III)(tolylterpy)_2]^{3+}$	6540.1	6.0	24	6540.1	0.42	4.3
	6541.8	1.5		6542.0	0.13	2.6
$[Mn(II)(tbu_3terpy)_2]^{2+}$	6540.0	9.4	25	6540.1	0.95	7.5
$[Mn(II)(tbu_3terpy)(N_3)_2]$	6540.2	12.6	26	6540.2	1.92	13.3
$[Mn(II)(terpy)Cl_2]$	6540.2	11.0	27	6540.2	1.48	10.7
$[Mn(II)(terpy)(NO_3)_2(H_2O)]$	6540.3	5.9	28	6540.2	0.91	7.2
$[Mn(II)(CF_3CO_2)_2(terpy)(H_2O)]$	6540.2	8.1	29	6540.2	0.59	5.4
$[Mn(II)(tolylterpy)_2]^{2+}$	6540.0	8.4	24, 30	6540.1	0.92	7.3
$[Mn(II)(tpa)Cl_2]$	6540.2	5.5	31	6540.3	0.51	4.8
$[Mn(II)(tpa)(NCS)_2]$	6540.0	4.0	25	6539.9	0.34	3.8
	6541.0	1.8		6540.8	0.55	5.1

[a]Experimental areas have been multiplied by 100.
[b]Synthesis and crystallographic structure references.
[c]The calculated energies have been shifted by 32.6 eV to higher energies.
[d]The predicted experimental area, A, is obtained from the calculated intensity, I, according to $A = 6.01 \bullet I + 1.79$.

Figure 3.1a contains a comparison of the experimental transition energies and their calculated counterparts using the B3LYP functional. In previous studies, it has been established that a constant shift of the calculated energies accounts for most of the systematic error made by the TD-DFT method.[15-17] The exact size of the shift is dependent on the computational method and therefore the shift has to be calibrated for each combination of functional and basis set. A regression analysis of the data leads to an average energy shift of 32.6 eV (±0.2 eV). It should be noted that for the evaluation of this shift, only transitions with dominant 1s to 3d character (*vide infra*) were taken into account. Figure 3.1b shows the relationship between the experimental and B3LYP calculated intensities of the pre-edge transitions. The linear relationship gives a correlation constant of R = 0.90. This is somewhat inferior to the correlation obtained for the transition energies but is still considered satisfactory (Table 3.1). The comparisons of the experimental energies and areas to those calculated using the BP86, TPSSh, and the purpose specific (BLYP + 22% HF exchange) functionals are shown in Figures 3.2-3.4.

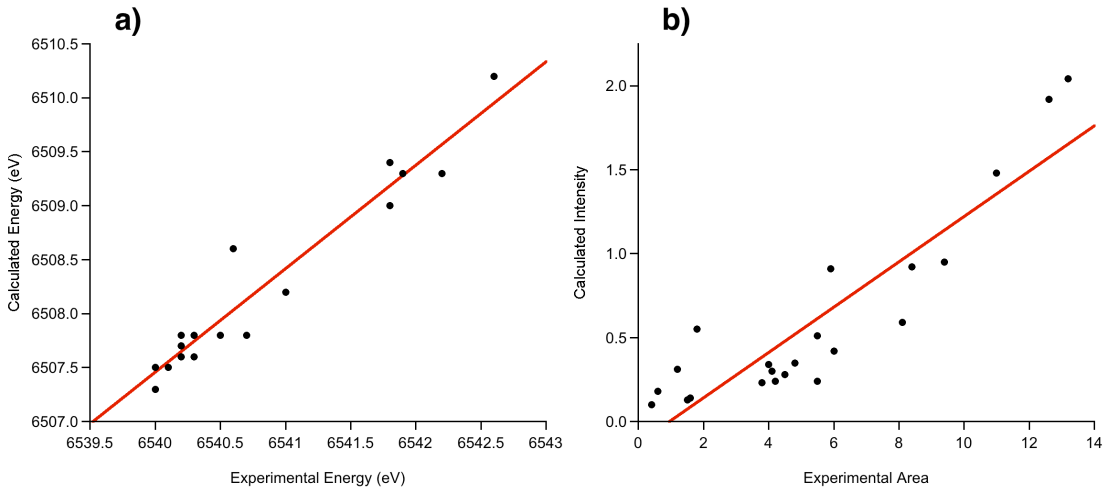

Figure 3.1. Relationship of calculated to experimentally determined transition energies (a) and intensities (b). The calculations used the B3LYP functional. The linear least squares fits are given by: $f^{a)} = 0.948E(\text{exp}) + 318.62\ eV$ and $f^{b)} = 0.135A(\text{exp}) - 0.129$.

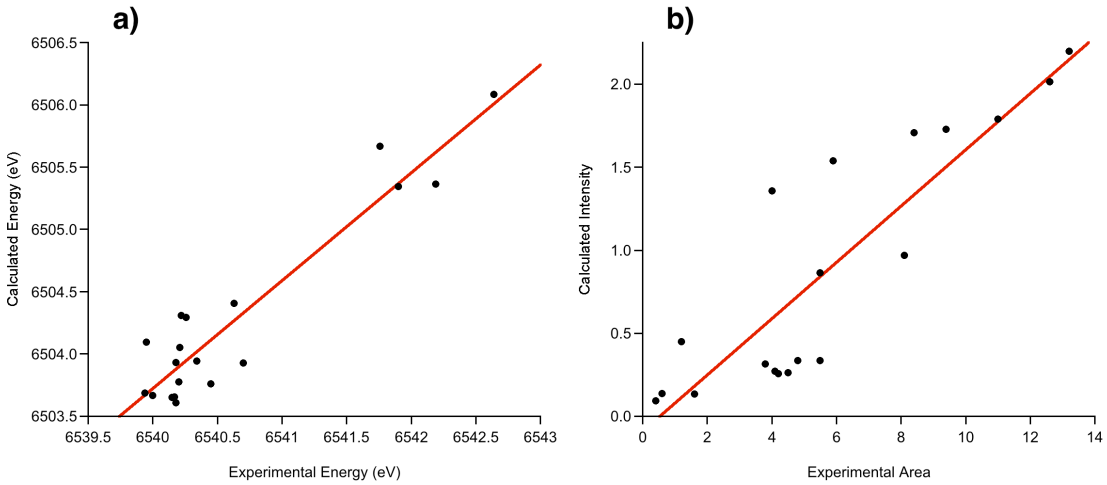

Figure 3.2. Relationship of calculated to experimentally determined transition energies (a) and intensities (b) using the TPSSh functional. The linear least squares fits are given by: $f^{a)} = 0.865E(\text{exp}) + 845.75\ eV$ (R = 0.94) and $f^{b)} = 0.169A(\text{exp}) + 0.089$ (R = 0.88).

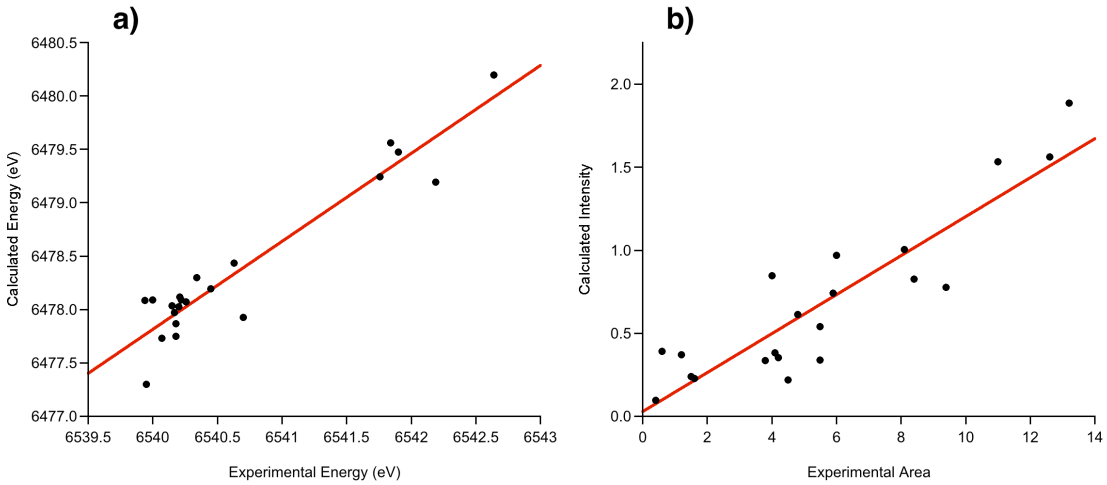

Figure 3.3. Relationship of calculated to experimentally determined transition energies (a) and intensities (b) using the BP functional. The linear least squares fits are given by: $f^{a)} = 0.824E(\text{exp}) + 1088.52\ eV$ (R = 0.95) and $f^{b)} = 0.117A(\text{exp}) + 0.028$ (R = 0.90).

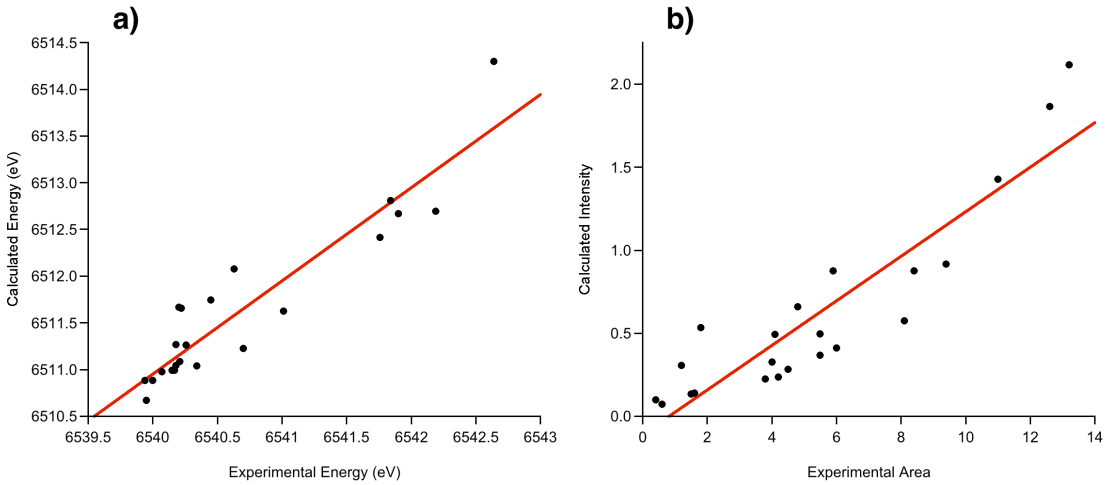

Figure 3.4. Relationship of calculated to experimentally determined transition energies (a) and intensities (b) using the BLYP functional with 22% admixed HF exchange (see text). The linear least squares fits are given by: $f^{a)}$ = 0.996E(exp) – 2.18 eV (R = 0.93) and $f^{b)}$ = 0.134A(exp) - 0.110 (R = 0.91).

Table 3.2. XAS calculated area fits and energy shifts for the TPSSh, BP, BLYP(22%), and B3LYP functionals

Functional	Calculated area fit line	R value	Energy shift (eV)
TPSSh	A = 4.52 I + 1.74	0.88	36.3
BP	A = 6.88 I + 0.87	0.90	62.3
BLYP(22%)	A = 6.11 I + 1.63	0.91	29.1
B3LYP	A = 6.01 I + 1.79	0.90	32.6

Symmetry and ligand field effects on the 1s to 3d transitions

In a previous study of the pre-edges of several Fe-compounds, the relationship between the shape and intensity of the pre-edges and the geometric and electronic structure of the complexes was examined.[15] Similar arguments hold for the present series of Mn complexes. Figure 3.5 shows the comparison of the measured (a) and calculated (b) pre-edges of representative members of the calibration series. Comparisons for the remaining compounds are shown in Figures 3.6-3.8.

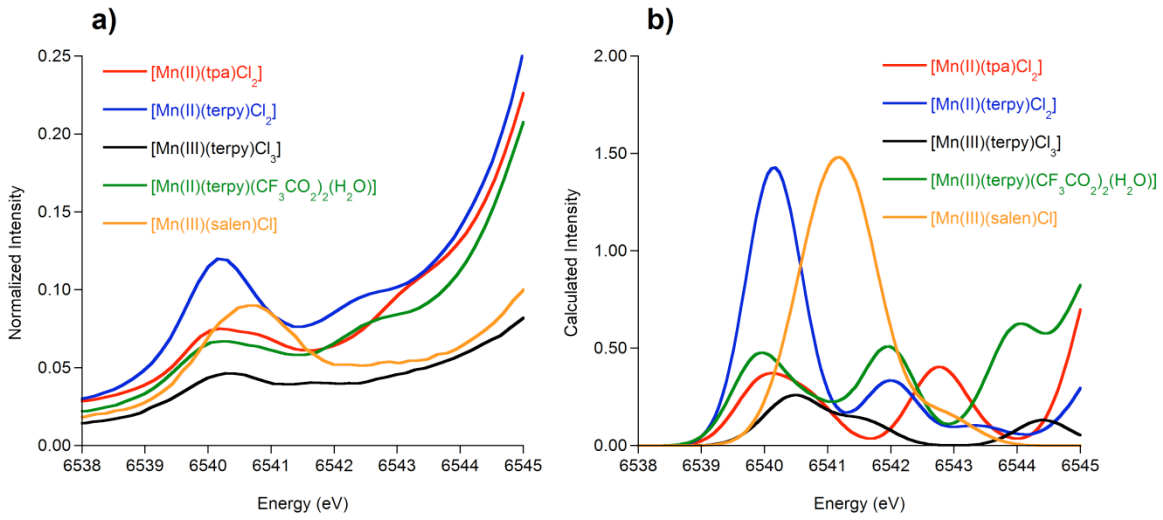

Figure 3.5. Experimental (a) and calculated (b) K pre-edge regions of various Mn-complexes highlighting the influence of geometrical parameters such as coordination number and geometry on the pre-edge intensity. The calculations used the B3LYP functional and a 32.6 eV energy shift and 1 eV broadening have been applied to all calculated spectra.

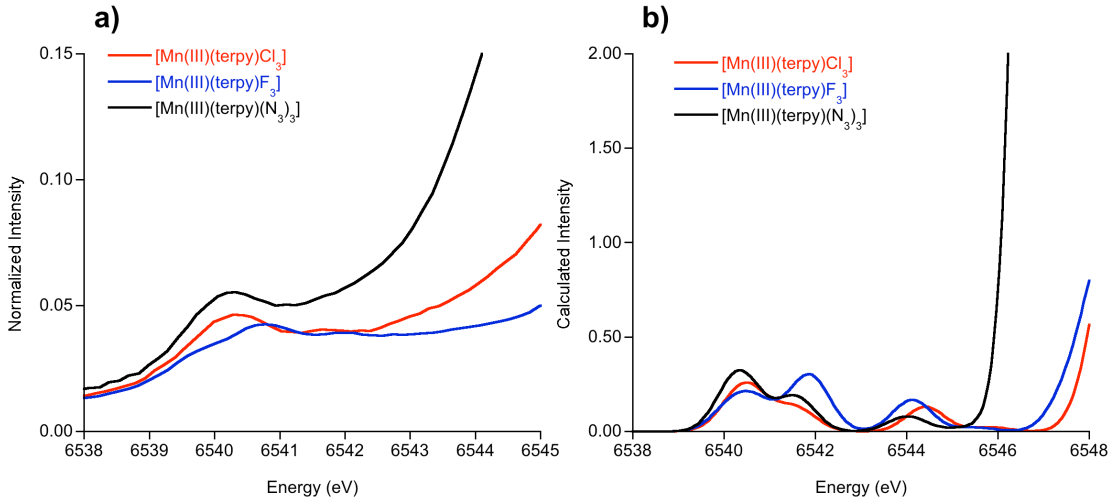

Figure 3.6. Comparison of measured (a) and calculated (b) XAS pre-edge spectra of [Mn(III)(terpy)Cl_3] (red), [Mn(III)(terpy)F_3] (blue), and [Mn(III)(terpy)$(N_3)_3$] (black). The calculations used the B3LYP functional and a 32.6 eV energy shift and 1 eV broadening have been applied to all calculated energies.

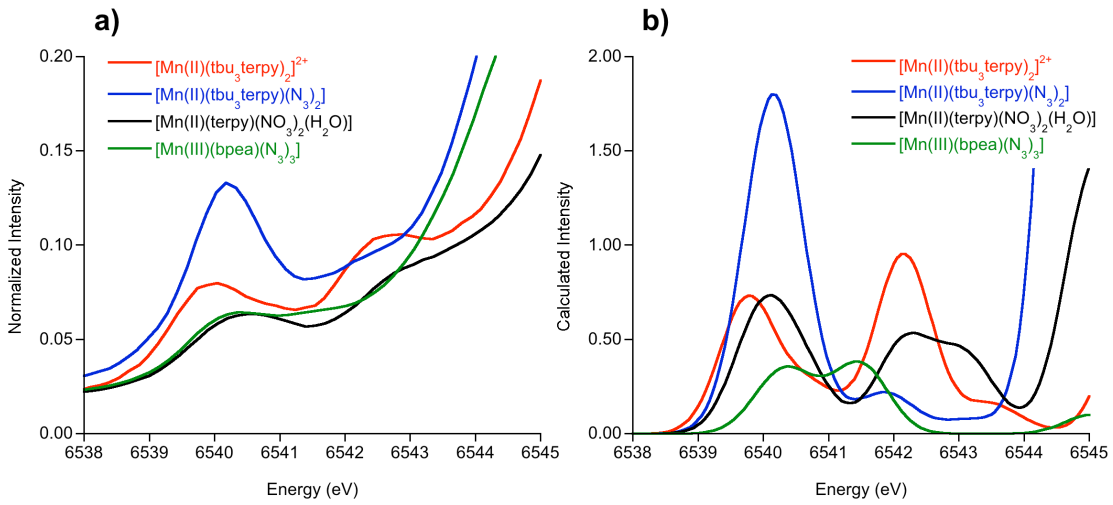

Figure 3.7. Comparison of measured (a) and calculated (b) XAS pre-edge spectra of $[Mn(II)(tbu_3terpy)_2]$ (red), $[Mn(II)(tbu_3terpy)(N_3)_2]$ (blue), $[Mn(II)(terpy)(NO_3)_2(H_2O)]$ (black), and $[Mn(III)(bpea)(N_3)_3]$ (green). The calculations used the B3LYP functional and a 32.6 eV energy shift and 1 eV broadening have been applied to all calculated energies.

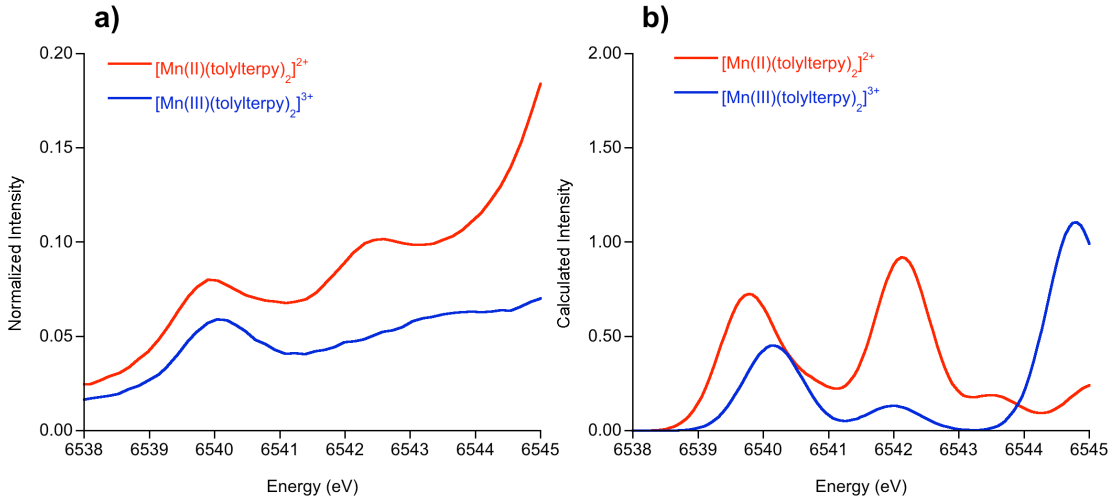

Figure 3.8. Comparison of measured (a) and calculated (b) XAS pre-edge spectra of $[Mn(II)(tolylterpy)_2]^{2+}$ (red) and $[Mn(III)(tolylterpy)_2]^{3+}$ (blue). The calculations used the B3LYP functional and a 32.6 eV energy shift and 1 eV broadening have been applied to all calculated energies.

On the basis of these spectra, some general trends may be noted. The two complexes $[Mn(II)(terpy)Cl_2]$ and $[Mn(III)(terpy)Cl_3]$ differ by both the oxidation state and spin state of the

central Mn ion $\left(S\left(Mn^{II} \right) = \frac{5}{2} \text{ and } S\left(Mn^{III} \right) = 2 \right)$, and more importantly by the number of ligands and their coordination geometry. [Mn(III)(terpy)Cl_3] is six-coordinate whereas [Mn(II)(terpy)Cl_2] is five-coordinate. Despite their chemical difference, the six ligating atoms (3 x N and 3 x Cl) of [Mn(III)(terpy)Cl_3] together form a slightly distorted octahedral environment around the central Mn^{3+} ion. The coordination sphere of the distorted square planar [Mn(II)(terpy)Cl_2] complex on the other hand is arranged such that the two chloro ligands are above and below the plane that is described by the terpy ligand, with a Cl-Mn-Cl angle of 114.9 degrees.

The pre-edges of both [Mn(III)(terpy)Cl_3] and [Mn(II)(terpy)Cl_2] each exhibit two features, one at 6540.2 eV and the other one to higher energy (~6542.3 eV). According to the calculations, the former is assigned as a standard Mn 1s to Mn 3d pre-edge transition, which gains some intensity due to Mn 4p mixing. The second peak corresponds to a metal-to-ligand charge-transfer (MLCT) transition that will be discussed in detail in the next section.

The 1s to 3d transition of [Mn(II)(terpy)Cl_2] is ~2.5 times more intense than that for [Mn(III)(terpy)Cl_3] in the experimental spectra. In the calculated spectra, the difference is even more pronounced with an intensity ratio of 3.3 (Figure 3.5 and Table 3.1). This significant increase in pre-edge intensity for [Mn(II)(terpy)Cl_2] is readily attributed to the change in the coordination geometry. The 4p mixing into the Mn 3d-shell is more pronounced in square pyramidal geometry than in octahedral geometry, so the pre-edge transitions acquire more allowed electric dipole character in square pyramidal geometry, and an increase in pre-edge intensity. [47,12,2]

Similar observations can be made for the pre-edge of the six-coordinate [Mn(II)(tpa)Cl_2] complex, which has the same oxidation and spin state as the five-coordinate [Mn(II)(terpy)Cl_2] complex. It also has two pre-edge features, one corresponding to Mn 1s to 3d transitions (6540.2

eV) and the other due to MLCT processes (6543.2 eV). Due to the distorted octahedral coordination geometry of [Mn(II)(tpa)Cl_2], the low energy pre-edge feature has a low intensity compared to the five-fold coordinated [Mn(II)(terpy)Cl_2]. Analogously the square pyramidal coordination geometry of [Mn(III)(salen)Cl] leads to an enhanced pre-edge intensity. Thus, the present test set nicely confirms the generally accepted notion that six-coordinate complexes give rise to less intense pre-edge features than their five-coordinate counterparts.[1, 2, 11]

All measured and calculated spectra exhibit two or more features in the pre-edge region. The TD-DFT methodology readily allows for the assignment of the observed transitions. For most of the investigated compounds, the 1s to 3d transitions all contribute to a single pre-edge feature with one resolved maximum. This is because the "ligand field splitting" between the different final states arising from the $1s^1 3d^{N+1}$ configuration is smaller than the experimental resolution of around 1 eV (Figure 3.5). Only compounds with strong ligand fields exhibit two or more 1s to 3d features. In the present series of compounds only [Mn(III)$(acac)_3$], [Mn(III)(terpy)F_3], [Mn(III)(salen)Cl], [Mn(III)(phenylterpy)Cl_3], [Mn(III)$(tolylterpy)_2]^{3+}$ and [Mn(II)(tpa)$(NCS)_2$] show two resolved 1s to 3d bands in their pre-edge spectra (Figure 3.9).

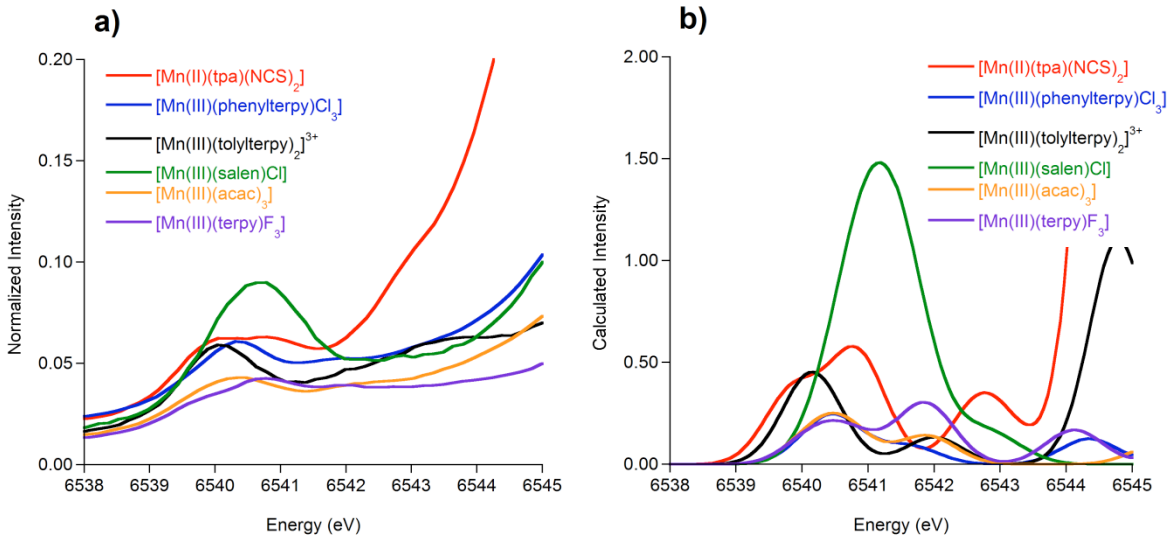

Figure 3.9. Experimental (a) and calculated (b) K pre-edge regions of various Mn-complexes highlighting their relatively strong ligand field. The calculations used the B3LYP functional and a 32.6 eV energy shift and 1 eV broadening have been applied to all calculated spectra.

Most of these complexes contain a Mn^{3+} ion, which is consistent with the generally larger ligand field strength in Mn^{3+} complexes as compared to Mn^{2+} complexes. For example, the experimental spectrum of [Mn(III)$(acac)_3$] shows two features with their maxima at 6540.2 eV and 6542.2 eV, corresponding to transitions into the t_{2g} and e_g derived molecular orbitals. This corresponds to a ligand field splitting of 2.0 eV.

As is well known, the spin-polarized picture does not properly resolve all of the final state multiplets.[48, 49] In terms of the spin-polarized description, however, the excited state corresponding to the alpha 1s to t_{2g} transition is lowest in energy, thus contributing to the first experimentally observed feature. This can be explained by the strong spin polarization apparent in d^4 high-spin complexes. The same qualitative order of states was found for all complexes exhibiting two 1s to 3d features. For [Mn(III)$(acac)_3$] the employed TD-DFT method underestimates the splitting of the 1s to 3d features by 0.5 eV (calculated at 6540.4 eV and 6541.9 eV, vs. 6540.2 and 6542.2 eV from experiment, Table 3.1). Similar observations are made for [Mn(III)(phenylterpy)Cl_3], [Mn(III)$(tolylterpy)_2]^{3+}$ and [Mn(III)(salen)Cl] where TD-

DFT underestimates the splitting by 0.3 eV, 0.4 eV and 0.8 eV, respectively (Table 3.1). The ligand field splitting for [Mn(II)(tpa)$(NCS)_2$] is much better reproduced by TD-DFT with experimental and calculated values of 1.0 eV and 0.9 eV, respectively. The experimental spectrum of [Mn(III)(terpy)F_3] exhibits three distinguishable 1s to 3d features. This remarkable observation is due to relatively short Mn-F bond distances (with optimized bond distances of 1.83 Å), which in turn lead to a strong ligand field. Again, TD-DFT underestimates the ligand field splitting resulting, in this particular case, in a qualitatively incorrect spectrum with only two resolved 1s to 3d features. Nevertheless, the theoretical results for the well-localized transitions into the predominantly empty metal 3d-orbitals are reasonable to good. Problems became apparent with charge transfer transitions as will be described in the next paragraph.

Ligands with extended π-systems

The experimental and calculated XAS pre-edge region of [Mn(II)(terpy)Cl_2] is shown in Figure 3.10a and b. This molecule will serve as an example to gain insight into the nature of the predicted spectra for the class of compounds containing ligands that have extended, arylic π-systems. Similar results are obtained for complexes that contain the acac, tpa, phenylterpy, tolylterpy or tbu_3terpy ligands. These ligands are primarily of π-donor character but nevertheless have low-lying empty π^* orbitals.

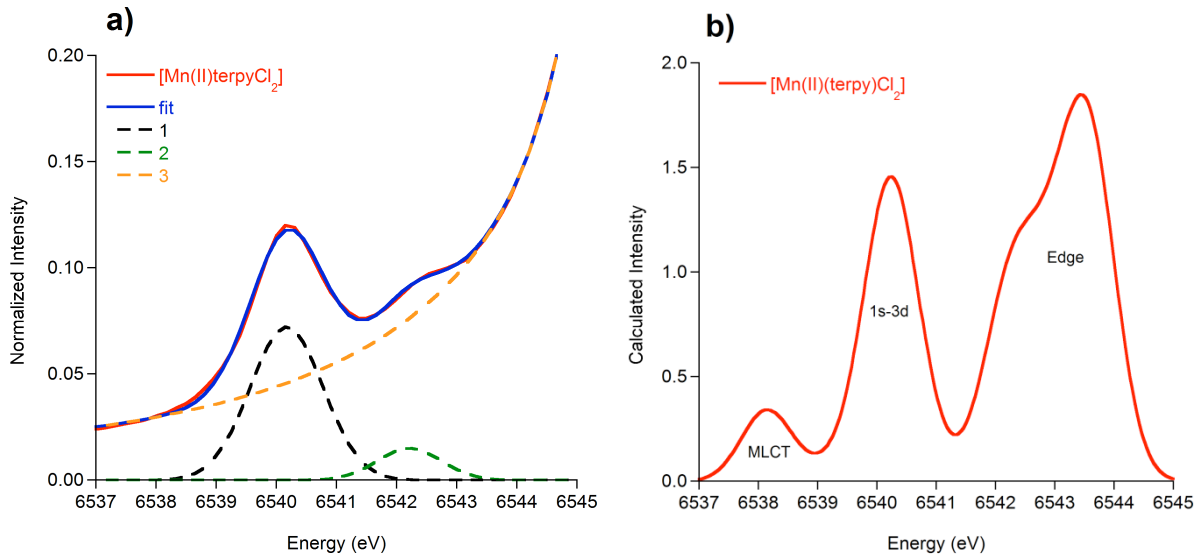

Figure 3.10. Experimental (a) and calculated (b) pre-edge spectra of [Mn(II)(terpy)Cl_2]. The dashed lines in the experimental spectrum represent the individual pre-edge (green and black dashed lines) and background components (orange dashed line) of the fit. The fit to the pre-edge comprises two features, one intense metal 1s to 3d peak at lowest energy (black dashed line) and a weak MLCT peak to higher energy (green dashed line). The calculation used the BP86 functional and hence the MLCT absorption occurs at lower energies. A 62.3 eV energy shift and 1 eV broadening have been applied to the calculated spectrum.

In order to emphasize certain aspects of the TD-DFT method, a spectrum that was calculated with a non-hybrid density functional (BP86) is presented. Both the experimental and calculated spectra exhibit two features that are separated by 2 eV. In the experimental spectrum, the more intense peak is situated at lower energy, whereas in the calculated spectrum the relative intensities of the two resolved peaks are reversed. This erroneous behavior is due to the well-known fact that TD-DFT has severe problems with excited states of charge transfer character. Depending on the system and the amount of exact exchange in the functional, such transitions can appear several eV too low in the calculated spectra. This is well known from valence excited states in the UV and visible regions of the spectrum,[50, 51] but appears to also hold for XAS calculations. The same behavior is seen here, where the extended π-systems of the ligands give rise to charge transfer artifacts or what will also be referred to as "ghost-states". The effect of increasing the amount of HF exchange on the predicted pre-edge spectrum of [Mn(II)(terpy)Cl_2] is demonstrated in Figure 3.11 where the fraction of HF exchange varies from 0% to 30%.

The most obvious effect is that the absolute transition energies increase with increasing amount of HF exchange. Secondly, the rising edge feature becomes more pronounced, which is due to the fixed number of calculated roots (40). Since the number of calculated "ghost-states" is reduced as the amount of HF exchange is increased,[50] more states that belong to the edge feature of the spectrum are included in the calculation. Hence, the calculated edge feature gains intensity when more HF exchange is present. The most important effect for the present work, however, is that the MLCT feature in the calculated spectrum is – as expected – shifted relative to the 1s-3d absorption to higher energies. In addition, the intensity of the MLCT-feature is slightly reduced with increasing amount of HF exchange. A detailed analysis of this series and a similar study for $[Mn(II)(tolylterpy)_2]^2$, which has a more pronounced MLCT feature, revealed that an admixture of 22% HF exchange yields the best results in terms of energy splitting and intensity ratio. This will be further addressed in the conclusion section.

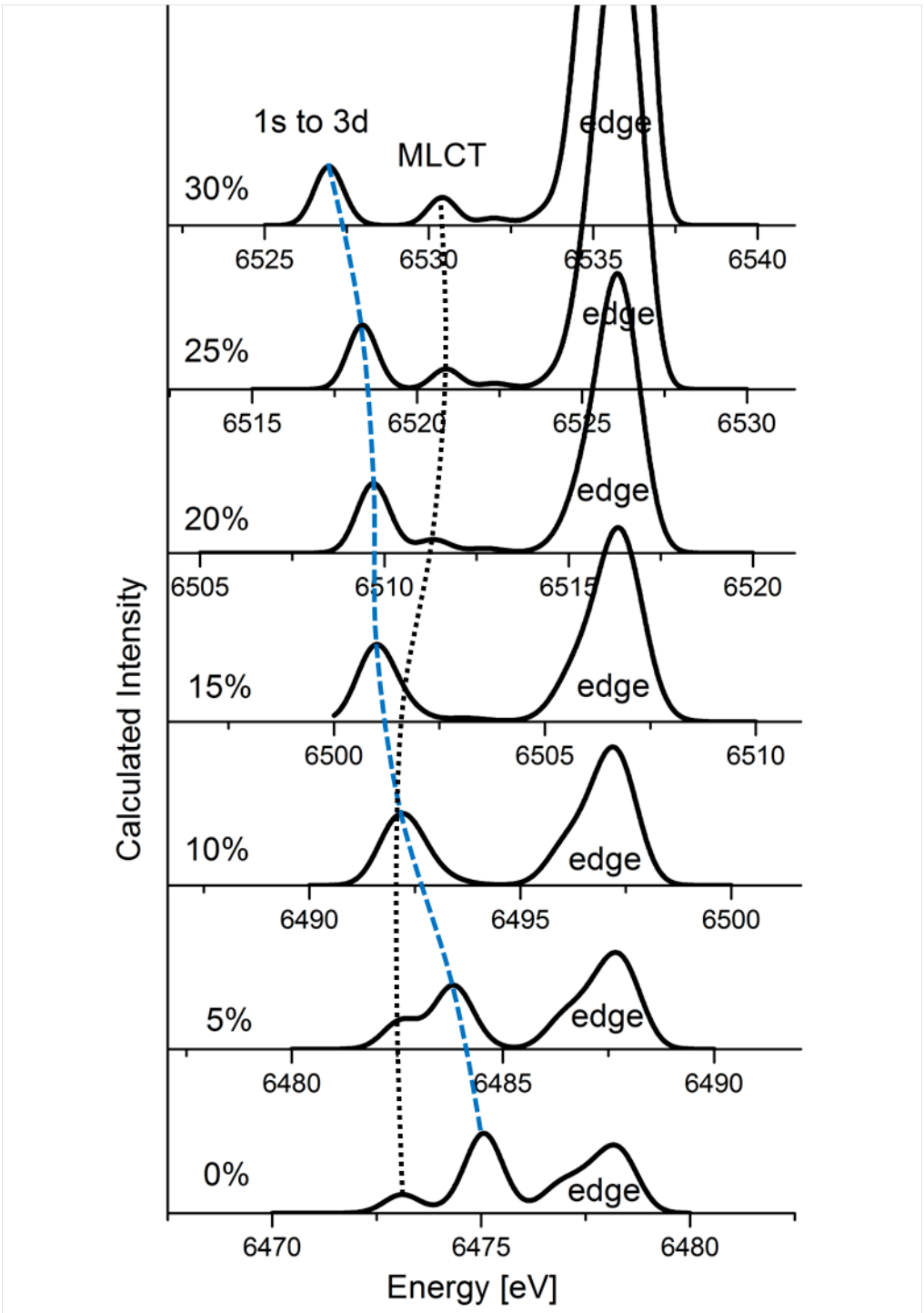

Figure 3.11. Calculated spectra of [Mn(II)(terpy)Cl_2] using a series of functionals that each contain a different amount of HF exchange (e.g. TPSSh contains 10% HF exchange and B3LYP contains 20% HF exchange). Starting with no HF exchange, the percentage increases in steps of 5% up to a maximum of 30% HF exchange. It is seen that the position of the MLCT peak (black dotted line) relative to the 1s to 3d peak (blue dashed line) changes from lower in energy (0%, 5%) to the same energy (10%, 15%) to higher energy (20% and higher) depending on the amount of HF exchange.

Effect of π-acceptor ligands

Pre-edge spectra of compounds containing ligands with considerable π-acceptor character such as N_3^- or SCN^- exhibit remarkable features in the rising edge-region of the Mn K-edge XAS spectra. Figure 3.12 shows the experimental and calculated spectra of [Mn(II)(tpa)Cl_2] and [Mn(II)(tpa)$(NCS)_2$]. The calculated spectrum of [Mn(II)(tpa)$(NCS)_2$] shows a strong feature at high energy that appears as a shoulder on the rising edge in the experimental spectrum. In the calculations, these features can be reproduced even within a relatively small number of calculated excited states. A proper reproduction of the rising edge features is unfortunately not feasible with the restrictions imposed by standard basis sets and DFT potentials.

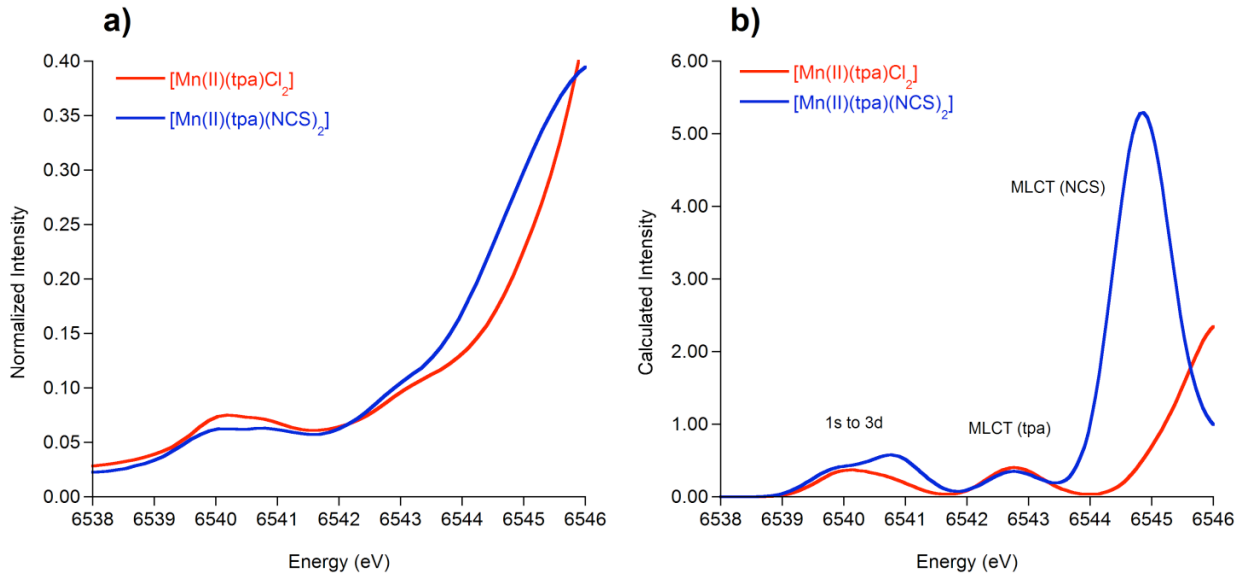

Figure 3.12. Experimental (a) and calculated (b) pre-edge spectra of [Mn(II)(tpa)Cl_2] and [Mn(II)(tpa)$(NCS)_2$]. The calculations used the B3LYP functional and a 32.64 eV energy shift and 1 eV broadening have been applied to the calculated spectra. Both spectra exhibit features corresponding to Mn 1s to 3d transitions around 6540.5 eV and a MLCT band at ~6542.8 eV. Only the spectrum of [Mn(II)(tpa)$(NCS)_2$] has an additional, intense MLCT band at 6545 eV due to transitions into π-orbitals of the SCN^- ligand. The high energy feature at 6546 eV of [Mn(II)(tpa)Cl_2] is a small part of the rising edge.

According to the calculations, the excited states that correspond to this strong feature have dominantly MLCT character. However, they are one order of magnitude more intense than the "ghost" MLCT transitions described in the previous section of this chapter. This finding can be

rationalized by the nature of the acceptor orbitals that are associated with the excited states. The acceptor orbitals associated with strong features have mostly SCN^- π-antibonding character. Strong metal-to-ligand backbonding interactions lead to mixing of metal d- and p- orbitals with the empty ligand orbitals. Hence, transitions from the metal 1s orbital to these orbitals gain intensity. Similar observations have been made for [Mn(III)(bpea)$(N_3)_3$], [Mn(III)(terpy)$(N_3)_3$] and [Mn(II)(tbu_3terpy)$(N_3)_2$]. Due to the MLCT character of the excited states that lead to the features discussed here, their predicted transition energies suffer from the same problems of the DFT method as those described above.

Conclusions

In this work, the previously reported method of calculating XAS K-edge pre-edge spectra with a simple TD-DFT protocol has been extended to Mn K-edges using different density functionals. It was found that, as for iron, chlorine, and sulfur K-edges,[15-17] the shape, intensity, and position of Mn 1s to 3d transitions is well predicted by TD-DFT. However, here it has been shown that the prediction of MLCT transitions is more problematic and may lead to significant artifacts in the calculated spectra. The current series of mononuclear coordination compounds contains many examples of ligands that interact with the central manganese ion via π-orbitals. Among this set one can discriminate between ligands with extended, arylic π-systems and genuine π-acceptor ligands such as the azide or thiocyanate ion. The former give rise to rather weak features 1-3 eV higher in energy than the main metal 1s to 3d peak. Although their exact position in the calculated spectrum is highly dependent on the amount of HF exchange incorporated in the functional and is by no means predictive, their existence and appearance is reproduced qualitatively correctly. It has to be noted that in the case of calculations with the TPSSh functional, the MLCT transitions for some of these systems coincide with the metal 1s to 3d

peak. This may lead to an incorrect number of peaks in the calculated spectrum (i.e. one feature as opposed to two; see Figure 3.11 panel with 10% HF exchange). Ligands of primarily π-acceptor character cause intense absorptions at high energies, which appear as clearly visible shoulders of the edge. These features are well reproduced by the TD-DFT method although their predicted position deviates in some cases from the measured values. Spectra calculated with 22% of exact exchange match the experimental spectra well. However, such agreement is treacherous. It is well known from the closely related problems of hyperfine structure or spin-state energetics calculations, that there is not a single fraction of HF exchange that is universally applicable to complexes containing different metals in different oxidation states.[52] In this respect, one should rather be aware of the shortcomings of the functionals used, which means that for XAS calculations one has to be careful when calculating spectra for complexes with extended π-ligand systems. As in many other instances, the 20% exact exchange used in the B3LYP functional appears to be a sensible compromise.

The present work lays the foundation of the application of the TD-DFT methodology to highly important problems in manganese biochemistry, foremost of course the tetranuclear manganese cluster in PSII. However, before this problem can be successfully addressed it must be proven that the methodology is applicable to spin-coupled oligonuclear systems. It should be noted that the issue with the TD-DFT methodology for extended π-ligand systems should not be problem for the OEC of PSII.

References

1. Roe, A. L.; Schneider, D. J.; Mayer, R. J.; Pyrz, J. W.; Widom, J.; Que, L., *J. Am. Chem. Soc.* **1984,** *106*, 1676.
2. Westre, T. E.; Kennepohl, P.; DeWitt, J. G.; Hedman, B.; Hodgson, K. O.; Solomon, E. I., *J. Am. Chem. Soc.* **1997,** *119*, 6297.
3. Grunes, L., *Phys. Rev. B* **1983,** *27*, 2111.
4. Dau, H.; Iuzzolino, L.; Dittmer, J., *BBA-Bioenergetics* **2001,** *1503*, 24.
5. Berry, J. F.; Bill, E.; Bothe, E.; DeBeer George, S.; Mienert, B.; Neese, F.; Wieghardt, K., *Science* **2006,** *312*, 1937.
6. Berry, J. F.; DeBeer George, S.; Neese, F., *Phys. Chem. Chem. Phys.* **2008,** *10*, 4361.
7. Song, W. J.; Seo, M. S.; DeBeer George, S.; Ohta, T.; Song, R.; Kang, M.-J.; Tosha, T.; Kitagawa, T.; Solomon, E. I.; Nam, W., *J. Am. Chem. Soc.* **2007,** *129*, 1268.
8. Shadle, S. E.; Penner-Hahn, J. E.; Schugar, H. J.; Hedman, B.; Hodgson, K. O.; Solomon, E. I., *J. Am. Chem. Soc.* **1993,** *115*, 767.
9. Aliaga-Alcalde, M.; DeBeer George, S.; Mienert, B.; Bill, E.; Wieghardt, K.; Neese, F., *Angew. Chem. Int. Ed.* **2005,** *44*, 2908.
10. Jaszewski, A. R.; Stranger, R.; Pace, R. J., *J. Phys. Chem. A* **2008,** *112*, 11223.
11. Randall, C. R.; Shu, L.; Chiou, Y.-M.; Hagen, K. S.; Ito, M.; Kitajima, N.; Lachicotte, R. J.; Zang, Y.; Que, L., *Inorg. Chem.* **1995,** *34*, 1036.
12. Shulman, G.; Yafet, Y.; Eisenberger, P.; Blumberg, W., *Proc. Natl. Acad. Sci. U. S. A.* **1976,** *73*, 1384.
13. Hahn, J. E.; Scott, R. A.; Hodgson, K. O.; Doniach, S.; Desjardins, S. R.; Solomon, E. I., *Chem. Phys. Lett.* **1982,** *88*, 595.
14. Dräger, G.; Frahm, R.; Materlik, G.; Brümmer, O., *Phys. Status Solidi B* **1988,** *146*, 287.
15. DeBeer George, S.; Petrenko, T.; Neese, F., *J. Phys. Chem. A* **2008,** *112*, 12936.
16. DeBeer George, S.; Petrenko, T.; Neese, F., *Inorg. Chim. Acta* **2008,** *361*, 965.
17. DeBeer George, S.; Neese, F., *Inorg. Chem.* **2010,** *49*, 1849.
18. Beckwith, M. A.; Roemelt, M.; Collomb, M. N.; DuBoc, C.; Weng, T.-C.; Bergmann, U.; Glatzel, P.; Neese, F.; DeBeer, S., *Inorg. Chem.* **2011,** *50*, 8397.
19. Yano, J.; Kern, J.; Sauer, K.; Latimer, M. J.; Pushkar, Y.; Biesiadka, J.; Loll, B.; Saenger, W.; Messinger, J.; Zouni, A.; Yachandra, V. K., *Science* **2006,** *314*, 821.
20. Yano, J.; Yachandra, V. K., *Inorg. Chem.* **2008,** *47*, 1711.
21. Mantel, C.; Hassan, A. K.; Pécaut, J.; Deronzier, A.; Collomb, M. N.; Duboc-Toia, C., *J. Am. Chem. Soc.* **2003,** *125*, 12337.
22. Mantel, C.; Chen, H. Y.; Crabtree, R. H.; Brudvig, G. W.; Pécaut, J.; Collomb, M. N.; Duboc, C., *ChemPhysChem* **2005,** *6*, 541.
23. Limburg, J.; Vrettos, J. S.; Crabtree, R. H.; Brudvig, G. W.; Paula, J. C. d.; Hassan, A.; A.-L.Barra; Duboc-Toia, C.; Collomb, M.-N., *Inorg. Chem.* **2001,** *40*, 1698.
24. Romain, S.; Duboc, C.; Neese, F.; Rivière, E.; Hanton, L. R.; Blackman, A. G.; Philouze, C.; Leprêtre, J.-C.; Deronzier, A.; Collomb, M.-N., *Chem. Eur. J.* **2009,** *15*, 980.
25. Duboc, C.; Collomb, M. N.; Pécaut, J.; Deronzier, A.; Neese, F., *Chem.-Eur. J.* **2008,** *14*, 6498.
26. Mantel, C.; Philouze, C.; Collomb, M. N.; Duboc, C., *Eur. J. Inorg. Chem.* **2004**, 3880.
27. Mantel, C.; Baffert, C.; Romero, I.; Deronzier, A.; Pécaut, J.; Collomb, M. N.; Duboc, C., *Inorg. Chem.* **2004,** *43*, 6455.
28. Baffert, C.; Romero, I.; Pécaut, J.; A.Llobet; Deronzier, A.; Collomb, M.-N., *Inorg. Chim. Acta* **2004,** *357*, 3430.

29. Rich, J.; Castillo, C. E.; Romero, I.; Rodríguez, M.; Duboc, C.; Collomb, M. N., *Eur. J. Inorg. Chem.* **2010**, 3658.
30. Romain, S.; Baffert, C.; Duboc, C.; Lepretre, J. C.; Deronzier, A.; Collomb, M. N., *Inorg. Chem.* **2009,** *48*, 3125.
31. Duboc, C.; Phoeung, T.; Zein, S.; Pécaut, J.; Collomb, M.-N.; Neese, F., *Inorg. Chem.* **2007,** *46*, 4905.
32. Ray, K.; DeBeer George, S.; Solomon, E. I.; Wieghardt, K.; Neese, F., *Chem.-Eur. J.* **2007,** *13*, 2783.
33. Neese, F. *ORCA-an ab initio,density functional and semiempirical program package*, Version 2.7; University of Bonn: 2010.
34. Lenthe, E. v.; Baerends, E. J.; Snijders, J. G., *J. Chem. Phys.* **1993,** *99*, 4597.
35. van Wüllen, C., *J. Chem. Phys.* **1998,** *109*, 392.
36. Becke, A. D., *Am. Phys. Soc.* **1988,** *38*, 3098.
37. Perdew, J. P., *Phys. Rev. B* **1986,** *33*, 8822.
38. Pantazis, D. A.; Chen, X. Y.; Landis, C. R.; Neese, F., *J. Chem. Theory Comput.* **2008,** *4*, 908.
39. Weigend, F.; Ahlrichs, R., *Phys. Chem. Chem. Phys.* **2005,** *7*, 3297.
40. Weigend, F., *Phys. Chem. Chem. Phys.* **2006,** *8*, 1057.
41. Klamt, A.; Schüürmann, G., *J. Chem. Soc. Perk. T. 2* **1993**, 799.
42. Hirata, S.; Head-Gordon, M., *Chem. Phys. Lett.* **1999,** *314*, 291.
43. Becke, A. D., *J. Chem. Phys.* **1993,** *98*, 5648.
44. Lee, C. T.; Yang, W. T.; Parr, R. G., *Phys. Rev. B* **1988,** *37*, 785.
45. Staroverov, V. N.; Scuseria, G. E.; Tao, J.; Perdew, J. P., *J. Chem. Phys.* **2003,** *119*, 12129.
46. Roemelt, M.; Beckwith, M. A.; Duboc, C.; Collomb, M. N.; Neese, F.; DeBeer, S., *Inorg. Chem.* **2012,** *51*, 680.
47. Griffith, J. S., *The Theory of Transition Metal Ions*. Cambridge University Press: Cambridge, 1964.
48. Neese, F.; Petrenko, T.; Ganyushin, D.; Olbrich, G., *Coord. Chem. Rev.* **2007,** *251*, 288.
49. Tchougréeff, A. L.; Ángyán, J. G., *Int. J. Quantum Chem.* **2010,** *110*, 454.
50. Neese, F., *J. Biol. Inorg. Chem.* **2006,** *11*, 702.
51. Tozer, D. J., *J. Chem. Phys.* **2003,** *119*, 12697.
52. Neese, F., *Coord. Chem. Rev.* **2009,** *253*, 526.

CHAPTER FOUR

Resolving the Protonation States of a bis-μ-oxo Bridged Mn(IV) Dimer using X-ray Absorption and Emission Spectroscopy[3]

Introduction

Reactions involving protonation or deprotonation of metal centers in bioinorganic catalysts are important processes that govern the catalyzed reaction chemistry. In addition, protonation states of bridging and terminal oxo ligands can also control catalytic function. This is most often accomplished by changing the charge density distribution and/or covalency between the metals and ligands, and the pKa of bound water/hydroxide, upon oxygen protonation. For example, the O2 activation catalyzed by ribonucleotide reductase is possibly accompanied by protonation state changes at the bridging oxygens of RNR,[1] and protonated copper oxo complexes (oxo, hydroxo, peroxo) are important in respiration (e.g. hemocyanin), and in C-H bond activation mechanisms (e.g. methane monooxygenase catalyst).[2, 3] In the oxygen-evolving complex (OEC) of photosystem II (PSII), which catalyzes the photosynthetic water oxidation reaction to produce atmospheric oxygen, protonation state changes of both the bridging and terminal oxo ligands have been proposed during the reaction mechanism, which has yet to be fully understood.

Although the high-resolution crystal structure of the OEC published in 2011 clarified many questions concerning the nuclearity and connectivity of the Mn_4CaO_x cluster,[4] there are multiple reasons why the protonation states of the bridging and terminal oxygens[5, 6] remain elusive. At 1.9

[3] Adapted from Krewald, V.; Lassalle-Kaiser, B.; Boron III, T. T.; Kern, J.; Beckwith, M. A.; Yachandra, V. K.; Pecoraro, V. L.; Yano, J.; Neese, F; DeBeer, S. (submitted for publication) and from Lassalle-Kaiser, B.; Boron III, T. T.; Krewald, V.; Kern, J.; Beckwith, M. A.; Schroeder, H.; Alonso-Mori, R.; Nordlund, D.; Weng, T.-C.; Sokaras, D.; Neese, F.; Bergmann, U.; Yachandra, V. K.; DeBeer, S.; Pecoraro, V. L.; Yano, J. (submitted for publication).

Å, the resolution of the crystal structure is too low to show the electron densities belonging to the hydrogen atom, especially in the vicinity of elements with much higher masses. A known problem in probing samples of the OEC with spectroscopy or diffraction is the constant reassembly and activity of the cluster. Moreover, the x-rays are expected to photoreduce the cluster,[7] leading to a structure that is not necessarily identical with one of the S-states of the Kok cycle. Thus there are multiple structures being probed at once, and differences in the protonation pattern may exist. In order to understand the mechanisms carried out by the OEC and other enzyme active sites, techniques with enough sensitivity to distinguish between structures that only differ by a single proton are required.

Since protons are chemically extremely relevant with respect to structure and reactivity, there are methods that can indirectly elucidate protonation state. A proton, as a Lewis acid, will lengthen bonds and this can be observed in the XRD pattern.[8] This bond lengthening of protonated species may also be observed in extended x-ray absorption fine structure (EXAFS) spectra, as the proton not only changes bond distances, but also the variance in bond distances (reflected in the Debye-Waller factors) that is partially responsible for the amplitude of the EXAFS spectra. As it interferes with the electronic structure of the possibly magnetically interacting chemical entity, the proton will also affect exchange pathways, thus leading to altered isotropic exchange coupling constants. More specifically, in EPR spectroscopy, these altered isotropic exchange coupling constants can result in differences in the observed hyperfine splitting pattern of the spectra. Information on protonation states can also be obtained from other EPR techniques such as HYSCORE.[9]

To understand the effects of protonation on high-valent Mn(IV) centers which are presumed to be present during the catalytic cycle of the OEC, a study concerning the chemistry, structure, and magnetism of $[Mn_2(IV)(\mu\text{-}O)_2(salpn)_2]$ and its homologues was published.[10] To the author's best

knowledge, it was and remains the first set of manganese complexes where three protonation states of the oxo bridges could be isolated without changes in the oxidation state of either of the Mn centers. This research was founded on earlier investigations showing the parent complex to be similar to elements of the OEC with respect to Mn-Mn distances and the alternative substrate H_2O_2 catalase activity.[11-13] A strong link between the protonation and redox chemistry of this compound was found. The transformation from $[Mn_2(IV)(\mu\text{-}O)_2(salpn)_2]$ to $[Mn_2(IV)(\mu\text{-}O)(\mu\text{-}OH)(salpn)_2]^+$ can occur in the presence of a weak acid such as the pyridinium ion, but is influenced by possible substitutions of the salpn ligand affecting the electron-donating or withdrawing character. The isotope shift of the O-H stretch frequency after labeling the oxo bridges with ^{18}O in the study by Baldwin et al. showed that the protonation occurs at the oxo bridges. With two equivalents of a stronger acid added to $[Mn_2(IV)(\mu\text{-}O)_2(salpn)_2]$, the doubly protonated species $[Mn_2(IV)(\mu\text{-}OH)_2(salpn)_2]^{2+}$ can be produced.

X-ray techniques other than x-ray diffraction, namely x-ray absorption and emission spectroscopy (XAS and XES, respectively), are also sensitive enough to distinguish between different protonation states as will be shown in this chapter. There are significant advantages to using XAS and XES over the EPR techniques mentioned above, including that they are element specific and not restricted by the spin state of the metal. This is especially advantageous for large protein clusters that contain many different types of atoms, and that in some cases contain different metal atoms in a single cluster.

Experimental and Computational Methodology

Contributions of coauthors of the manuscripts from which this chapter was adapted are noted throughout. The role of the author was in analysis and fitting of the XAS and XES data.

Synthesis and sample preparation

The compounds were synthesized by the group of Dr. Junko Yano following the procedure of Baldwin et. al.[10] The purity of the compounds was checked via comparison of UV-Visible and XAS spectra with previously published data. Samples were diluted with boron nitride and then pressed into Al spacers and sealed with Kapton tape.

XAS measurements

The XAS measurements were performed by the group of Dr. Junko Yano at the Stanford Sychrotron Radiation Laboratory (SSRL) on beamline 7-3, under ring conditions of 3.0 GeV with an average current of 90 mA. The intensity of the incident x-ray beam was monitored by an N_2-filled ion chamber (I_0) in front of the sample. The radiation was monochromatized by a Si(220) double-crystal monochromator and data were collected as fluorescence excitation spectra with a Ge 30 element detector (Canberra). The energy was calibrated using the pre-edge peak of $KMnO_4$ (6543.3 eV). The standard used for internal energy calibration was placed between two N_2-filled ionization chambers (I_1 and I_2) after the sample, which was kept at a temperature of 10 K in a liquid helium flow cryostat to minimize radiation damage. The x-ray flux at 6.4 to 7.1 keV was between 2 to 5.10^7 photons s^{-1} mm^{-2} of the sample.

XES measurements

The XES measurements were also performed by the group of Dr. Junko Yano on beamline 6-2 at SSRL using an operating ring current of 300 mA. The incident photon energy was set to 10.4 keV using the monochromator of two cryogenically cooled Si(111) crystals. Horizontal and vertical focusing mirrors were used to focus the x-ray beam to 0.7 x 1 mm. Data were collected at 10 K in a continuous flow liquid helium cryostat and calibrated to the first moment of the $K\beta_{1,3}$ peak of Mn_2O_3 at 6490.4 eV.

The XES spectra were recorded using a high-resolution crystal-array spectrometer using the 440 reflection of 14 spherically bent Si(110) crystals (100 mm diameter, 1 m radius of curvature) aligned on intersecting Rowland circles.[14] An energy-resolving Si drift detector was positioned at the focus of the 14 diffracting elements. The spectrometer energy was calibrated by measuring the energy of the elastically scattered beam as a function of spectrometer position. A He filled polyethylene bag was placed between the cryostat and the spectrometer to minimize signal attenuation due to air absorption.

Analysis of XAS and XES Spectra

The x-ray absorption XANES regions and the XES spectra were fit using the program BlueprintXAS.[15, 16] For each compound, 100 fits were generated, and the best fits out of these were averaged for the final analysis. For the XAS data, both the pre-edge and edge regions of the spectra were fit simultaneously, and at least 30 reasonable fits were included for a statistically significant average. The reported peak areas and intensity-weighted average energies are those of the best-fit averages. All of the spectra were normalized to an edge intensity of 1 based on the intensity value of the edge region fit component. The pre-edge areas were obtained from the BlueprintXAS program and subsequently multiplied by 100.

For the XES data, both the Kβ main line and valence to core regions were fit simultaneously, and at least 30 reasonable fits were included for a statistically significant average. The reported peak areas and intensity-weighted average energies are those of the best-fit averages. All of the emission spectra are normalized to a total integrated area of 1000. More details on the fitting procedure can be found in Appendix A.

Computational Details

The DFT calculations were performed by Vera Krewald using the ORCA progam package. Scalar relativistic effects were taken into account with the 0th order regular approximation for

relativistic effects[17, 18] (ZORA), and solvation effects were modeled with the conductor-like screening model[19] (COSMO). A tight integration grid (ORCA Grid4) was used in all calculations. Geometry optimizations for the four molecules were based on the crystal structure with the appropriate number and position of the protons added. Following previously published procedures,[20, 21] the geometry optimizations were performed at the high spin state with an **ε** value of 8 within COSMO to simulate a protein environment, and with the van der Waals correction[22-24] implemented in ORCA. For these calculations, the BP86 functional[25, 26] was combined with the scalar-relativistically recontracted Karlsruhe triple-z def2-TZVP(-f) basis set[27, 28] including the auxiliary basis set because the Resolution of the Identity approximation was employed.

For the calculation of Mn K-edge XANES, the TD-DFT approach with the Tamm-Dancoff approximation was chosen.[29] The TPSSh functional[30] and the RIJCOSX[31] approximation were used with the same basis set combination as for the geometry optimizations. Acetonitrile was chosen as the solvent within COSMO (ε = 36.6) in accordance with previous employed protocols. For each Mn center, 100 roots were calculated to cover a sufficient energy range to compare reliably with experiment. Following the protocol published previously, the donor orbitals were localized and the acceptor orbitals were chosen to be the whole virtual space. The computed spectra were shifted by 36.27 eV to higher energy and broadened by 1.5 eV.

The method for calculating XES spectra has been published and tested.[32, 33] This study follows the latter publication in correcting the molecular orbitals for spin-orbit coupling, with the spin-orbit mean-field approximation (SOMF) for the SOC operator. The BP86 functional with def2-TZVP(-f) and def2-TZV/J basis sets and a solvent model for dichloromethane (COSMO, ε = 9.08) was used here. The resulting computed spectra were shifted by 59.2 eV to higher energy and broadened by 3.5 eV.

Details on the analysis of the calculated spectra and the correlation to experiment

The calculated XAS and XES spectra were analyzed with procedures described previously, resulting in intensity-weighted average energies (IWAE) and calculated areas that are directly comparable to the respective experimental data.[29, 33] Since contributions from two donor sites are considered in both the XAS and XES calculations, the values for the intensities were divided by two in order to match the experimental normalization procedure of normalizing to a single Mn center. The assignment of the calculated XAS is based on a difference-density approach, since with the functional TPSSh more than one acceptor orbital (commonly two to six, with varying coefficients) is found to be important for describing the character of the transition modeled with the TDDFT approach. A difference density can be understood as the density of the donor orbitals minus the density of the combined acceptor orbitals. For the assignment of the calculated XES, an analysis of the donor orbitals is sufficient to understand the character of the spectral features since the emission spectra are modeled using a one-electron picture.

Results and Analysis

Computational Structures

The crystal structure of $[Mn_2(IV)(\mu\text{-}O)_2(salpn)_2]$[11, 12] served as a starting point for all structural models discussed here. Four molecular cores can be deduced from structure **1** by protonation steps: a singly protonated structure, **2**, and two doubly protonated isomers **3a** and **3b**. The respective cores and their characteristic interatomic distances and angles are presented in Figure 4.1. Note that there is no relevant displacement of the Mn centers from the plane defined by the bridging O atoms and the N and O atoms of the ligand. Compound **1** has a $Mn_2(\mu\text{-}O)_2$ core with standard Mn-Mn and Mn-O distances of 2.697 Å and 1.822/1.831 Å. The Mn-O-Mn and O-Mn-

O angles are 95.16° and 84.84°, respectively. After the first protonation step, forming the asymmetrically protonated $Mn_2(\mu\text{-}O)(\mu\text{-}OH)$ core, the whole diamond expands to a Mn-Mn distance of 2.838 Å. The asymmetry is reflected in the increased Mn-O-Mn angle of 102.29° accompanied by the compressed Mn-OH-Mn angle of 92.12°. The symmetric $Mn_2(\mu\text{-}OH)_2$ core **3a** has a Mn-Mn distance increased by 0.17 Å relative to species **2**, and increased by 0.311 Å relative to the unprotonated core, **1**. This is approximately the same increase as found for an asymmetric double protonation of the core, forming compound **3b**, $Mn_2(\mu\text{-}O)(\mu\text{-}OH_2)$. As can be expected, the Mn-O distances increase upon protonation to ~1.97 Å for a bridging hydroxo and 2.20 Å for a bridging aquo ligand. These findings from DFT calculations are in accordance with the results of the EXAFS analysis by Baldwin et al., who reported an increase of the Mn-Mn distance by 0.1 Å for each protonation step.

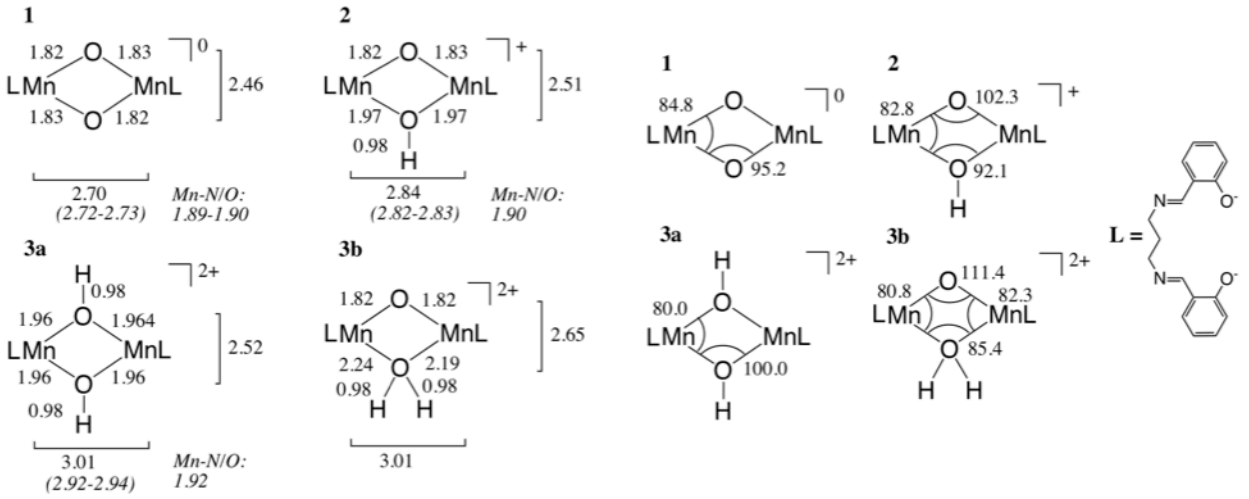

Figure 4.1. Selected interatomic distances (Å, left) and angles (degrees, right) of the cores of the compounds investigated. Distances from EXAFS measurements are given in italics. L represents the *salpn* ligand, shown on the right.

Experimental XAS data

The experimental XANES of compounds **1-3** are displayed in Figure 4.2. All complexes exhibit a steep rising edge feature at ~6553 eV which is due dominantly to dipole allowed Mn 1s-4p transitions. At lower energies (between 6538 and 6545 eV) the pre-edges corresponding to

Mn 1s-3d transitions are observed. For the Mn dimers studied here, the intensities of the white line maximum (at ~6560 eV) deviate, with the intensity of the unprotonated compound **1** being the lowest (~1.1), followed by the protonated compounds **2** (~1.2) and **3** (~1.25). This increase in white line intensity is consistent with what is typically observed for transition metal aquo species, which show very intense white line features.[34] The edge energies do not change significantly across the series (≤0.12 eV based on the edge component of the fits), indicating that the Mn centers are at the same oxidation state in all three complexes. This absence of an edge energy shift is in contrast to what has been observed for a similar protonation series of Fe dimers (protonation of only the oxo-bridge while maintaining the same ligand framework), where the edge shifts to lower energy upon protonation.[34] However, in the case of the Fe complexes, there is a more significant distortion of the $Fe_2(\mu\text{-oxo})(\mu\text{-acetato})_2$ core upon protonation.[35] The Fe-O_{bridge} bond lengths increase and the Fe atoms become less displaced from the ligand plane upon protonation (however the overall Fe atom displacement from the ligand plane remains significant in both complexes). For the series of Mn dimers presented here, the distortion of the $Mn_2(\mu\text{-O})_2$ core is less pronounced: the Mn-O_{bridge} bond lengths do not increase as significantly, and the Mn atoms are not displaced from the ligand plane in any of the three complexes. This could explain the absence of an edge energy shift across the series.

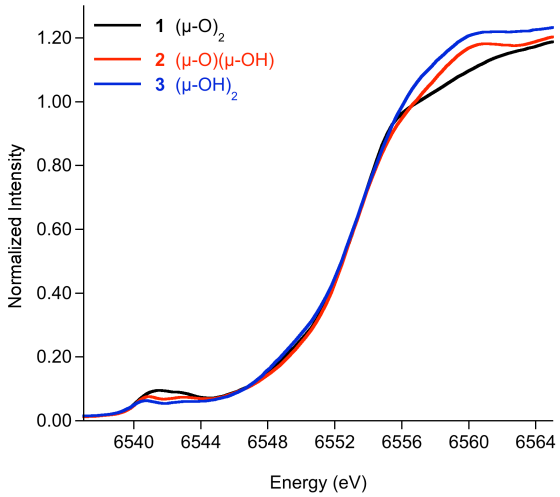

Figure 4.2. XANES of compounds **1** (black), **2** (red) and **3** (blue).

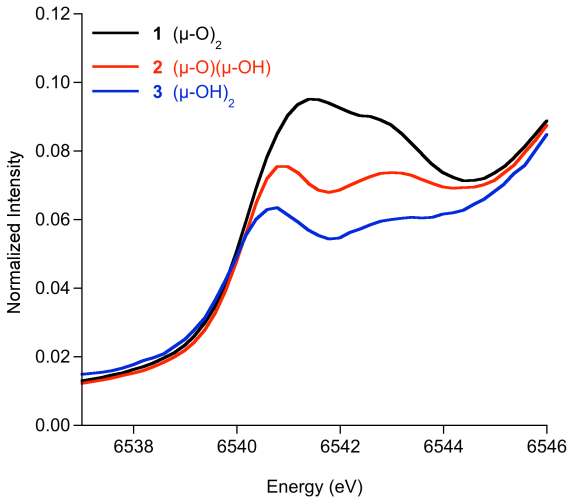

Figure 4.3. Pre-edge region of the x-ray absorption spectra of compounds **1** (black), **2** (red) and **3** (blue).

This study will focus on the pre-edge region (6538-6545 eV) of the XAS spectra (Figure 4.3). Two peaks appear for each compound. The most intense spectrum is that of compound **1**, with **2** being of intermediate intensity and **3** the lowest. Upon protonation of the bridging oxygen atoms, the IWAE of the total pre-edge region decreases slightly (6541.9 to 6541.6 eV). For the single protonation of the $(\mu\text{-O})_2$ bridged complex to the (μ-O)(μ-OH) bridged complex, this decrease is distinctly smaller (0.03 eV) than that of the second protonation step (0.27 eV). As can be deduced from the observations on the intensities, and from the fits shown in Figure 4.4, the pre-edge areas change more significantly. They reduce from 25.7 for compound **1**, to 21.7 and 14.5

for compounds **2** and **3**, respectively. The larger part of this change can be attributed to the decrease in the area of the higher energy feature upon protonation (Figure 4.4 and Table 4.1). This indicates that the pre-edge areas are more useful for determining protonation states of the oxo bridges than the pre-edge energies.

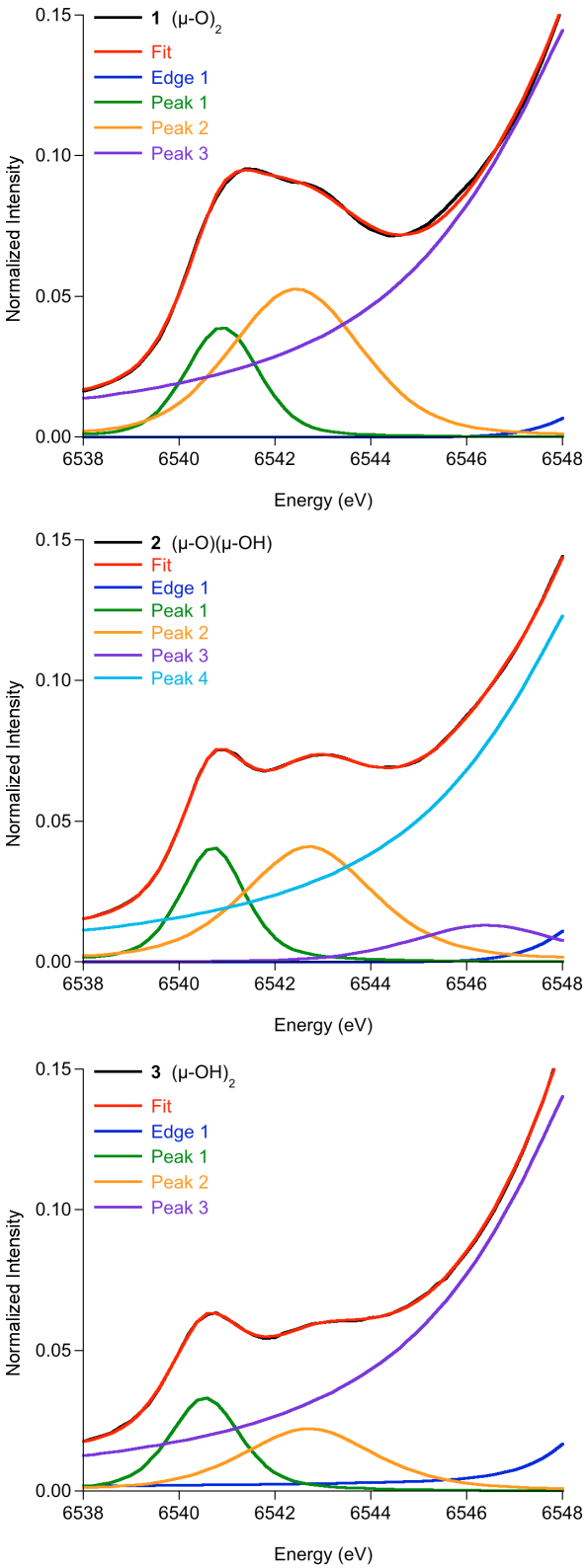

Figure 4.4. Fits to the XAS pre-edge region for compounds **1** (top), **2** (middle) and **3** (bottom).

Table 4.1. Intensity weighted average energies and areas for the total pre-edge regions and individual peaks (1, 2) for the experimental spectra and calculated spectra based on the high spin solution. Calculated spectra IWAEs were shifted by 36.27 eV to higher energy.

	Total		1		2	
	IWAE (eV)	Area[a]	IWAE (eV)	Area[a]	IWAE (eV)	Area[a]
			Experiment			
1	6541.9	25.67	6540.9	7.95	6542.4	17.80
2	6541.9	21.72	6540.7	7.73	6542.7	13.98
3	6541.6	14.50	6540.5	6.82	6542.7	7.67
			Calculation			
1	6542.1	1.72	6541.3	0.79	6542.9	0.93
2	6542.5	1.41	6541.1	0.51	6543.2	0.90
3a	6542.2	1.19	6541.5	0.84	6544.0	0.35
3b	6541.7	3.32	6541.0	2.47	6543.5	0.85

[a]Experimental areas are based on fits to the normalized data, and values were multiplied by 100. Calculated areas are sums of oscillator strengths and normalized to the number of donors.

Calculated XAS

The calculated spectra based on the high spin solution have two features in the pre-edge region between 6538 and 6545 eV, as presented in Figure 4.8. For the $(\mu\text{-O})_2$ bridging motif of complex **1**, the first peak is slightly lower in intensity than the second peak (Table 4.1). Upon protonation, the intensity of the whole pre-edge region decreases for the singly protonated and symmetric doubly protonated structures **2** and **3a**, respectively. This follows the experimental trend, which is most easily seen by comparison to the background-subtracted data in Figure 4.6. However, the intensity of the first feature in the calculated spectrum of complex **2** is lower than that of the second one, whereas complex **3a** has a broad first peak that is higher in intensity than the second peak. The calculated spectrum of the asymmetric doubly protonated core, structure **3b**, has a first peak that is over twice the intensity of that of the unprotonated structure **1**. Therefore, it does not follow the trend of the experimental data and is thus far too intense to represent a realistic structure for the formula $[Mn_2\{OH\}_2(salpn)_2]^{2+}$. The second feature of compound **3b** is approximately the same intensity as the second feature of compound **2**. Conclusions drawn from

the total IWAEs are consistent with those reached from the analysis of the calculated areas: the IWAEs of structures **1**, **2**, and **3a** reproduce the trend in the experimental data, whereas those of **1**, **2**, and **3b** do not. This reinforces that structure **3b** is not a feasible motif for the doubly protonated core.

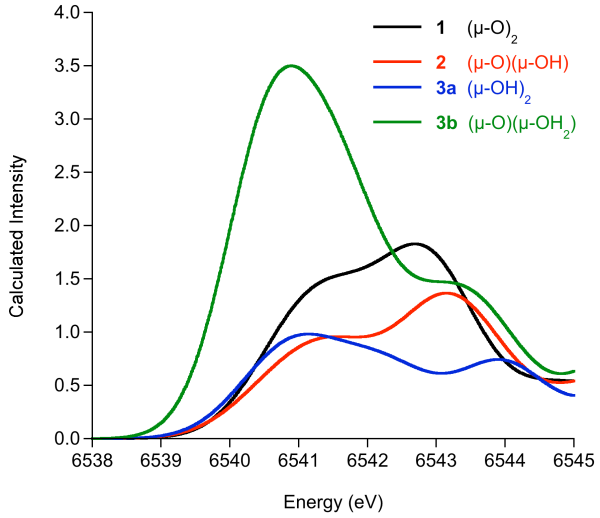

Figure 4.5. Calculated x-ray absorption spectra based on the high-spin solution for compounds **1** (black), **2** (red) and **3a** (blue) and **3b** (green).

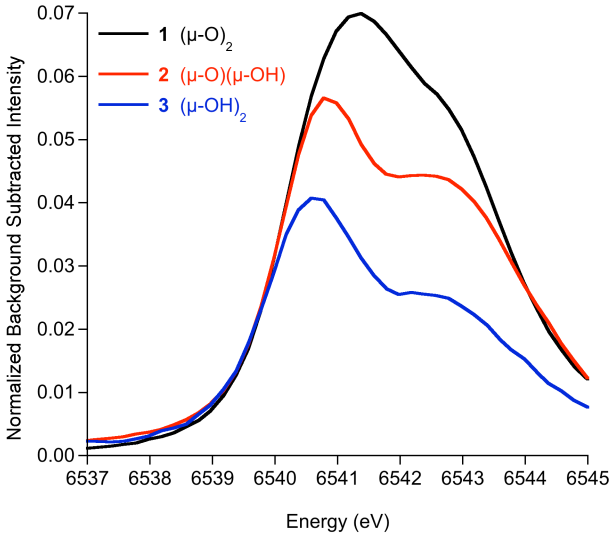

Figure 4.6. Background-subtracted x-ray absorption pre-edge spectra for compounds **1** (black), **2** (red) and **3** (blue).

Assignment of the calculated XAS. The assignments of the peaks for the high spin solution are based on the difference densities of the states forming each feature in the spectrum. This approach has been chosen over a direct analysis of the acceptor orbitals because there are multiple acceptor orbitals for each state. In previous studies, there was one clearly dominant acceptor orbital defining the majority of the transition character. In this study, however, there are at least two (and usually 4-6) acceptor orbitals with significant coefficients, so the character of a state could not be determined in a straightforward manner. The difference density of a state is the difference between the density associated with the donor orbital and the densities associated with the acceptor orbitals. The donor orbital, a 1s orbital, is too small to be represented in the plots. However, the dominant character of the acceptor orbitals can be deduced from these density plots.

In the Mn_2(IV) system with a high-spin $(d^3)_2$ configuration, the β orbitals are all empty. In a coordinate system where the origin is in the center of the $Mn_2(\mu\text{-}O)_2$ diamond with the x-axis towards one Mn atom and the z-axis perpendicular to the plane formed by the $Mn_2(\mu\text{-}O)_2$ core, the occupied α orbitals are of xz, yz and x^2-y^2 character, and the unoccupied α orbitals have z^2 and xy character. These orbital characters are the 'local' characters on the Mn centers, since the origin of the coordinate system does not coincide with either of the metal atoms. In the calculated XAS of compound **1**, four groups of transitions can be identified (Figure 4.7): the transitions into the empty β xz, yz and x^2-y^2 orbitals are at lowest energies followed by transitions into the empty α z^2 and xy orbitals. The latter ones are the most intense in the spectrum and account for most of the character of the first pre-edge feature. The next transitions are those into the β orbitals of z^2 and xy character, while the last group of states has acceptor orbitals from both the α and β set that have xz, yz and x^2-y^2 character mixed with contributions from the ligands.

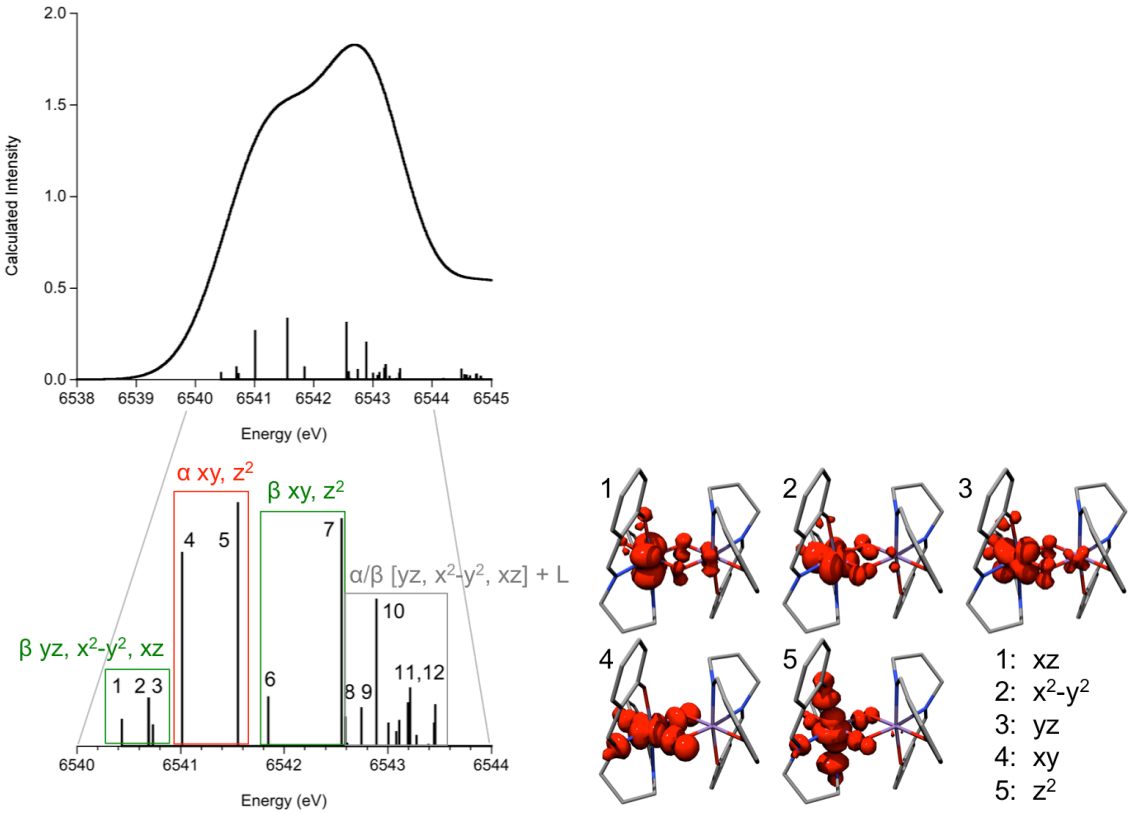

Figure 4.7. Assignment of the calculated pre-edge XAS spectrum of **1** based on the difference densities shown on the right for the first five labeled states. The labels for the local character are in accordance with the coordinate system described in the text.

The same pattern can be observed for the other species, with modifications in the relative intensities and positions of the transitions. Most importantly, in the spectra of species **2** and **3a**, groups of states can be identified that are characterized as MLCT states rather than as states with mixed-in ligand character. As has been stated earlier in Chapter 3, the energetic position of these states depends on the choice of functional.[29] For the calculations in this study that used the TPSSh functional, the transitions into the MLCT states coincide with those of the pre-edge region, which may partially be the reason for the inverted pre-edge peak intensity ratio of the calculated spectra compared to experiment.

The significantly elevated intensity of compound **3b** can be attributed to two transitions in the pre-edge region. The first intense state is due to transitions into α orbitals of xy character, and the

second one is due to transitions into β orbitals of mixed xz, xy and x^2-y^2 character. The difference densities associated with these transitions show that the donor atoms *trans* to the aquo bridge are more strongly involved than the ones *trans* to the oxo bridge, which contribute very little intensity.

Experimental XES data

The emission spectra consist of the main line, which consists of the Kβ' (lower energy) and $K\beta_{1,3}$ (higher energy, most intense) features, and the valence to core region, which occurs at higher energies and is significantly less intense than the main line. The main lines for the Mn(IV) dimer series studied here are shown in Figure 4.8. Figure 4.9 shows the valence to core region. The main line extends from 6472 to 6500 eV, and the valence to core region from 6510 to 6540 eV. There is a small shift of the $K\beta_{1,3}$ feature to higher energy upon protonation of the bridging oxygen atoms, however with the magnitude being less than 0.2 eV at each protonation step it is not sufficiently significant to correspond to changes in the Mn oxidation states, thus confirming the analysis of the XAS edge energy changes. It was shown previously that the dominant factor increasing the $K\beta_{1,3}$ energy for Mn monomers is an increased 3p-3d exchange.[33] Since the 3p-3d exchange can be linked to covalency, it is worthwhile to consider the changes in covalency across the series. At each protonation step, the covalency of the core decreases: the $(\mu\text{-}O)_2$ core is the most covalent and the $(\mu\text{-}OH)_2$ core the least covalent. The decrease in covalency of the bridging motifs should increase the 3p-3d exchange interaction across the series, which may explain the slightly larger observed splitting of the Kβ' and $K\beta_{1,3}$ features upon protonation.

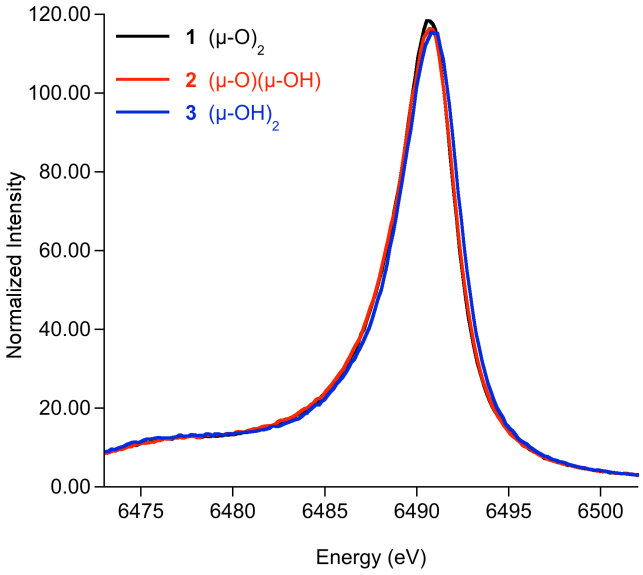

Figure 4.8. Kβ main line region of the x-ray emission spectra of compounds **1** (black), **2** (red) and **3** (blue).

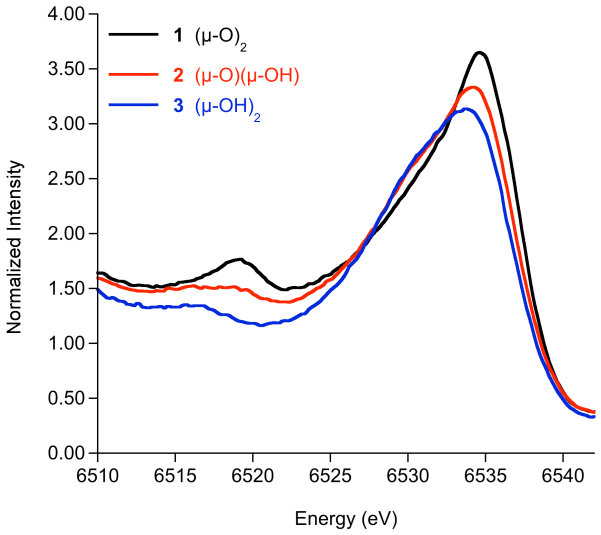

Figure 4.9. Valence to core region of the x-ray emission spectra of compounds **1** (black), **2** (red) and **3** (blue).

The valence to core region features two characteristic peaks, the Kβ'' (satellite) at 6511-6521 eV and the $K\beta_{2,5}$ at 6521-6540 eV (Figure 4.9). The energies of both features shift to lower energies upon protonation. In addition, the intensities of both features decrease upon protonation, with a shoulder growing concurrently at the lower-energy side of the $K\beta_{2,5}$ peak for compounds **2** and **3**.

The fits to the XES data (Figure 4.10) are composed of a background, which is the sum of the contributions from the Kβ main line features (Kβ' and $K\beta_{1,3}$), and four to five features in the valence to core region. Using the IWAEs and areas of the fits, the observations based on Figure 4.7 can be quantified. Upon protonation of the bridging oxygens, the IWAE of the total valence to core region increases slightly, from 6531.1 eV ($(\mu\text{-O})_2$) to 6531.4 eV ((μ-O)(μ-OH)) and 6533.2 eV ($(\mu\text{-OH})_2$). Similarly to the pre-edge regions of the XAS spectra, the valence to core areas decrease from 39.60 for the $(\mu\text{-O})_2$ bridge, to 37.79 and 33.63 for the (μ-O)(μ-OH) and $(\mu\text{-OH})_2$ bridges, respectively. Thus, the valence to core areas are expected to be more useful for determining protonation states of the bridging oxygen atoms than the valence to core energies.

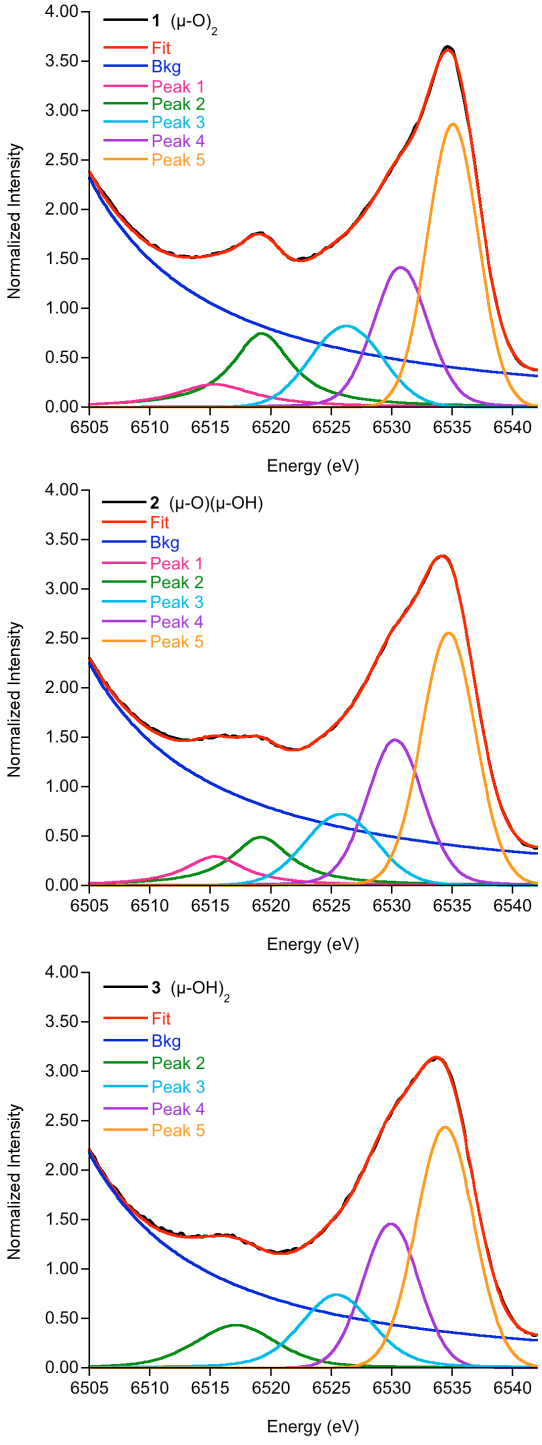

Figure 4.10. Fits to the XES valence to core region for compounds **1** (top), **2** (middle) and **3** (bottom).

Changes in the satellite region. It is interesting to inspect the changes in the satellite region upon protonation. For the $(\mu\text{-O})_2$ bridged complex a single, albeit non-symmetric, intense feature is observed at 6519.3 eV (Table 4.2). A lower energy fit component was needed to accurately fit the asymmetry of this feature (Figure 4.10, top). Similarly for the $(\mu\text{-OH})_2$ bridged complex, a single feature is observed, although here the feature is more symmetric, less intense, and is shifted 2.2 eV to lower energy at 6517.1 eV. For the $(\mu\text{-O})(\mu\text{-OH})$ complex, however, two even less intense Kβ" features are observed at 6519.2 and 6516.2 eV. The satellite region in systems similar to the ones studied here is known to be due to transitions from atoms bound to the metal center. Considering the different chemical surroundings of the oxygen atoms in the salpn ligand and the bridges, it is likely that these lead to transitions at different energies. Thus, the two fit components in the spectrum of compound **1** can be identified with the two types of oxygen atoms. For compound **2**, two types of oxygen atoms can be distinguished as well, but for compound **3** this is not possible. This analysis does not include an assignment of the transitions from the N-salpn orbitals, but these are expected to remain the same for all species.

Table 4.2. Intensity weighted average energies and areas (x1000) for the normalized total valence to core regions and individual peaks (1-5) for the experimental spectra and calculated spectra based on the high spin solution. Calculated spectra IWAEs were shifted by 59.2 eV to higher energy.

	Total		1		2		3		4		5	
	IWAE (eV)	Area	IWAE (eV)	Area	IWAE (eV)	Area	IWAE (eV)	Area	IWAE (eV)	Area	IWAE (eV)	Area
						Experiment						
1	6531.1	39.60	6515.4	2.90	6519.3	6.93	6526.3	6.13	6530.8	8.65	6535.1	14.99
2	6531.4	37.79	6516.2	3.20	6519.2	4.64	6525.8	6.01	6530.3	9.27	6534.7	14.67
3	6533.2	33.63	--	--	6517.1	4.28	6525.5	6.30	6529.9	8.47	6534.4	14.57
						Calculation						
1	6530.8	19.13	6517.2	0.68	6520.4	3.13	6525.3	0.29	6529.5	2.61	6534.6	12.42
2	6530.6	19.76	6517.7	2.06	6520.7	1.61	6525.1	0.22	6529.7	3.89	6534.5	11.98
3a	6531.0	18.70	6518.5	2.72	--	--	6526.3	0.58	6530.5	5.19	6534.9	10.21
3b	6530.7	18.20	6519.2	3.13	--	--	6526.0	0.58	6530.3	4.68	6534.8	9.90

Calculated XES

The calculated valence to core XES spectra are shown in Figure 4.11, with the experimental background subtracted spectra in Figure 4.12 for comparison. The general trend in the $K\beta_{2,5}$ region (6525-6540 eV) is reasonably well-reproduced with the intensity of the feature at ~6535 eV decreasing upon protonation and a new shoulder appearing at ~6530 eV. Similarly in the satellite region (6515-6525 eV), the intensity decreases upon protonation and the energy of the maximum also decreases (Figure 4.11 and Table 4.2). The intensity of the calculated satellite feature decreases upon protonation, but more importantly, the absolute width of the signal increases (also observed in the experimental spectra). The predicted Kβ" feature of compound **1** at 6520.4 eV is located at the highest energy and has the narrowest peak width in this series. The doubly protonated compound **3a** is also predicted to have a narrow satellite feature, but one that occurs at lower energies (~6518.5 eV). The calculated satellite feature of compound **2** extends from the lower-energy end of compound **3a** to nearly the higher-energy end of compound **1**. For compound **3b**, the width is the same as for compound **2**, but the peak is less intense. Finer details on the asymmetry of the features can be observed in Figure 4.11.

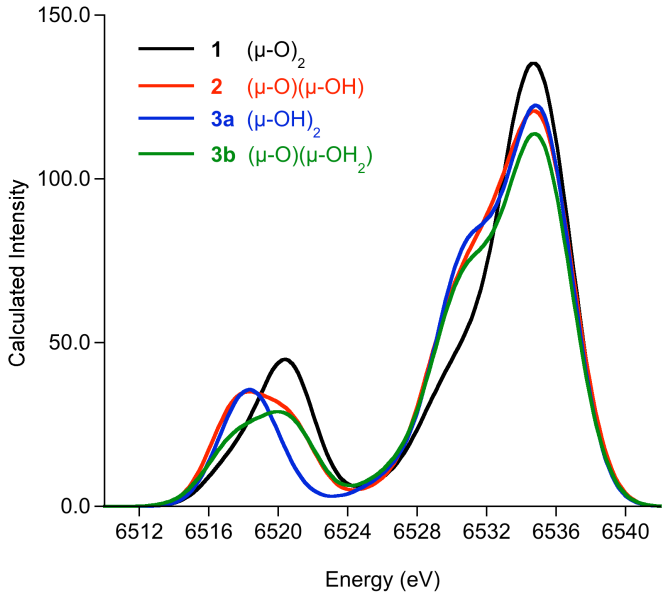

Figure 4.11. Computed x-ray emission valence to core region for compounds **1** (black), **2** (red) and **3a** (blue) and **3b** (green). An artificial broadening of 3.5 eV was applied to the calculated spectra.

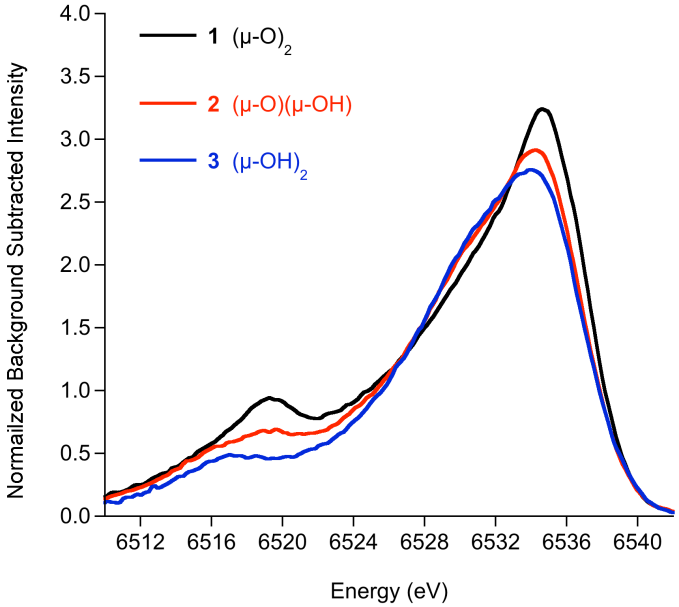

Figure 4.12. Background-subtracted x-ray emission valence to core region for compounds **1** (black), **2** (red) and **3** (blue).

Assignments of the valence to core XES. The assignments of the calculated valence to core spectra are shown in Figure 4.13. The satellite feature is due to transitions from the O and N 2s orbitals into the Mn 1s orbitals. For structure **1**, the transitions appear from lower to higher energy in the order O_{salpn}, N_{salpn}, O_{bridge}, where the transitions from the O_{bridge} 2s orbitals are the most intense. Upon single protonation to compound **2**, the transitions from the now distinguishable bridging oxygen atoms separate. The states occurring at the lowest energy in the satellite feature are due to transitions from orbitals of mixed O_{salpn}/OH_{bridge} character. The transitions from the N_{salpn} 2s and O_{bridge} 2s orbitals are unshifted with respect to the unprotonated species. For the doubly protonated complexes, the N_{salpn} 2s orbitals remain at the same energy as the unprotonated compound **1**. However for structure **3a**, there are no molecular orbitals of mixed O_{salpn}/OH_{bridge} as before for compound **2**. The states arising from the OH_{bridge} 2s orbitals appear at higher energies than the states corresponding to the O_{salpn} 2s orbitals. Since the protonated and unprotonated oxo-bridge 2s orbitals give rise to states at distinctly different energies, the asymmetrically protonated complexes must have satellite regions that extend over a broader energy range. This is seen more clearly when analyzing the satellite region in the spectrum of the hypothetical compound **3b**: the states corresponding to the 2s orbitals of the O_{salpn} and N_{salpn} atoms appear at the same energies as in the other spectra, with the transitions from the oxo-bridge 2s orbital at higher energies, and the transitions from the aquo-bridge O 2s orbital at lower energies. In the convolution, this renders a spectrum that is broader and less intense than for the other structures.

A similar trend was observed in the experimental spectra and their fits: two peaks are necessary to fit the spectra of the unprotonated compound **1** and the singly protonated compound **2**, whereas only one feature is required to fit the spectrum of the doubly protonated compound **3**. According to the calculations for compound **1**, the transitions from unprotonated oxo-bridge 2s

orbitals and the salpn ligand O 2s orbitals appear at energies separated by ~3 eV. Thus, the satellite region extends over an energy range close to the experimental resolution, which explains the demand for two fit peaks in this region for compound **1**. For the doubly protonated compound **3**, however, the different O-contributions are separated by only ~1 eV, which is below the experimental resolution and thus only one peak is needed in the fit of the satellite region.

Besides a decrease in intensity upon protonation, the $K\beta_{2,5}$ feature of the three spectra exhibits no major differences. More interesting is its shoulder at lower energy, which grows strongly upon protonation. In compound **1**, this shoulder is due to transitions of LMCT character from the salpn ligand. The increase in intensity upon protonation stems from transitions out of OH_{bridge} p-orbitals that are found in this energy region together, and sometimes mixed, with the transitions of LMCT character (Figure 4.13).

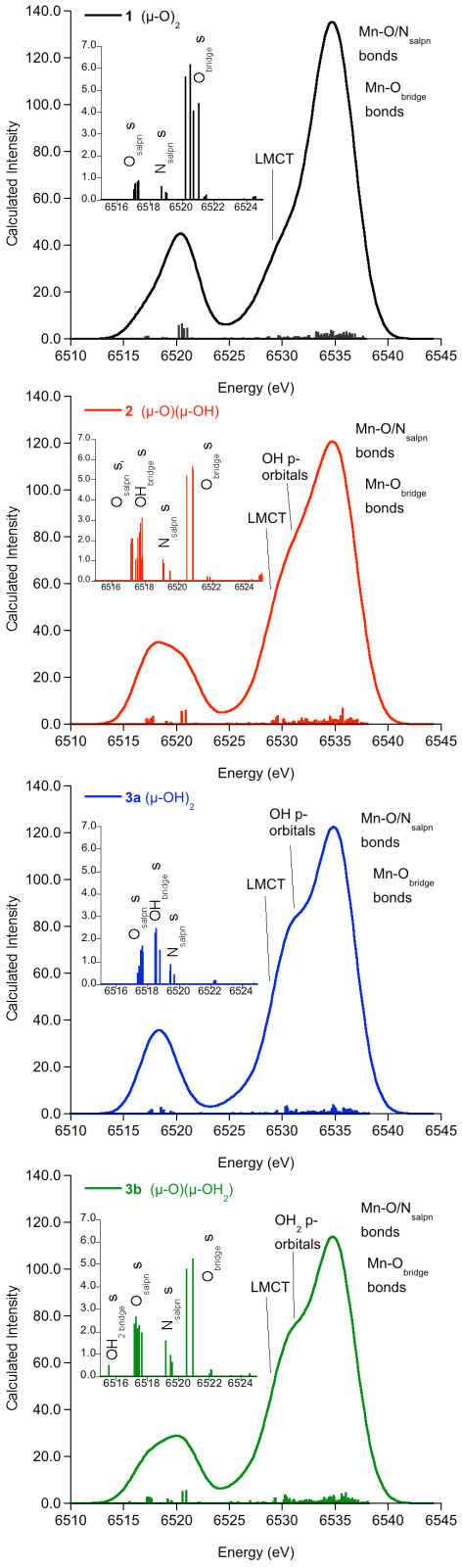

Figure 4.13. Assignments of the calculated XES valence to core region based on the orbital character corresponding to the individual transitions. The insets show the assignments for the satellite regions of the spectra (6515-6525 eV).

Correlation of experimental and calculated XAS intensities and energies

The experimental and calculated areas and the IWAEs are compared for the dimers in the series. In order to better judge the correlation between experiment and theory, previously reported data on a series of Mn monomers,[29] as well as additional data on Mn(V)-monomers ([Mn(V)(O)DCB]$^-$ and [Mn(V)(O)DMB]$^-$)[36] are included in the plots.

The regression line in the correlation of the areas of the total pre-edge region (Figure 4.14) is based on the monomer data only, and it is forced through the origin. The data points of compounds **1**, **2** and **3a** are in reasonable proximity to the monomer line, with structure **3b** showing the largest deviation from the regression line. The regression line follows y = 0.095 x with an adjusted R-value of 0.989, which remains essentially unchanged at 0.988 upon inclusion of the total area dimer data for compounds **1**, **2** and **3a**. Thus it is safe to conclude that the monomer data is a strong calibration set and the dimer data are well predicted by the calculations. Hence the asymmetrically double protonated (μ-O)(μ-OH_2) species, structure **3b**, can be ruled out as a bridging motif. This is an important finding when considering different protonation patterns for the OEC, where the assignment of protonation patterns is far more complex. Such assignment would be aided by the investigation of a larger series of model complexes, with varied Mn oxidation states and donor sets.

The correlation for the IWAEs of the total pre-edge region is shown in Figure 4.15. The regression line follows y = 0.940 x + 394.361 with an adjusted R-value of 0.926, which changes only slightly to 0.929 upon inclusion of the total IWAE dimer data for compounds **1**, **2** and **3a**. The average energies are located at higher values than most of the monomers since their oxidation state is +IV, and not +II or +III as for the monomers.

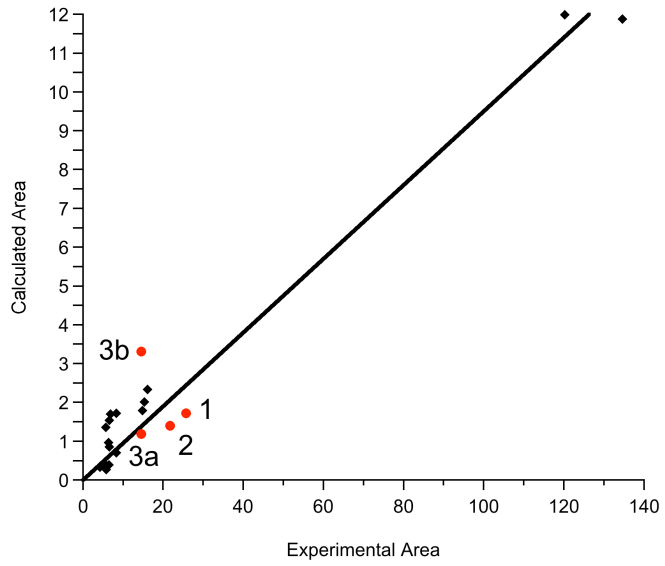

Figure 4.14. Correlation of experimentally determined and calculated XAS areas for the total pre-edge region for the high spin solution of the dimers (red circles) and for the total pre-edge region for the monomer data (black diamonds). The regression line is based on the monomer data only and follows y = 0.095 x (adjusted R = 0.989, forced through 0).

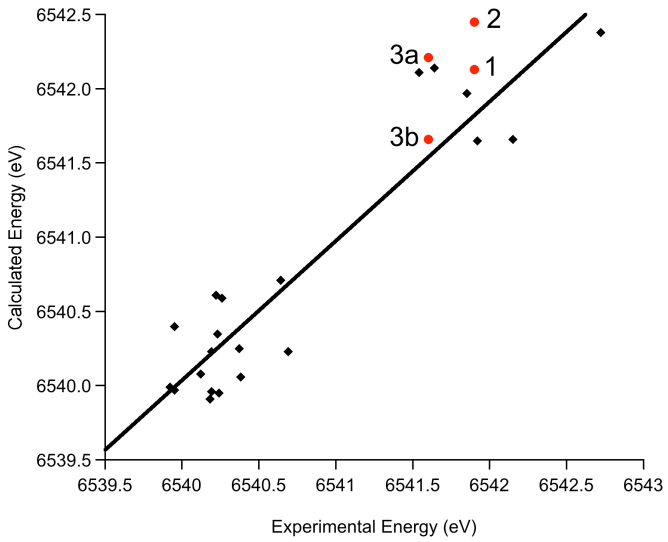

Figure 4.15. Correlation of experimentally determined and calculated XAS IWAEs for the total pre-edge region for the high spin solution of the dimers (red circles) and for the individual peaks of the monomer data (black diamonds). The regression line is based on the monomer data only and follows y = 0.940 x + 394.361 (adjusted R = 0.926).

Correlation of experimental and calculated XES intensities and energies

The x-ray emission spectra are compared to a previously published set of monomer data that includes Mn(II) as well as Mn(III) and Mn(IV) data.[33] The IWAEs for individual peaks of the protonation series are compared to the IWAEs for the total valence to core area of the monomer series. The data points corresponding to the individual peaks of the monomer series fall on the linear regression line for the dimer data (Figure 4.16). As can be expected from this result, the values for the total IWAEs of the dimer XES spectra are close to the regression line. R does not change upon the inclusion of the monomer data so the data are consistent with the previous correlation (R = 0.992 without, R = 0.991 with). Similar observations hold for the areas, where the monomer areas also lie very close to the dimer regression line (Figure 4.17). The best regression line is obtained with both individual and total peak areas for the protonation series, with only a slight change in fit quality upon inclusion of the monomer data (R 0.973 without, 0.979 with). With the emission data alone, it is difficult to rule out a bridging motif based solely on the IWAE and area values.

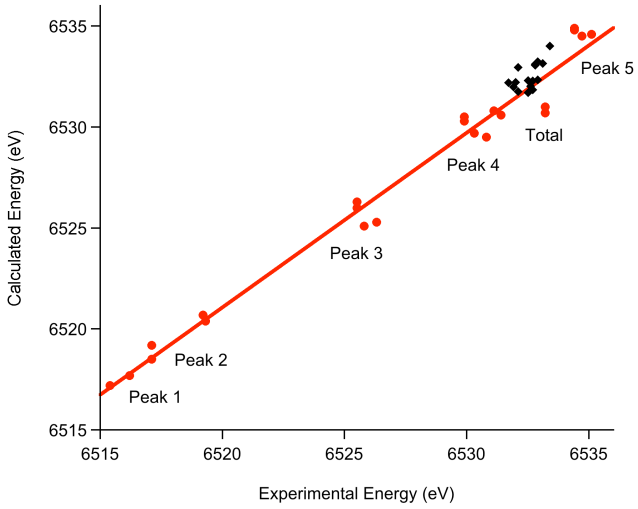

Figure 4.16. Correlation of experimentally determined and calculated XES IWAEs for the individual peaks and the total valence to core regions of the dimers (red circles), and the total valence to core regions of the monomer data (black diamonds). The regression line applies to the dimer data only and follows y = 0.874 x + 821.535 with R = 0.992.

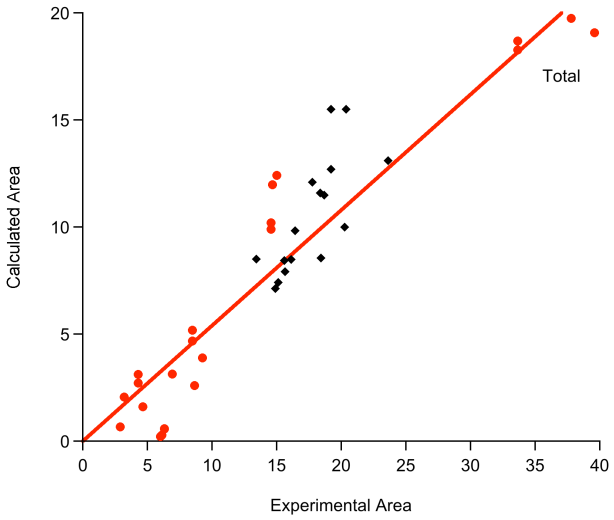

Figure 4.17. Correlation of experimentally determined and calculated XES areas for the individual peaks and the total valence to core region of the dimers (red circles), and the total valence to core region of the monomer data (black diamonds). The regression line applies to the dimer data only and follows y = 0.536 x with R = 0.973.

Conclusions

The analysis of experimental and calculated x-ray absorption and emission spectra of a series of Mn dimers has been conducted in detail. The correlations of experiment and calculation are based on the areas in the pre-edge or valence to core region, and on the respective intensity weighted average energies. In combination with the visual inspection of experimental and calculated spectra, this approach allows the protonation patterns across the series to be distinguished.

For both the XAS and XES spectra, the calculations reproduce the experimentally observed trends reasonably well. The calculated XAS spectra based on the high spin solution both have two features in the pre-edge region (corresponding to transitions of 1s-α and 1s-β electrons into the unoccupied orbitals of local e_g character), and the decrease in both the pre-edge energy and intensity upon successive protonation of the $(\mu\text{-O})_2$ bridges follows that seen experimentally. The calculated XES spectra also successfully reproduce the general shapes of the experimental spectra, most notably in the growth of a shoulder in the $K\beta_{2,5}$ region due to hydroxo 2p

contributions upon protonation of the bridges. Specifically in the satellite region of the spectra, corresponding to transitions from oxo-bridge 2s orbitals, the differences in the protonation states of the bridges are reflected in the number of features observed, as well as in their energies and intensities: there is a single feature for the both the unprotonated and doubly protonated complexes, while there are two distinguishable but less intense features for the singly protonated complex.

It should be noted that the experimental emission spectra are at relatively low resolution (~3.5 eV). In principle, however, measurements could be made at higher resolution (approaching the core hole lifetime of a Mn 1s electron, which is ~1 eV). Such high resolution data would provide a means to potentially glean even more information about subtle structural changes around the Mn atoms. Despite the low resolution, however, the ability of experimental XES to distinguish between the protonation states of the bridges in the dimers presented here illustrates the potential of this technique to discern the protonation states of the oxo bridges in the OEC. This potential is illuminated further by the ability of the XAS and XES calculations to reproduce the subtle differences between the two doubly protonated structures, the symmetric $[Mn_2(IV)(\mu\text{-}OH)_2(salpn)_2]^{2+}$ and the asymmetric $[Mn_2(IV)(\mu\text{-}O)(\mu\text{-}OH_2)(salpn)_2]^{2+}$.

References

1. Bollinger, J. M.; Jiang, W.; Green, M. T.; Krebs, C., *Curr. Opin. Struct. Biol.* **2008,** *18*, 650.
2. Kryatov, S. V.; Rybak-Akimova, E. V.; Schindler, S., *Chem. Rev.* **2005,** *105*, 2175.
3. Lieberman, R. L.; Rosenzweig, A. C., *Critical Reviews in Biochemistry and Molecular Biology* **2004,** *39*, 147.
4. Umena, Y.; Kawakami, K.; Shen, J. R.; Kamiya, N., *Nature* **2011,** *473*, 55.
5. Sproviero, E. M.; McEvoy, J. P.; Gascon, J. A.; Brudvig, G. W.; Batista, V. S., *Photosynth. Res.* **2008,** *97*, 91.
6. Siegbahn, P. E. M., *Acc. Chem. Res.* **2009,** *42*, 1871.
7. Yano, J.; Kern, J.; Irrgang, K. D.; Latimer, M. J.; Bergmann, U.; Glatzel, P.; Pushkar, Y.; Biesiadka, J.; Loll, B.; Sauer, K.; Messinger, J.; Zouni, A.; Yachandra, V. K., *Proc. Natl. Acad. Sci. U. S. A.* **2005,** *102*, 12047.
8. MacMurdo, V. L.; Zheng, H.; Que, L., *Inorg. Chem.* **2000,** *39*, 2254.
9. Milikisiyants, S.; Chatterjee, R.; Lakshmi, K. V., *J. Phys. Chem. B* **2011,** *115*, 12220.
10. Baldwin, M. J.; Stemmler, T. L.; Riggsgelasco, P. J.; Kirk, M. L.; Pennerhahn, J. E.; Pecoraro, V. L., *J. Am. Chem. Soc.* **1994,** *116*, 11349.
11. Larson, E.; Lah, M. S.; Li, X. H.; Bonadies, J. A.; Pecoraro, V. L., *Inorg. Chem.* **1992,** *31*, 373.
12. Gohdes, J. W.; Armstrong, W. H., *Inorg. Chem.* **1992,** *31*, 368.
13. Frasch, W. D.; Mei, R., *Biochim. Biophys. Acta* **1987,** *891*, 8.
14. Glatzel, P.; Bergmann, U., *Coord. Chem. Rev.* **2005,** *249*, 65.
15. Delgado-Jaime, M. U.; Kennepohl, P., *J. Synchrot. Radiat.* **2010,** *17*, 119.
16. Delgado-Jaime, M. U.; Mewis, C. P.; Kennepohl, P., *J. Synchrot. Radiat.* **2010,** *17*, 132.
17. Lenthe, E. v.; Baerends, E. J.; Snijders, J. G., *J. Chem. Phys.* **1993,** *99*, 4597.
18. van Wüllen, C., *J. Chem. Phys.* **1998,** *109*, 392.
19. Klamt, A.; Schüürmann, G., *J. Chem. Soc. Perk. T. 2* **1993**, 799.
20. Baffert, C.; Orio, M.; Pantazis, D. A.; Duboc, C.; Blackman, A. G.; Blondin, G.; Neese, F.; Deronzier, A.; Collomb, M. N., *Inorg. Chem.* **2009,** *48*, 10281.
21. Orio, M.; Pantazis, D. A.; Petrenko, T.; Neese, F., *Inorg. Chem.* **2009,** *48*, 7251.
22. Grimme, S., *J. Comput. Chem.* **2006,** *27*, 1787.
23. Grimme, S., *J. Comput. Chem.* **2004,** *25*, 1463.
24. Grimme, S.; Antony, J.; Ehrlich, S.; Krieg, H., *J. Chem. Phys.* **2010,** *132*.
25. Becke, A. D., *Am. Phys. Soc.* **1988,** *38*, 3098.
26. Perdew, J. P., *Phys. Rev. B* **1986,** *33*, 8822.
27. Pantazis, D. A.; Chen, X. Y.; Landis, C. R.; Neese, F., *J. Chem. Theory Comput.* **2008,** *4*, 908.
28. Weigend, F.; Ahlrichs, R., *Phys. Chem. Chem. Phys.* **2005,** *7*, 3297.
29. Roemelt, M.; Beckwith, M. A.; Duboc, C.; Collomb, M. N.; Neese, F.; DeBeer, S., *Inorg. Chem.* **2012,** *51*, 680.
30. Staroverov, V. N.; Scuseria, G. E.; Tao, J.; Perdew, J. P., *J. Chem. Phys.* **2003,** *119*, 12129.
31. Neese, F.; Wennmohs, F.; Hansen, A.; Becker, U., *Chem. Phys.* **2009,** *356*, 98.
32. Lee, N.; Petrenko, T.; Bergmann, U.; Neese, F.; DeBeer, S., *J. Am. Chem. Soc.* **2010,** *132*, 9715.

33. Beckwith, M. A.; Roemelt, M.; Collomb, M. N.; DuBoc, C.; Weng, T.-C.; Bergmann, U.; Glatzel, P.; Neese, F.; DeBeer, S., *Inorg. Chem.* **2011,** *50*, 8397.
34. Westre, T. E.; Kennepohl, P.; DeWitt, J. G.; Hedman, B.; Hodgson, K. O.; Solomon, E. I., *J. Am. Chem. Soc.* **1997,** *119*, 6297.
35. Armstrong, W. H.; Lippard, S. J., *J. Am. Chem. Soc.* **1984,** *106*, 4632.
36. Yano, J.; Robblee, J.; Pushkar, Y.; Marcus, M. A.; Bendix, J.; Workman, J. M.; Collins, T. J.; Solomon, E. I.; DeBeer George, S.; Yachandra, V. K., *J. Am. Chem. Soc.* **2007,** *129*, 12989.

CHAPTER FIVE

How accurately can Extended X-ray Absorption Spectra be Predicted from First Principles? Implications for Modeling the Oxygen Evolving Complex in Photosystem II.[4]

Introduction

X-ray absorption spectroscopy (XAS) is a powerful tool for determining the geometric and electronic structure of a transition metal absorber. The extended x-ray absorption fine structure (EXAFS) region of the spectrum has had a particularly profound impact on our understanding of the local metrical structure of the transition metal active sites in numerous metalloproteins. In many cases, EXAFS data has preceded the crystallographic characterization of proteins by years or even decades.[1] EXAFS data have also been utilized extensively to provide unique structural insights into enzymatic intermediates. Examples include characterization of the oxygen intermediates in methane monooxygenase,[2, 3] ribonucleotide reductases,[4] P450s,[5] chloroperoxidases,[6] and multicopper oxidases[7] to name only a few. In the context of the present manuscript, the current view of the Mn_4Ca cluster in photosystem II has been greatly influenced by the results of detailed extended x-ray absorption fine structure (EXAFS) studies. Most notably, more than three decades ago, Mn K-edge EXAFS studies first established the presence of a 2.7 Å Mn-Mn vector in the oxygen evolving complex (OEC) of photosystem II (PSII).[8] In subsequent studies the picture was further refined: a combination of oriented membrane Mn EXAFS,[9] Ca EXAFS,[10, 11] Sr EXAFS,[11-13] range-extended Mn K-edge EXAFS,[14] and single crystal Mn K-edge EXAFS[15] gave rise to an increasingly detailed description of the Mn_4Ca active site. Based on these studies, Yano, Yachandra and coworkers have shown that the

[4] Adapted from Beckwith, M. A.; Ames, W.; Vila, F. D.; Krewald, V.; Duboc, C.; Collomb, M.-N.; Yano, J.; Rehr, J. J.; Neese, F.; and DeBeer S. (to be submitted).

EXAFS of the S_0, S_1, and S_2 states show strong similarities, while the largest changes occur on going to the S_3 state.

The S_2 state is perhaps the best studied, due the presence of a characteristic EPR multiline signal, indicative of an S=1/2 ground state.[16, 17] Based on the EXAFS, the S_2 state active site contains three 2.7-2.8 Å Mn-Mn vectors, one longer ~3.3 Å Mn-Mn vector, and Mn-Ca interactions at 3.4 and 4.0 Å (with either a 2:2 or 3:1 ratio of short to long vectors). In addition, an average of two Mn-O contributions per Mn can be identified at a distance of ~1.85 Å. From this information, one would like to reconstruct the three-dimensional model that gives rise to these scattering contributions. Such an approach has been applied by Yano et al. in a detailed polarized EXAFS study[15] of the S_1-state from which they concluded that neither the cubane like model derived from Barber's initial 3.5 Å crystal structure[18] or the 3.0 Å crystal structure of Loll et. al.[19] were consistent with the EXAFS data. Rather they proposed the possibility of three different topologically related "dimer of dimers" models, which were consistent with the polarized EXAFS data. Interestingly, using the same data, Batista and coworkers proposed a cubane like model and argued that it is consistent with the calculated EXAFS spectra.[20, 21]

S_2 state models have also been proposed on the basis of detailed computational studies. Siegbahn and coworkers[22, 23] have proposed a model which is similar to the "dimer of dimers" models proposed by Yano et. al., whereas that proposed by Barber and Murray[18] is similar to the cubane like model of Batista and coworkers. In a recent computational study, Pantazis et. al. demonstrated that both a Siegbahn-like open cubane model and the closed-cubane model of Barber are viable S_2 state structures, with an energetic difference of only 1 kcal/mol, suggesting the two conformations could potentially coexist in the S_2 state, and are likely interconvertible depending on the experimental conditions (Scheme 1 A and B).[24]

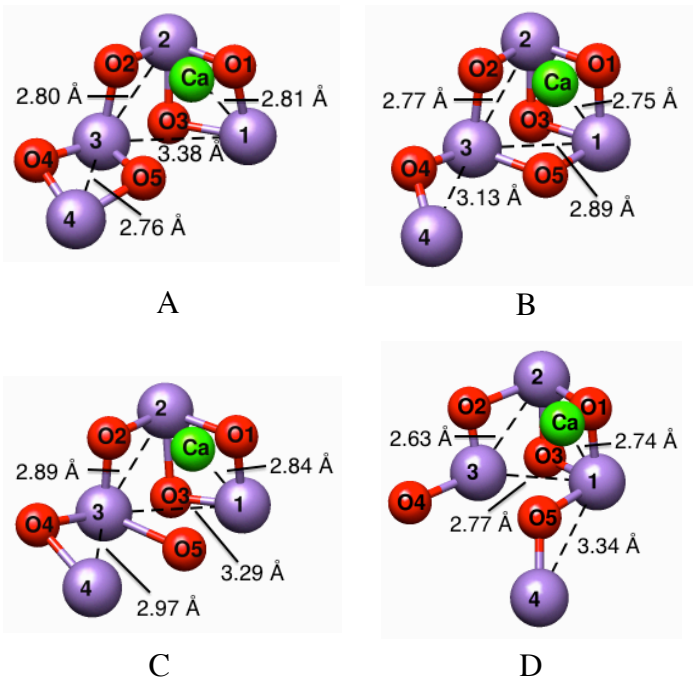

Scheme 5.1. Schematic representations of the Mn_4Ca core of the models of the OEC. Mn-Mn distances are shown for each model. The Mn atoms are labeled according to the numbering scheme in reference 24. The Ca atom is located in a plane coming out of the paper towards the reader.

This raises the possibility that the experimental EXAFS of the S_2 state reflects the presence of the two different conformations. Do the EXAFS data correspond to a closed cubane as initially reflected in the Barber crystal structure and the subsequent calculations of Batista and Murray? Or do the EXAFS data correspond to an open cubane like model, as initially proposed by both Yano and Siegbahn? Can EXAFS data distinguish these two possibilities?

Inherent in this discussion, is the question of how reliably one can predict EXAFS data based on multiple scattering calculations. The predictions of both Yano and Batista utilized FEFF calculated EXAFS data, with either global Debye-Waller (DW) values or experimentally estimated DW values. Yano et al. used fixed DW values for the Mn-Mn and Mn-Ca vectors of PSII models based on previous fitting results from PSII and model compound studies, whereas Batista et al. used a global DW value in the EXAFS calculations. Another approach that has been used by Ryde and co-workers is to use DW values that were calculated from quantum

mechanical vibrational frequencies. This approach was applied to Ni and Cu model complexes and [Ni, Fe] hydrogenase but not to the OEC.[25, 26]

Clearly, if one intends to use the experimental EXAFS data in conjunction with calculations as a means to limit and define a three dimensional structure in a system as complex as the OEC, one must first determine how reliably current state-of-the-art multiple scattering calculations are able to *predict* EXAFS of simple molecules? One should carefully differentiate between the *fitting* and *prediction* of EXAFS spectra. In the *fitting approach* a least square fit of DW factors and geometrical parameters are varied until the best agreement with experiment is achieved. This approach has been used in countless successful studies and, when used properly, provides accurate metal ligand distances. On the other hand, the *prediction* of EXAFS spectra implies that a purely theoretically obtained spectrum is compared to the experimental one. Thus, both the structure of the species under investigation as well as the DW factors need to be obtained on theoretical grounds. Only if it is possible to properly predict the EXAFS spectrum of molecules with known structure and known EXAFS spectra can this approach be used to judge the quality or plausibility of a theoretical obtained structure for an unknown system. To the author's knowledge the ability to use EXAFS in the latter, predictive way for complex molecules has never been rigorously assessed despite its frequent use in application studies. The main purpose of this work is to fill this gap and there assess how the results impact the general understanding of the EXAFS for the OEC.

In order to address these questions, a systematic study of a series of monomeric and dimeric Mn model complexes, for which high accuracy crystal structures are known, has been conducted. FEFF is then used to calculate the EXAFS based on the crystal structure using the Correlated Debye (CD) model, and also to calculate the EXAFS based on the DFT geometry optimized structure, using both the CD model and a more refined model, known as the Dynamical Matrix

(DM) method, which uses harmonic frequencies obtained from DFT second derivatives.[27]

Using this information and comparing fit values to predicted values, the author is able to assess which parameters from the FEFF calculations are most reliable and which require further refinement, either from experiment and/or computations. This approach is then applied to the S_2-state of the OEC, and the predicted EXAFS based on proposed literature models. We focus on the open and closed cubane model of the Mn_4Ca active site, as most recently defined by Pantazis et. al., and which correspond most closely to the models of Siegbahn[22, 23] and Barber, respectively.[18] In addition, a geometry optimized model of the Shen crystal structure[28] and Batista's[20] computational model are investigated (Scheme 1, C and D). The broader implications for using EXAFS data in a predictive fashion are discussed.

Experimental

A set of three mononuclear and four binuclear manganese complexes was investigated (Scheme 5.2). The following abbreviations have been used for the ligands: terpy = 2,2':6',2"-terpyridine; phenylterpy = 4'-phenyl-2,2':6',2"-terpyridine; tpa = tris-2-picolylamine.

Sample Preparation. The samples were synthesized by the groups of Drs. Carole Duboc and Marie-Noëlle Collomb according to published procedures.[29-34] All XAS samples were prepared as dilutions in boron nitride, pressed in Al spacers and sealed with 38 micron Kapton windows. All samples were measured at 10 K in a liquid Helium cryostat.

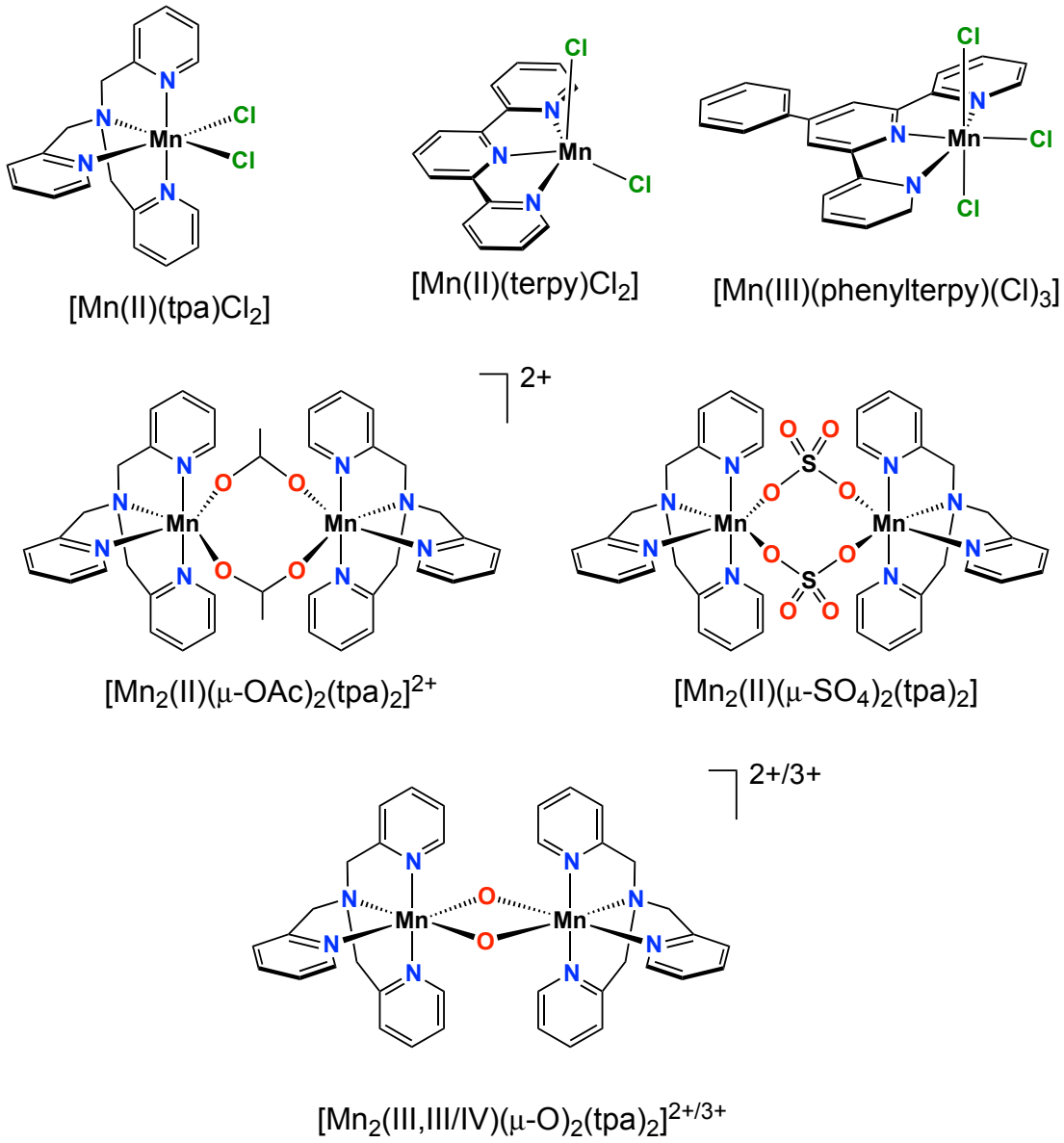

Scheme 5.2. The seven manganese complexes investigated in this study.

XAS Data Collection. All XAS data were recorded at the Stanford Synchrotron Radiation Laboratory (SSRL) on focused beam line 9-3. A Si(220) monochromator was used for energy selection. A Rh-coated mirror (set to a cutoff of 10 keV) was used for harmonic rejection, in combination with 25% detuning of the monochromator. All data were measured in transmission mode to k = 12 Å^{-1}, stopping at the Fe K-edge. Internal energy calibration was performed by simultaneous measurement of the absorption of a Mn foil placed between a second and third

ionization chamber. The first inflection point of the Mn foil was assigned to 6539.0 eV. Samples were monitored for photoreduction throughout the course of data collection. Only those scans that showed no evidence of photoreduction were used in the final averages. The averaged data were processed as described previously.[35] A second-order polynomial was fit to the pre-edge region and subtracted from the entire spectrum. A three-region cubic spline was used to model the background above the edge using the program PySpline.[36]

EXAFS Calculations. Theoretical EXAFS spectra were calculated using both FEFF 7 and FEFF 9.[37, 38] The EXAFS amplitude, $\chi(k)$, is given by[27]

$$\chi(k) = S_0^2 \sum_R N \frac{\left|f_{eff}(k)\right|}{kR^2} \sin(2kR + \phi_k) e^{-2kR/\lambda_k} e^{-2\sigma^2 k^2} \tag{5.1}$$

where S_0^2 is the overall many-body amplitude factor, N is the number of similar scatterers, $|f_{\text{eff}}(k)|$ is the effective scattering amplitude, R is the absorber-scatterer distance, $\exp(-2\sigma^2 k^2)$ is a Debye-Waller like factor, λ_k is the mean free path of the photoelectron, and ϕ_k is the total phase shift for the photoelectron wave interaction with the absorber and the scatterer. All of the scattering paths contributing to the total EXAFS were calculated directly in FEFF using default parameters. The S_0^2 parameter was set to 1 for all calculations and fits except where noted.

Four different approaches were examined for the EXAFS calculations:

Method 1. Spectra were calculated with FEFF 7 using the crystal structure coordinates, and the resulting spectra were fit to the data using EXAFSPAK[39] as described previously.[35]

Method 2. Spectra were calculated with FEFF 9 using crystal structure coordinates and the CD model.

Method 3. Spectra were calculated with FEFF 9 using DFT geometry optimized structure coordinates and the CD model.

Method 4. Spectra were calculated with FEFF 9 using DFT geometry optimized structure coordinates and the DM model. Hessians were obtained from DFT frequency calculations, using the ORCA program[40], as described below. In principle spectra can also be calculated using the DM model and the crystal structure coordinates. Results for a limited test set are presented in Figures 5.4 and 5.5, and show generally similar trends. However, in some cases significant imaginary frequencies resulted, thus we have chosen to focus only on the DM model used in conjunction with the geometry optimized structures.

The differences between the two models used for calculating DW factors in methods 3 and 4 are largely a result of the differences in how the vibrational density of states (VDOS) is calculated. On the most sophisticated level (Method 4), the VDOS is calculated on the basis of the calculated quantum chemical frequencies. The main points of the theory are described in ref 27. To this end the VDOS can be written in terms of the spectral resolution of the (mass weighted) Hessian matrix (usually called the 'dynamic matrix' in the physics literature). In operator form, the VDOS operator takes the form:

$$\hat{\rho}(\omega) = -\frac{2\omega}{\pi} \sum_{k=1}^{3N_{At}-6(5)} \frac{\left|\mathbf{k}\right\rangle\left\langle\mathbf{k}\right|}{\omega^2 - d_k - i\varepsilon} \tag{5.2}$$

Here N_{At} is the number of atoms and hence $3N_{At}-6(5)$ represents the number of vibrational degrees of freedom (5) for linear molecules), ω is the frequency, $\left|\mathbf{k}\right\rangle$ an eigenvector of the mass weighted Hessian matrix and d_k is its k'th eigenvalue (related to the harmonic frequency of the associated mode by $\omega_k = 1302.78\sqrt{d_k}$, in cm^{-1}). As usual, ε is a broadening parameter. The mass-weighted Hessian matrix is:

$$D_{KL} = \frac{1}{\sqrt{M_K M_L}} \frac{\partial^2 E}{\partial X_K \partial X_L} \tag{5.3}$$

Here X_K and X_L denote nuclear displacements and M_K and M_L are the masses of the atoms that belong to the given pair of displacements. Each scattering pathway $\mathbf{R}$ in a multiple scattering calculation consists of a number of atoms that build up the pathway. Let us denote the atoms and their associated displacements involved in a scattering pathway with $\left|\mathbf{Q}_R\right\rangle$ (this is a vector of length $3N_{At} - 6(5)$ that contains zero's for all atoms not involved in the pathway). One can then readily obtain a VDOS that is projected onto the given pathway as $\rho_R(\omega) = \mathrm{Im}\left\langle \mathbf{Q}_R \mid \hat{\rho}(\omega) \mid \mathbf{Q}_R \right\rangle$. This quantity essentially indicates how strongly a given scattering pathway contributes to the VDOS at a given frequency ω. Using this projected quantity and applying the reasoning outlined in the original references, the Debye-Waller factor for a given pathway as a function of temperature is obtained by integrating over frequency to obtain:

$$\sigma_R^2(T) = \frac{\hbar}{2\mu_R}\int_0^\infty \frac{1}{\omega}\coth\left(\frac{\hbar\omega}{2k_BT}\right)\rho_R(\omega)\,d\omega \tag{5.4}$$

where μ_R is the reduced mass associated with the given scattering pathway $\mathbf{R}$ and k_B is Boltzmann's constant.

In the CD model a much simpler approach is taken.[41] Here the projected VDOS is calculated as:

$$\rho_R(\omega) = \frac{3\omega^2}{w_D^3}\left[1 - \frac{\sin(\omega R/c)}{\omega R/c}\right] \tag{5.5}$$

where R is the absorber-scatterer path distance, $w_D = k_B\theta_D/\hbar$ is the Debye frequency, θ_D is the Debye temperature, c = w_D / k_D denotes the Debye approximation to the speed of sound, k_D = $(6\pi^2 N/V)^{1/3}$, and N/V is the atomic density number in the crystal.

Electronic structure Calculations. All quantum chemical calculations were carried out with the ORCA quantum chemistry package.[40] The molecular geometries of the Mn monomers were

optimized by Michael Roemelt as described previously[42] using the BP86 functional[43, 44] and scalar relativistically recontracted (SARC)[45] all electron def2-TZVP(-f) basis sets.[46] The Coulomb fitting basis of Weigend was used in the uncontracted form. The conductor like screening model[47] (COSMO) was used with dichloromethane as the solvent ($\varepsilon = 9.08$). Scalar relativistic effects were taken into account at the ZORA level,[48, 49] and all species were treated with the spin-unrestricted Kohn-Sham method. Dense integration grids were used for all calculations (ORCA Grid4).

The molecular geometries of the Mn dimers were optimized by Vera Krewald using the BP86 functional[43, 44] and scalar relativistically recontracted (SARC) all electron def2-TZVP basis sets. As with the monomers, the calculations used ZORA. Solvation effects were accounted for with the conductor-like screening model (COSMO, $\varepsilon = 8$) to simulate a protein environment for comparison with OEC data, and the empirical van der Waals correction[50-52] to the DFT energy was also included.

Calculations were investigated for the four proposed models shown in Scheme 1. Models A and B are based on the recently reported open-cubane and closed cubane conformations, as proposed by Pantazis et al.[24] Model C is a DFT refined model of the 1.9 Å XRD.[28] Model D is the open cubane model of Batista.[20] Geometry optimizations performed by Vera Krewald used the BP86 functional[43, 44] and all-electron relativistic contracted basis sets[45] (TZVP on Mn, O, and N, and SARC-SVP on C and H). The zeroth-order regular approximation (ZORA)[48, 49] was used to account for relativistic effects. Solvation effects were accounted for by the conductor-like screening model (COSMO, $\varepsilon = 8$) and the third-generation (D3) van der Waals correction of Grimme[52] was used as well.

The same protocols used for the geometry optimizations were used for the numerical frequency calculations. Inclusion of COSMO in the frequency calculations did not significantly affect the theoretical EXAFS spectra in the subsequent FEFF calculations.

Results and Discussion

Fits to the Mn Monomers EXAFS Data: Method 1. Figure 5.1 shows the experimental data and the fits to the data for the Mn monomers. The best fit parameters are given in Tables 5.1-5.3. The fits were obtained by first calculating the $\chi(k)$ spectra using FEFF 7 and then allowing the distances, σ^2 values, and ΔE_0 to refine (method 1). The metrical parameters are summarized in Table 5.4, column 1. These results, perhaps not surprisingly, show excellent agreement with the experimental EXAFS, with error values (F $x10^3$) ranging from 0.19-0.58 over the series of monomers. The obtained distances (Table 5.4) are in reasonable agreement with the crystallographic distances, with first shell Mn-Cl distances deviating by less than 0.02 Å from the crystallographic values. A slightly larger error is seen for the Mn-N distances, with deviations of 0.03-0.06 Å, relative to the crystal structure. A larger error in light atom interactions (i.e. N) is generally expected in the presence of a heavier scatterer (i.e. Cl). As there are numerous paths that contribute to the Mn-C and Mn-C-N paths because of the larger number of C atoms in the terpy ligand (Figure 5.2), a direct comparison with the crystal structure is more difficult to assess for these particular path contributions. However, the Mn-C-N multiple scattering paths do not have a significant contribution to the total EXAFS (FT magnitudes on the order of ~0.06 compared to ~2.0 in the first shell of the experimental FT). In any case, visual inspection of the data and the fit in both EXAFS and FT shows good agreement. This approach to analyzing EXAFS data is, of course, the most common approach used in the literature. It, however, fails to illustrate the difference between the data and first-principles calculations, which

is essential if one wishes to use EXAFS calculations in a predictive fashion. In order to better assess this, the FEFF calculated spectra are presented below.

Table 5.1. Best fit parameters for [Mn(II)terpyCl_2]. Standard deviations for the fit values are given in parentheses.

N	Path	R (Å)	σ^2 ($Å^2$)	ΔE_0 (eV)	F ($x10^3$)
2	Mn-Cl	2.36 (0.0038)	0.0025 (0.0005)	-7.605 (0.6130)	0.579
3	Mn-N	2.21 (0.0098)	0.0044 (0.0012)	-7.605	
6	Mn-C	3.13 (0.0104)	0.0061 (0.0012)	-7.605	
7	Mn-C	4.62 (0.0143)	0.0034 (0.0015)	-7.605	
12	Mn-C-N	3.26 (0.0265)	0.0052 (0.0045)	-7.605	

Table 5.2. Best fit parameters for [Mn(II)tpaCl_2]. Standard deviations for the fit values are given in parentheses.

N	Path	R (Å)	σ^2 ($Å^2$)	ΔE_0 (eV)	F ($x10^3$)
2	Mn-Cl	2.44 (0.0033)	0.0025 (0.0004)	-8.427 (0.4406)	0.511
4	Mn-N	2.27 (0.0082)	0.0067 (0.0010)	-8.427	
4	Mn-C	3.15 (0.0094)	0.0026 (0.0012)	-8.427	
6	Mn-C	4.68 (0.0256)	0.0075 (0.0030)	-8.427	
18	Mn-C-N	3.44 (0.0147)	0.0015 (0.0019)	-8.427	

Table 5.3. Best fit parameters for [Mn(III)phenylterpyCl_3]. Standard deviations for the fit values are given in parentheses.

N	Path	R (Å)	σ^2 ($Å^2$)	ΔE_0 (eV)	F ($x10^3$)
3	Mn-Cl	2.29 (0.0027)	0.0049 (0.0003)	-3.496 (0.3879)	0.190
3	Mn-N	2.13 (0.0066)	0.0062 (0.0010)	-3.496	
6	Mn-C	2.90 (0.0186)	0.0018 (0.0024)	-3.496	
14	Mn-C-N	4.51 (0.0080)	0.0015 (0.0008)	-3.496	
10	Mn-C-N	5.06 (0.0115)	0.0010 (0.0015)	-3.496	

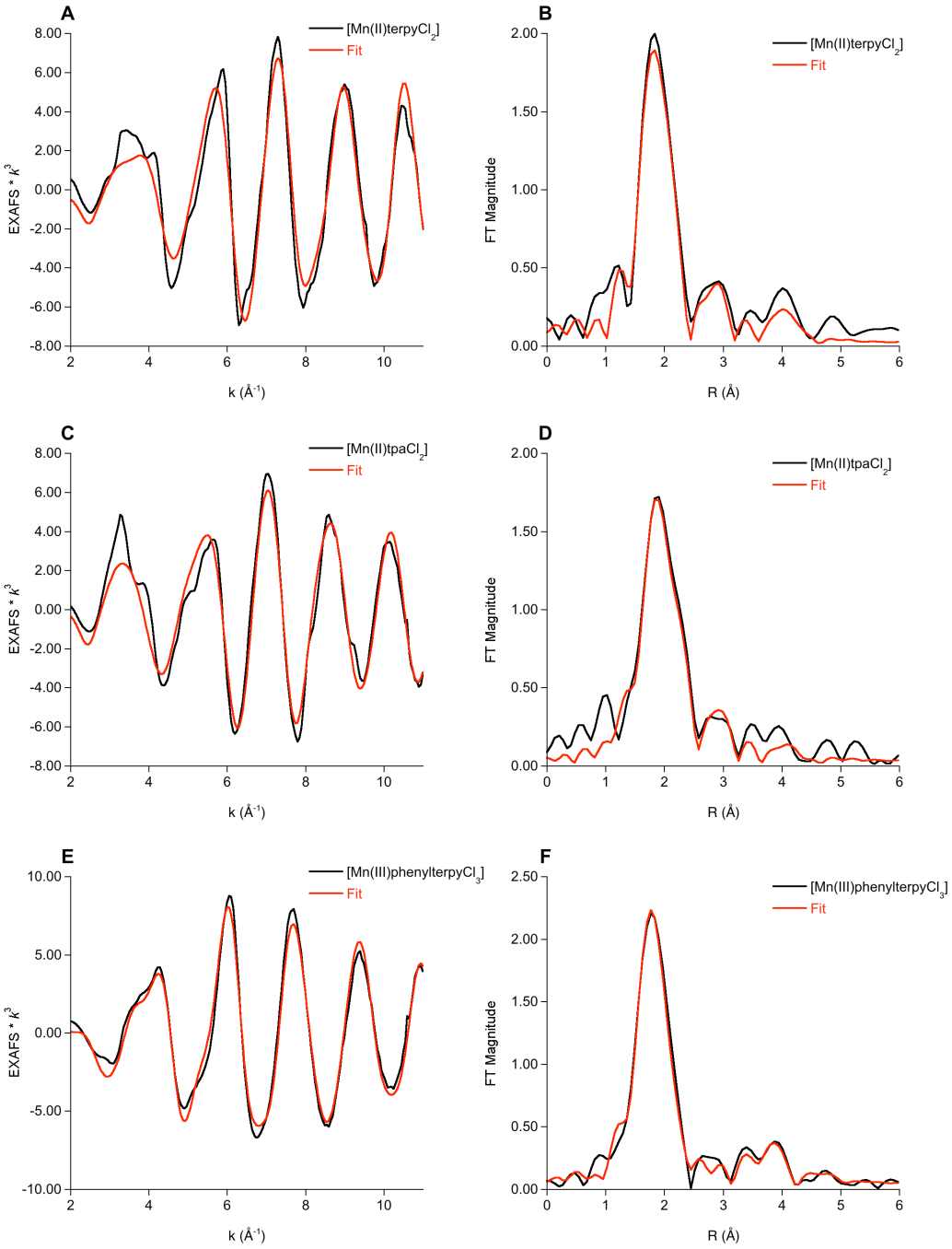

Figure 5.1. Experimental (black) and fits (red) to the $\chi(k)$ spectra and the corresponding non phase shift corrected FTs of [Mn(II)terpyCl_2] (A and B), [Mn(II)tpaCl_2] (C and D), and [Mn(III)phenylterpyCl_3] (E and F).

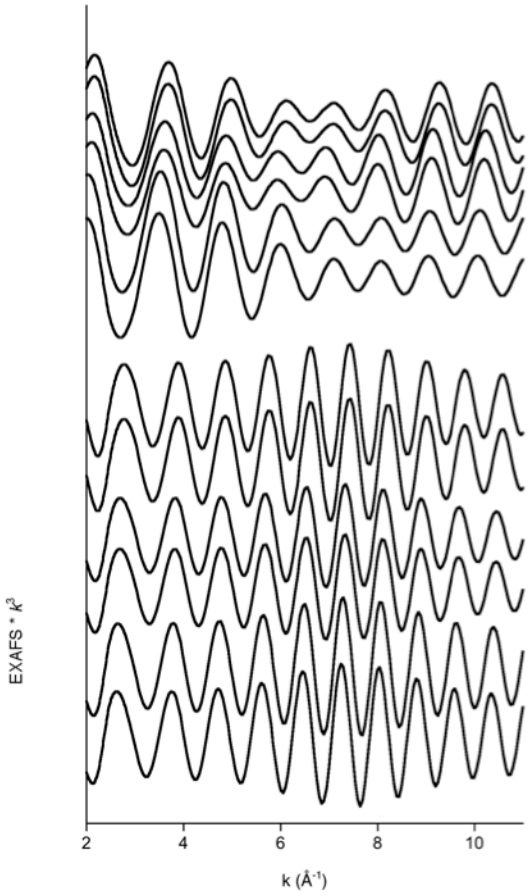

Figure 5.2. $\chi(k)$ spectra of the individual multiple scattering Mn-C-N paths of [Mn(II)terpyCl_2].

FEFF calculated EXAFS Spectra for the Mn Monomers: Methods 2-4.

Figure 5.3 presents the direct FEFF calculated spectra using methods 2-4 *without any fitting of parameters*. These results are summarized in Table 5.4, columns 2-4 and Figure 5.3. While all of the theoretical spectra reproduce the general shape of the experimental spectra reasonably well in the first shell (i.e. at distances, R, between 0 and 2.5 Å), there are clear discrepancies in the calculated intensity and in the distributions and intensity of the outer shell features (R > 2.5 Å) relative to experiment (Figure 5.3). Not surprisingly, without fitting the calculated spectra to the experimental data, one observes a substantial increase in the error values, by a factor of up to ~7 (Table 5.4), which is also observed visually in the calculated spectra (Figure 5.3). Here the origin of these differences in each computational approach is more closely evaluated.

Method 2. It is perhaps most instructive to first compare the method 2 calculated spectra to the fit data, as this approach uses the crystallographic coordinates. Table 5.4 (columns 1 and 2) highlights the differences between the crystal structure and the fit EXAFS data. For all three monomers the error value has increased significantly, with the largest deviation occurring for the complex [Mn(III)phenylterpyCl_3]. As noted above, the first shell Mn-Cl distances are in very good agreement with the EXAFS fit distances. However, larger differences are observed for the more weakly scattering Mn-N distances, as well as the outer shell Mn-C distances. The differences between method 2 and the fit data (method 1) are summarized in Table 5.5, column 1. The difference between the fit and calculated distances and DW values are reported, together with percentage deviations between the calculated and fit values. As an example, the Mn-N distance from the [Mn(II)terpyCl_2] crystal structure, 2.21 Å, is 0.03 Å shorter than the fit distance of 2.24 Å, thus corresponding to a ΔR of ~1% between the calculated and fit distances. Over the series of monomers, the percent deviation in the calculated and fit distances for the first-shell paths ranges from 0-3%. Similar trends are observed for the longer distance single and multiple scattering paths involving atoms that are part of the terpy or tpa ligands (Mn-C and Mn-C-N), though the deviations between the calculated and fit distances span a larger range (ΔR = 0.3-6%). This may be attributed to the larger number of paths which comprise the 2.5-5 Å region of the FT.

While the calculated distance values are reasonably similar to the fit distances, this is not the case for the DW factors. Using method 2, the average calculated DW factors (Table 5.4) differ from the fit DW factors by ~30-67% for the first-shell paths (0 Å < R < 2.5 Å), and by ~6-330% for the outer shell paths (i.e. contributions at R > 2.5 Å). We note that the full range of outer shell paths is not reported in Table 5.5. Table 5.5 reports only the single scattering contributions. Multiple scattering contributions are on average found to have even larger errors in the

calculated vs. fit DW values. In any case, these results clearly indicate that the largest error in the FEFF calculated spectra is associated with determining mean square deviations in the bond lengths.

Method 3. In addition to using the crystallographic coordinates (method 2), the FEFF 9 CD model using DFT geometry optimized structures (method 3) was also tested. The results of these calculations are summarized in Figure 5.3 and Tables 5.4 and 5.5. As can be clearly seen in Table 5.4, the geometry optimized distances are quite similar to the crystallographic distances, with deviations of 0.01-0.02 Å in the first-shell distances and somewhat larger deviations in the outer shell contributions. Overall the root mean square deviations between the crystallographic coordinates and the geometry optimized structures range from 0.247 to 0.922, indicating generally reasonable agreement. As the changes in distances are relatively small, it is perhaps not surprising that there is correspondingly essentially no change in the DW values between methods 2 and 3 (Table 5.4).

The small changes in FT intensities between method 2 and method 3 (see Figures 5.3D and F) reflect the slight differences in bond length distribution rather than differences in the calculated disorder parameters. This is more clearly illustrated by examining the deconvolution of the calculated spectrum of [Mn(II)(tpa)Cl_2] as presented in Figure 5.6. There are noticeable differences in the intensities of the individual components using methods 2 and 3, particularly for the Mn-Cl and Mn-N contributions. This originates from a larger distribution in the Mn-Cl and Mn-N distances in the geometry optimized structure, as compared to the crystal structure. In the crystal structure the Mn-Cl distances are 2.42 Å and 2.45 Å while in the geometry optimized structure the Mn-Cl vectors are 2.39 Å and 2.47 Å. Similarly for the Mn-N distances the experimental vectors of 2.29, 2.29, 2.35 and 2.40 Å show a somewhat larger distribution in the geometry optimized structure, with values of 2.26, 2.27, 2.38, and 2.41 Å, respectively. This

results in a higher calculated total first-shell FT intensity for method 2 than for method 3 (a total FT magnitude of 2.2 vs. 1.8, Figure 5.3D). This further highlights the importance of having both accurate distances and DW values in order to make spectral predictions.

Method 4. As the Correlated Debye model did not produce satisfactory results at either the crystallographic coordinates or at the geometry optimized structures, in large part due to significant error in the DW values, an alternate method for obtaining these values was explored. DFT frequencies were used within the FEFF DMDW code in order to obtain the values for mean bond displacements. These results are summarized in Figure 5.3 and Tables 5.4 and 5.5 (last column).

By inspection of Figure 5.3 and Table 5.4, one can see that in certain cases, method 4 gives slightly better predicted spectra ([Mn(III)phenylterpyCl_3]), while in other cases, it is slightly worse. Specifically, for the geometry optimized structure of [Mn(II)tpaCl_2], the DW value for the Mn-Cl path calculated using the DM method is almost twice that of the DW value calculated using the CD method (Method 3) at the same structure (Table 5.4). This larger DW value results in a decrease in the intensity of the FT for this path (Figure 5.6). As the Mn-Cl path dominates the first shell FT spectral intensity, this results in a total calculated first shell FT intensity that is too low. In general, the DW factors calculated using method 4 differ from the fit values from method 1 by ~12-52% for the first-shell paths, and by ~3-230% for outer shell paths (as with methods 2 and 3, the percent deviations for the multiple scattering paths are not reported in Table 5.5). These differences are lower than those for methods 2 and 3 (first-shell ~30-67%, outer shell ~6-330%), indicating that method 4 results in slightly better calculated DW values than either method 2 or 3. However, given that the direct calculation of the DW factors through quantum chemically calculated frequencies represents much more rigorous physics than the simple CD model (which amounts to a spherical approximation), the result is still somewhat disappointing.

In particular because quantum chemical frequencies from DFT calculations are well known to be quite precise in the overwhelming majority of cases.

For methods 2-4, one could also improve agreement with the experimental data, by refining the amplitude parameter, S_0^2. Specifically for method 2, by allowing S_0^2 to decrease to a value of 0.8, better agreement with experimental data can be obtained. As an example, for [Mn(II)tpaCl_2] the error value decreases from the value reported in Table 5.4 to 1.2e-3. However, as modifying the S_0^2 value uniformly decreases the entire spectral intensity, such an approach is not appropriate when the relative intensities of the contributions vary.

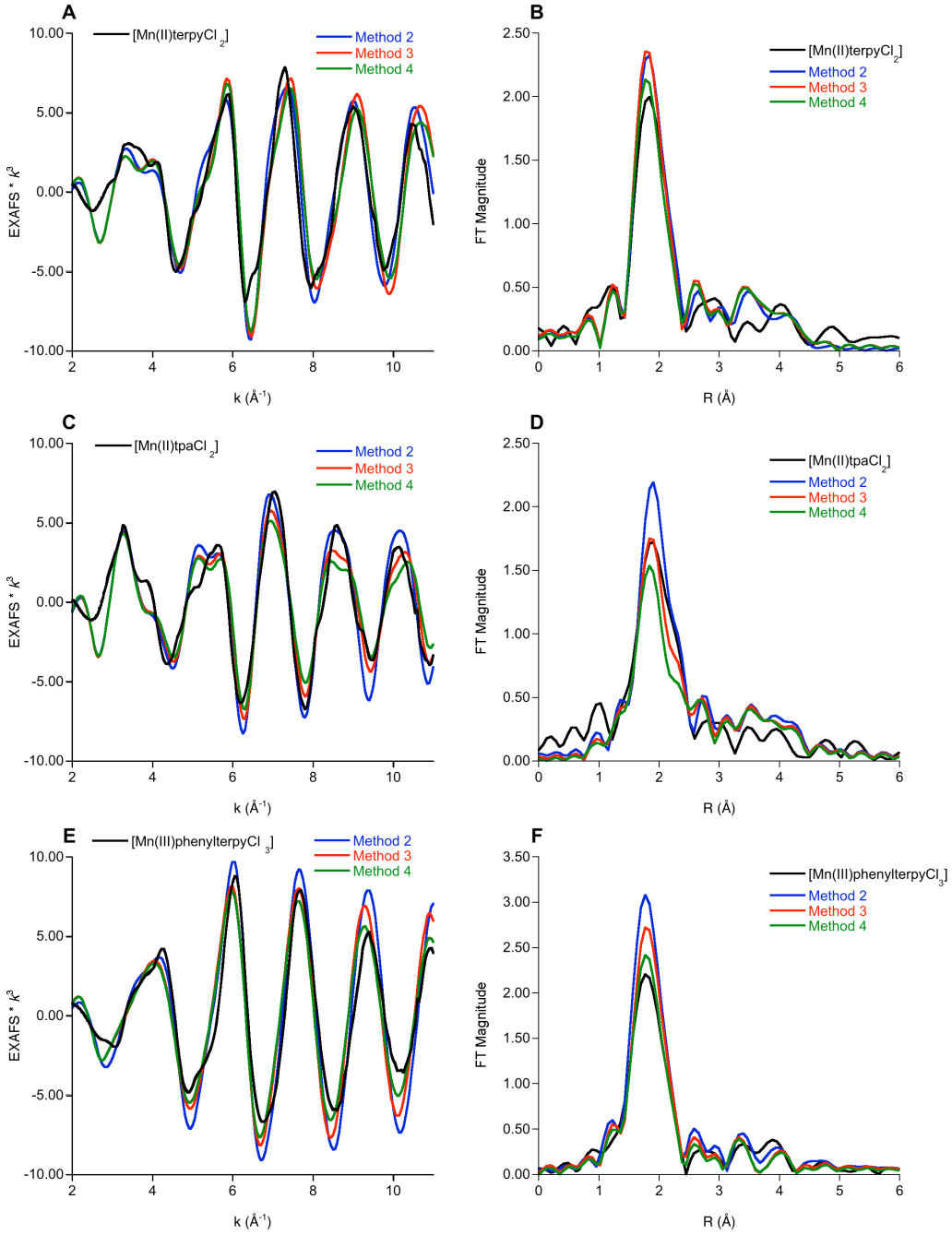

Figure 5.3. Experimental (black) and theoretical $\chi(k)$ spectra calculated using FEFF 9 and the corresponding non phase shift corrected FTs of [Mn(II)terpyCl$_2$] (A and B), [Mn(II)tpaCl$_2$] (C and D), and [Mn(III)phenylterpyCl$_3$] (E and F).

Table 5.4. Comparison of path distances and DW factors of the Mn monomer fits to those calculated from the crystal structures using the CD method in FEFF 9, and from the geometry optimized structures using the CD and DM methods in FEFF 9. All distances and DW factors shown are the average values for each scattering path. The numbers in parentheses correspond to the absolute deviation associated with each average value.

Path		Method 1	Method 2	Method 3	Method 4
			[Mn(II)terpyCl$_2$]		
Mn-N	R (Å)	**2.21**	2.24 (±0.02)	2.24 (±0.03)	2.24 (±0.03)
	σ^2 (Å^2)	**0.0044**	0.0031 (±1e-5)	0.0031 (±1e-5)	0.0032 (±1e-4)
Mn-Cl	R (Å)	**2.36**	2.36 (±0.01)	2.34 (±5e-3)	2.34 (±5e-3)
	σ^2 (Å^2)	**0.0025**	0.0017 (±5e-6)	0.0016 (±0)	0.0028 (±2e-5)
Mn-C[a]	R (Å)	**3.13, 4.62**	3.14 (±0.05), 4.55 (±0.13)	3.15 (±0.04), 4.63 (±0.18)	3.15 (±0.04), 4.63 (±0.18)
	σ^2 (Å^2)	**0.0061, 0.0034**	0.0037 (±8e-6), 0.0036 (±2e-5)	0.0037 (±9e-6), 0.0036 (±2e-5)	0.0035 (±4e-4), 0.0035 (±2e-4)
Mn-C-N	R (Å)	**3.26**	3.37 (±0.03)	3.36 (±0.16)	3.36 (±0.16)
	σ^2 (Å^2)	**0.0052**	0.0037 (±1e-5)	0.0039 (±2e-4)	0.0032 (±2e-4)
Error (F)[b]		**0.579**	0.733	1.55	1.30
			[Mn(II)tpaCl$_2$]		
Mn-N	R (Å)	**2.27**	2.33 (±0.04)	2.33 (±0.07)	2.33 (±0.07)
	σ^2 (Å^2)	**0.0067**	0.0031 (±2e-5)	0.0032 (±3e-5)	0.0036 (±3e-4)
Mn-Cl	R (Å)	**2.44**	2.44 (±0.02)	2.43 (±0.04)	2.43 (±0.04)
	σ^2 (Å^2)	**0.0025**	0.0017 (±0)	0.0017 (±1e-5)	0.0035 (±4e-4)
Mn-C[a]	R (Å)	**3.15, 4.68**	3.19 (±0.07), 4.53 (±0.05)	3.19 (±0.07), 4.53 (±0.05)	3.19 (±0.07), 4.53 (±0.05)
	σ^2 (Å^2)	**0.0026, 0.0075**	0.0037 (±1e-5), 0.0036 (±7e-6)	0.0037 (±1e-5), 0.0036 (±8e-6)	0.0040 (±3e-4), 0.0038 (±2e-4)
Mn-C-N	R (Å)	**3.44**	3.46 (±0.05)	3.46 (±0.06)	3.46 (±0.06)
	σ^2 (Å^2)	**0.0015**	0.0037 (±4e-5)	0.0038 (±4e-5)	0.0037 (±2e-4)
Error (F)		**0.511**	1.22	1.18	1.43
			[Mn(III)phenylterpyCl$_3$]		
Mn-N	R (Å)	**2.13**	2.17 (±0.06)	2.21 (±0.08)	2.21 (±0.08)
	σ^2 (Å^2)	**0.0062**	0.0031 (±3e-5)	0.0032 (±4e-5)	0.0030 (±2e-4)
Mn-Cl	R (Å)	**2.29**	2.27 (±0.01)	2.29 (±0.02)	2.29 (±0.02)
	σ^2 (Å^2)	**0.0049**	0.0016 (±4e-6)	0.0016 (±4e-6)	0.0026 (±1e-4)
Mn-C	R (Å)	**2.90**	3.07 (±0.07)	3.11 (±0.09)	3.11 (±0.09)
	σ^2 (Å^2)	**0.0018**	0.0037 (±1e-5)	0.0037 (±2e-5)	0.0032 (±5e-4)
Mn-C-N[a]	R (Å)	**4.51, 5.06**	4.47 (±0.06), 4.96 (±0.03)	4.51 (±0.06), 4.72 (±0.11)	4.51 (±0.06), 4.72 (±0.11)
	σ^2 (Å^2)	**0.0015, 0.0010**	0.0037 (±2e-5), 0.0043 (±5e-4)	0.0038 (±3e-5), 0.0041 (±6e-4)	0.0031 (±2e-4), 0.0033 (±4e-4)
Error (F)		**0.190**	1.24	0.767	0.402

[a]Two paths of this type were included in the fit to the data. The corresponding distances and DW factors are separated by commas.

[b]A measure of the error value (x10^3) between the experimental data and the EXAFS calculated via each method, where $F = \Sigma_i [k_i^3/(\Sigma_j k_j^3 |\chi^{expt}(k_j)|)]^2[\chi^{expt}(k_i) - \chi^{calc}(k_i)]^2$. In the case of method 1 the error is between the data and the final fit to the data.

Table 5.5. Differences between the final fit parameters (Method 1) and the FEFF 9 calculated parameters for the Mn monomers, using methods 2-4. Values have been obtained by subtracting the averaged fit values for a given path from the averaged calculated values for a given path.

Path		**Method 2 (absolute deviation)**	**Method 2 (percent deviation)**	**Method 3 (absolute deviation)**	**Method 3 (percent deviation)**	**Method 4 (absolute deviation)**	**Method 4 (percent deviation)**
Mn-Cl 2.3-2.4 Å	ΔR (Å)	-0.02 to 0	0 to 0.9%	-0.02 to 0	0 to 0.8%	-0.02 to 0	0 to 0.8%
	$\Delta\sigma^2$ (Å^2)	-0.0033 to -0.0008	32 to 67%	-0.0033 to -0.0008	32 to 67%	-0.0023 to +0.0010	12 to 47%
Mn-N 2.1-2.3 Å	ΔR (Å)	+0.03 to +0.06	1 to 3%	+0.03 to +0.08	1 to 4%	+0.03 to +0.08	1 to 4%
	$\Delta\sigma^2$ (Å^2)	-0.0036 to -0.0013	30 to 54%	-0.0035 to -0.0013	30 to 52%	-0.0032 to -0.0012	27 to 52%
Mn-C 2.9-3.2 Å	ΔR (Å)	+0.01 to +0.17	0.3 to 6%	+0.02 to +0.21	0.6 to 7%	+0.02 to +0.21	0.6 to 7%
	$\Delta\sigma^2$ (Å^2)	-0.0024 to +0.0019	39 to 106%	-0.0024 to +0.0019	39 to 106%	-0.0026 to +0.0014	43 to 78%

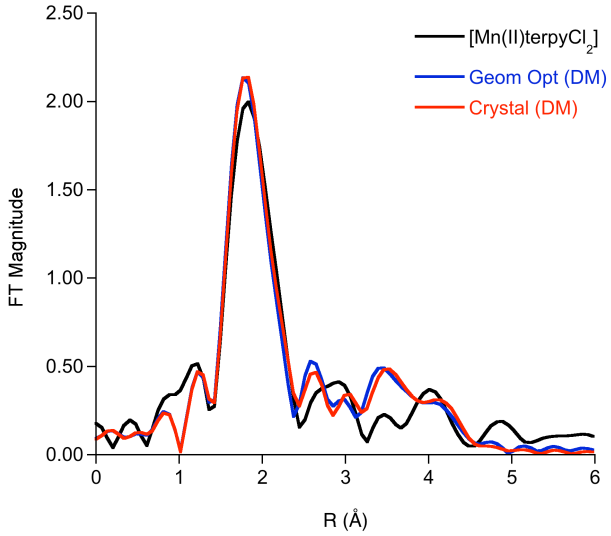

Figure 5.4. Non phase shift corrected FTs of the experimental (black) and theoretical EXAFS using the DM method at the geometry optimized (blue) and at the crystal (red) structure coordinates of [Mn(II)terpyCl$_2$].

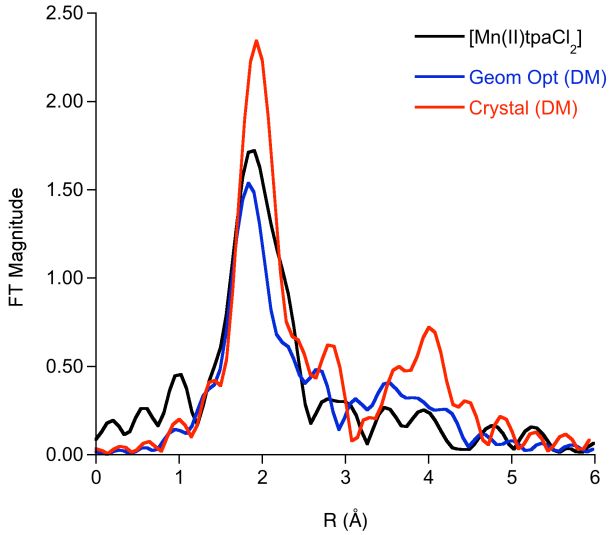

Figure 5.5. Non phase shift corrected FTs of the experimental (black) and theoretical EXAFS using the DM method at the geometry optimized (blue) and at the crystal (red) structure coordinates of [Mn(II)tpaCl_2].

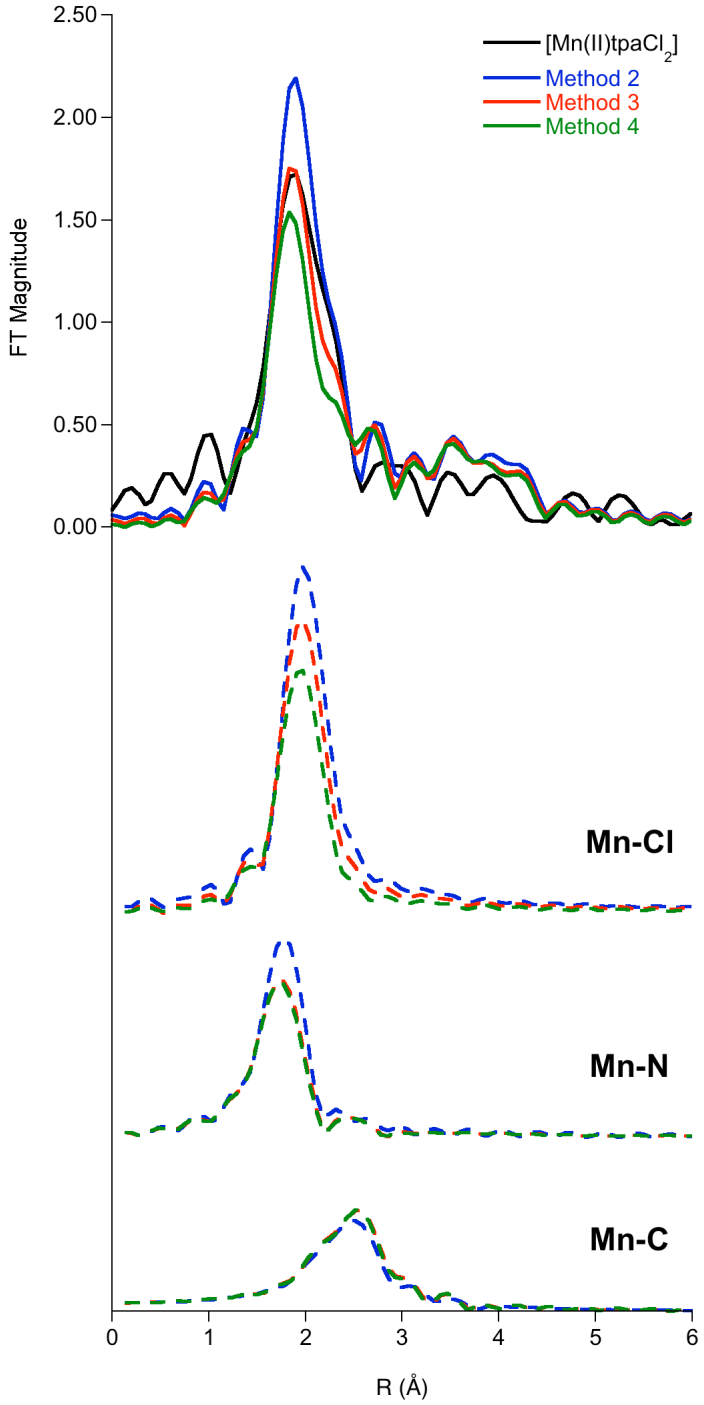

Figure 5.6. Calculated spectra and contributions of significant single scattering paths to the total spectra for [Mn(II)tpaCl$_2$]. The deconvolutions for each method are the sums of the individual scattering paths of each type.

Fits to the Mn Dimers EXAFS Data: Method 1. Given the generally good agreement between calculated and experimental spectra for the Mn monomers, it is of interest to extend these correlations to more complex Mn dimers. Figure 5.7 shows the fits to the Mn dimers, with the corresponding fit parameters summarized in Tables 5.6-5.9 and in Table 5.11, column 1. Table 5.10 shows the error values for the monomers and dimers after fitting, and prior to fitting using the Correlated Debye model in FEFF 7. The fits show good agreement with the experimental EXAFS, with error values (F x10^3) ranging from 0.37-0.66 over the dimer series. Similar to the monomers, the fit distances are reasonably close to the crystallographic distances.

Table 5.6. Best fit parameters for $[Mn_2(II)(\mu\text{-}OAc)_2tpa_2]^{2+}$. Standard deviations for the fit values are given in parentheses.

N	Path	R (Å)	σ^2 (Å^2)	ΔE_0 (eV)	F (x10^3)
2	Mn-O	2.12 (0.0051)	0.0044 (0.0009)	-3.184 (0.1874)	0.434
2	Mn-O	3.54 (0.0113)	0.0046 (0.0016)	-3.184	
4	Mn-N	2.28 (0.0042)	0.0049 (0.0007)	-3.184	
8	Mn-C	3.10 (0.0052)	0.0084 (0.0006)	-3.184	
1	Mn-Mn	4.11 (0.0077)	0.0030 (0.0010)	-3.184	
6	Mn-C-O	4.50 (0.0152)	0.0037 (0.0021)	-3.184	

Table 5.7. Best fit parameters for $[Mn_2(II)(\mu\text{-}SO_4)_2tpa_2]$. Standard deviations for the fit values are given in parentheses.

N	Path	R (Å)	σ^2 (Å^2)	ΔE_0 (eV)	F (x10^3)
2	Mn-O	2.15 (0.0034)	0.0016 (0.0005)	-3.056 (0.2331)	0.372
2	Mn-O	3.58 (0.0707)	0.0034 (0.0033)	-3.056	
4	Mn-N	2.33 (0.0033)	0.0029 (0.0004)	-3.056	
9	Mn-C	3.14 (0.0089)	0.0068 (0.0010)	-3.056	
1	Mn-Mn	4.23 (0.0136)	0.0058 (0.0015)	-3.056	
4	Mn-S-O	3.42 (0.0518)	0.0035 (0.0113)	-3.056	
8	Mn-O-O	3.91 (0.0317)	0.0037 (0.0070)	-3.056	

Table 5.8. Best fit parameters for $[Mn_2(III)(\mu\text{-}O)_2tpa_2]^{2+}$. Standard deviations for the fit values are given in parentheses.

N	Path	R (Å)	σ^2 (Å^2)	ΔE_0 (eV)	F (x10^3)
2	Mn-O	1.83 (0.0023)	0.0022 (0.0002)	-0.068 (0.3495)	0.662
4	Mn-N	2.23 (0.0138)	0.0280 (0.0029)	-0.068	
9	Mn-C	2.98 (0.0087)	0.0121 (0.0012)	-0.068	
1	Mn-Mn	2.63 (0.0022)	0.0014 (0.0002)	-0.068	
14	Mn-C-N	5.10 (0.0312)	0.0122 (0.0056)	-0.068	

Table 5.9. Best fit parameters for $[Mn_2(III,IV)(\mu\text{-}O)_2tpa_2]^{3+}$. Standard deviations for the fit values are given in parentheses.

N	Path	R (Å)	σ^2 (Å^2)	ΔE_0 (eV)	F (x10^3)
2	Mn-O	1.80 (0.0035)	0.0049 (0.0003)	-2.867 (0.3504)	0.429
4	Mn-N	2.02 (0.0061)	0.0128 (0.0007)	-2.867	
9	Mn-C	2.91 (0.0054)	0.0095 (0.0007)	-2.867	
1	Mn-Mn	2.63 (0.0030)	0.0021 (0.0002)	-2.867	
18	Mn-C-N	3.21 (0.0204)	0.0127 (0.0046)	-2.867	

Table 5.10. F values (x10^3) after fitting, and prior to fitting using DW factors calculated using Correlated Debye (CD) model, as well as using a global DW value of 0.0025 Å^2 in the FEFF 7 calculated spectra. The values for the best fit are given in bold. The F values prior to fitting for the dimers result from using only the first 60 FEFF calculated paths in EXAFSPAK.

Compound	CD	CD Float ΔE_0	Global DW	Global DW Float ΔE_0	Best Fit	Best Fit Fix ΔE_0
Monomers						
$[Mn(II)terpyCl_2]$	2.05823	1.13314	2.08328	1.10100	**0.579**	0.854313
$[Mn(II)tpaCl_2]$	2.62517	1.14601	2.69773	1.08449	**0.511**	0.558481
$[Mn(III)phenylterpyCl_3]$	2.81974	1.27642	2.43139	0.73916	**0.190**	0.333914
Dimers						
$[Mn_2(II)(\mu\text{-}OAc)_2tpa_2]^{2+}$	3.76333	0.98087	3.79276	0.97387	**0.434**	0.498389
$[Mn_2(II)(\mu\text{-}SO_4)_2tpa_2]$	2.30781	1.15582	2.26389	1.10454	**0.372**	0.182035
$[Mn_2(III)(\mu\text{-}O)_2tpa_2]^{2+}$	5.52279	0.91498	5.47243	0.97107	**0.662**	0.699640
$[Mn_2(III,IV)(\mu\text{-}O)_2tpa_2]^{3+}$	4.10749	1.98350	4.40131	2.45666	**0.429**	0.311015

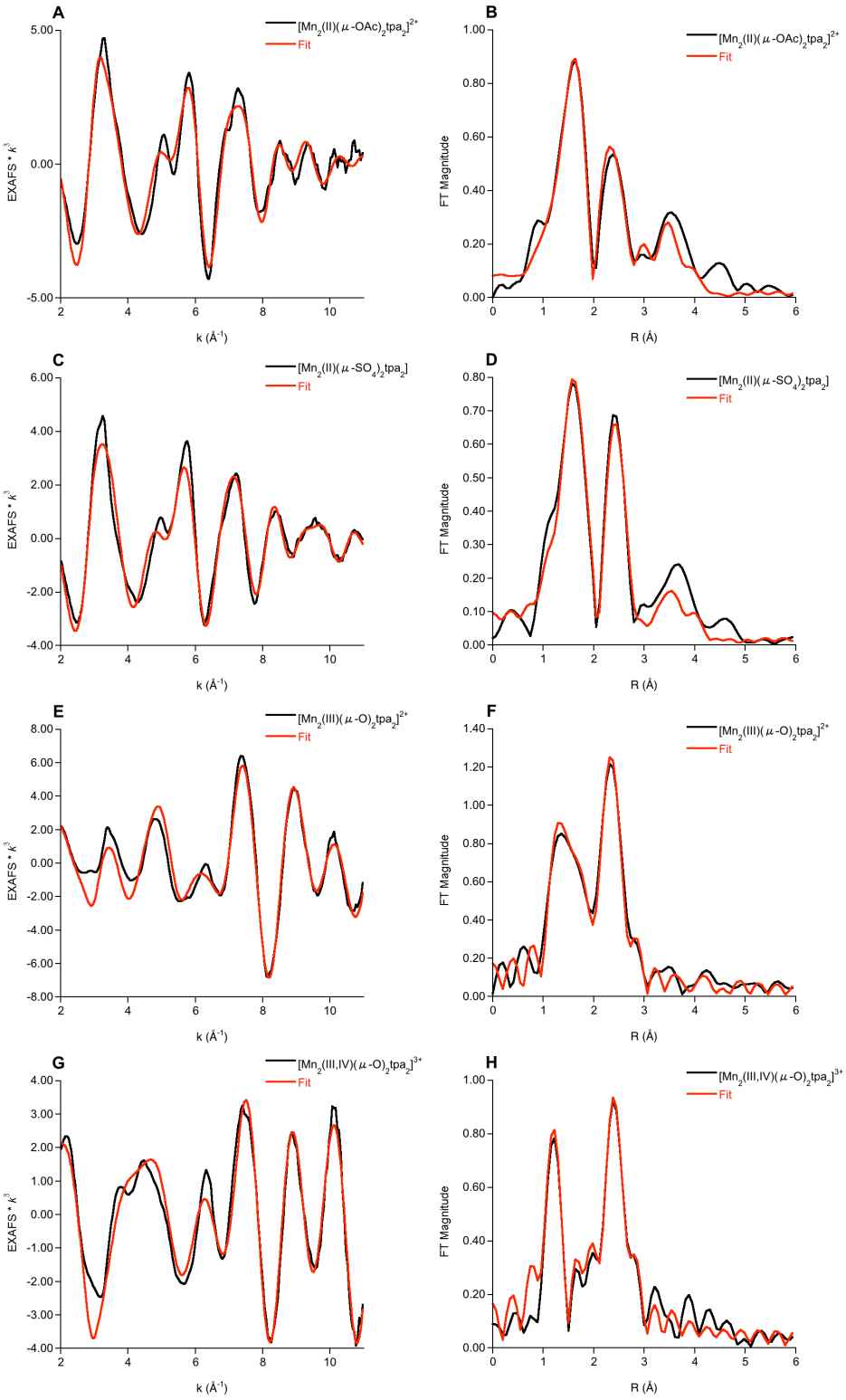

Figure 5.7. Experimental (black) and fits (red) to the $\chi(k)$ spectra and the corresponding non phase shift corrected FTs of $[Mn_2(II)(\mu\text{-}OAc)_2tpa_2]^{2+}$ (A and B), $[Mn_2(II)(\mu\text{-}SO_4)_2tpa_2]$ (C and D), $[Mn_2(III)(\mu\text{-}O)_2tpa_2]^{2+}$ (E and F), and $[Mn_2(III,IV)(\mu\text{-}O)_2tpa_2]^{3+}$ (G and H).

FEFF calculated EXAFS Spectra for the Mn Dimers: Methods 2-4.

The FEFF spectra calculated using methods 2-4 (first-principle calculations in the absence of fitting) are shown in Figure 5.8. In contrast to the monomers, the agreement between theory and experiment is generally rather poor. In all cases, the outer shell contributions to the FT are poorly predicted (Figure 5.8, right) and in some cases even the first shell FT deviates significantly from experiment (Figure 5.8F, 5.8H). The predicted outer shell FT intensities are particularly poor for the $[Mn_2(II)(\mu\text{-}OAc)_2tpa_2]^{2+}$ and $[Mn_2(II)(\mu\text{-}SO_4)_2tpa_2]$ dimers, which may be attributed to the more complex OAc and SO_4 bridging motifs (Figures 5.8B and 5.8D). This is also reflected in the error values of the calculated dimer spectra, which increase from the fit error values by a factor of up to a factor of ~23 (Table 5.11). In order to discern the origins of these differences, each computational approach is examined in detail below.

Method 2. Table 5.11 shows the differences between the FEFF calculations using the crystal structure (column 2) and the fits to the EXAFS data (column 1). Not only have the error values increased significantly compared to those of the fits, but the error values have also increased substantially relative to what was obtained for the monomers using the same method (Table 5.4, column 2). The first-shell distances (R between ~1 and 2 Å), and in some cases the second shell distances (R between ~2 and 3 Å), are very similar to the EXAFS fit distances, but there are larger discrepancies in the outer shells, particularly for $[Mn_2(II)(\mu\text{-}OAc)_2tpa_2]^{2+}$ and $[Mn_2(II)(\mu\text{-}SO_4)_2tpa_2]$.

Table 5.12 shows the differences between the calculations using method 2 and the fits to the data (method 1). The percent deviation in the calculated and fit distances for the first-shell Mn-O and Mn-N paths ranges from 0-4%, while those of the longer distance Mn-C single scattering and the multiple scattering paths range from 0.3-4% and 1-10%, respectively. The distance

differences for the Mn-Mn path greatly depend on the bridging structure in the dimer. For both the $[Mn_2(III)(\mu\text{-}O)_2tpa_2]^{2+}$ and $[Mn_2(III,IV)(\mu\text{-}O)_2tpa_2]^{3+}$ dimers (fit distance = 2.63 Å), there is good agreement between crystal structure and fit values, with ΔR = 0-0.4%. The agreement for the $[Mn_2(II)(\mu\text{-}OAc)_2tpa_2]^{2+}$ and $[Mn_2(II)(\mu\text{-}SO_4)_2tpa_2]$ dimers is somewhat worse (ΔR = 2% and 4%). This is most likely due to the longer Mn-Mn distances in these complexes, due to the OAc and SO_4 bridging ligands.

As observed for the monomers, the agreement between calculated and fit DW values also differs for the first-shell paths and the outer shell paths. As shown in Table 5.12, using method 2 the average calculated DW factors for the Mn dimers differ from the fit DW factors by ~10-89% for the first-shell paths, and by ~7-78% for the Mn-Mn path. The differences for the outer shell paths range from ~8-70%, however only the single scattering contributions to the outer shell are shown in Table 5.12. These results provide further evidence that the largest error in the FEFF calculated spectra is associated with the calculation of the mean square deviation in the bond lengths.

Method 3. The results of the calculations using method 3 for the Mn dimers are summarized in Figure 5.8 and Tables 5.11 and 5.12. As was observed for the monomers, the geometry optimized distances are quite similar to the crystallographic distances, with notable exceptions being the longer distance Mn-Mn paths in $[Mn_2(II)(\mu\text{-}OAc)_2tpa_2]^{2+}$ and $[Mn_2(II)(\mu\text{-}SO_4)_2tpa_2]$, which is attributed to the more flexible nature of the bridging ligands (as noted above). Overall the root mean square deviations between the crystallographic coordinates and the geometry optimized structures range from 0.124 to 0.538, indicating generally very good agreement. Also similar to the monomers, there is essentially no change in the calculated DW values between methods 2 and 3, as seen in Table 5.11.

There are, however, small changes in the first-shell FT intensities between method 2 and method 3, despite the calculated DW factors being almost identical. These intensity changes arise from differences in the bond length distribution, as was also observed for the monomers. This is more clearly seen in the deconvolution of $[Mn_2(II)(\mu\text{-}SO_4)_2tpa_2]$ as shown in Figure 5.9, specifically in the Mn-N contribution. The variation in individual Mn-N distances (2.25, 2.26, 2.31, and 2.36 Å (crystal structure, $\Delta R = 0.11$ Å) vs. 2.19, 2.23, 2.35, and 2.39 Å (geometry optimized structure, $\Delta R = 0.20$ Å)) results in a higher calculated total first-shell FT intensity for method 2 than for method 3. In the case of the outer shell Mn-Mn path in $[Mn_2(II)(\mu\text{-}SO_4)_2tpa_2]$, the 0.36 Å decrease in distance compared to the crystal structure results in poorer agreement between the calculated and fit spectra compared to the spectrum using the crystallographic distance, despite this path having the same calculated DW value for both the crystallographic and geometry optimized structures (Table 5.11 and Figure 5.9, right). This again emphasizes the importance of calculating both accurate distances *and* accurate DW factors if one wishes to make accurate spectral predictions.

It should be noted that in the deconvolution of $[Mn_2(III)(\mu\text{-}O)_2tpa_2]^{2+}$ (Figure 5.9, left) the intensities of all the individual path contributions are almost identical, yet the total FT intensities are different between methods 2 and 3. This discrepancy in the deconvolution is most likely due to differences in the interference between the calculated paths.

Method 4. The results of the FEFF calculated spectra using the DMDW code are summarized in Figure 5.8 and Tables 5.11 and 5.12. In general, the DW factors calculated using method 4 differ from the fit values from method 1 by ~9-119% for the first-shell paths, by ~16-118% for outer shell paths, and by ~7-40% for the Mn-Mn path. These differences are similar to those for methods 2 and 3 (first-shell ~10-88%, outer shell ~8-70%, Mn-Mn ~7-78%), indicating that method 4 can provide slightly better calculated DW values than either method 2 or 3, though the

deviations are still significant. Unlike with the monomers, the spectra calculated using method 4 are almost identical to those calculated using method 3, particularly for R < 3 Å. A quantitative assessment shows that while the DW values for the individual paths vary between method 3 and 4, the average values are sufficiently similar to result in nearly identical calculated spectra at R < 3 Å.

There are, however, more noticeable differences in the calculated spectra using these two methods at R > 3 Å for the $[Mn_2(II)(\mu\text{-}OAc)_2tpa_2]^{2+}$ and $[Mn_2(II)(\mu\text{-}SO_4)_2tpa_2]$ dimers. As can be seen in the deconvolution of $[Mn_2(II)(\mu\text{-}SO_4)_2tpa_2]$ (Figure 5.9, right), these differences arise mainly from intensity differences in the Mn-Mn path, and to a lesser extent from differences in the outer shell Mn-O path (average distance = 3.49 Å). In both cases, the DW values calculated using method 4 are more than two times the DW values calculated using method 3 (Table 5.11). However, the total spectra are more dominated by the changes in the Mn-Mn path. This highlights the fact that EXAFS is ideally suited for obtained accurate Mn-Mn vectors, but more limited in defining the metrics of bridging light atoms.

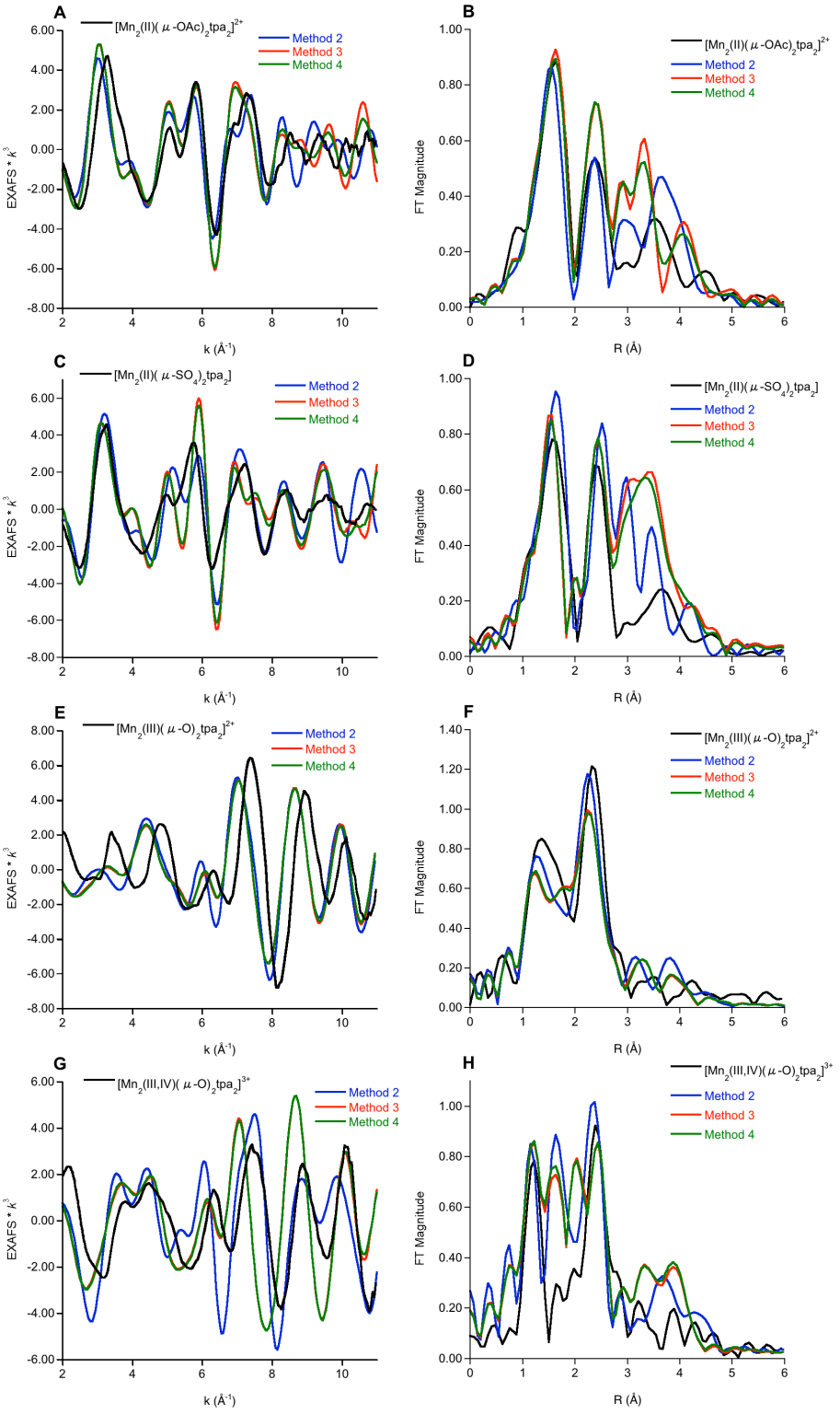

Figure 5.8. Experimental (black) and theoretical $\chi(k)$ spectra calculated using FEFF 9 and the corresponding non phase shift corrected FTs of $[Mn_2(II)(\mu\text{-}OAc)_2tpa_2]^{2+}$ (A and B), $[Mn_2(II)(\mu\text{-}SO_4)_2tpa_2]$ (C and D), $[Mn_2(III)(\mu\text{-}O)_2tpa_2]^{2+}$ (E and F), and $[Mn_2(III,IV)(\mu\text{-}O)_2tpa_2]^{3+}$ (G and H).

Table 5.11. Comparison of path distances and DW factors of the Mn dimer fits to those calculated from the crystal structures using the CD method in FEFF 9, and from the geometry optimized structures using the CD and DM methods in FEFF 9. All distances and DW factors shown are the average values for each scattering path. The numbers in parentheses correspond to the absolute deviation associated with each average value.

Path		Method 1	Method 2	Method 3	Method 4
			[Mn$_2$(II)(μ-OAc)$_2$tpa$_2$]$^{2+}$		
Mn-O[a]	R (Å)	**2.12, 3.54**	2.12 (±0.04), 3.59 (±0.20)	2.13 (±0.07), 3.49 (±0.11)	2.13 (±0.07), 3.49 (±0.11)
	σ^2 (Å^2)	**0.0044, 0.0046**	0.0029 (±2e-5), 0.0028 (±5e-6)	0.0029 (±3e-5), 0.0028 (±0)	0.0039 (±8e-4), 0.0064 (±6e-5)
Mn-N	R (Å)	**2.28**	2.25 (±0.07)	2.27 (±0.06)	2.27 (±0.06)
	σ^2 (Å^2)	**0.0049**	0.0033 (±2e-5)	0.0032 (±1e-5)	0.0033 (±3e-4)
Mn-C	R (Å)	**3.10**	3.15 (±0.06)	3.18 (±0.13)	3.18 (±0.13)
	σ^2 (Å^2)	**0.0084**	0.0036 (±9e-6)	0.0036 (±7e-6)	0.0037 (±4e-4)
Mn-Mn	R (Å)	**4.11**	4.20	3.99	3.99
	σ^2 (Å^2)	**0.0030**	0.0013	0.0013	0.0036
Mn-C-O	R (Å)	**4.50**	4.65 (±0.22)	4.70 (±0.28)	4.70 (±0.28)
	σ^2 (Å^2)	**0.0037**	0.0042 (±7e-4)	0.0045 (±7e-4)	0.0046 (±3e-4)
Error (F)[b]		**0.434**	3.09	3.37	2.89
			[Mn$_2$(II)(μ-SO$_4$)$_2$tpa$_2$]		
Mn-O[a]	R (Å)	**2.14, 3.58**	2.10 (±0.03), 3.34 (±0.02)	2.09 (±0.04), 3.49 (±1e-3)	2.09 (±0.04), 3.49 (±1e-3)
	σ^2 (Å^2)	**0.0016, 0.0034**	0.0028 (±2e-5), 0.0029 (±5e-6)	0.0028 (±3e-5), 0.0028 (±0)	0.0035 (±3e-4), 0.0074 (6e-5)
Mn-N	R (Å)	**2.33**	2.30 (±0.04)	2.29 (0.08)	2.29 (±0.08)
	σ^2 (Å^2)	**0.0029**	0.0032 (±2e-5)	0.0032 (±2e-5)	0.0035 (±5e-4)
Mn-C	R (Å)	**3.14**	3.15 (±0.05)	3.23 (±0.17)	3.23 (±0.17)
	σ^2 (Å^2)	**0.0068**	0.0036 (±9e-6)	0.0036 (±1e-5)	0.0040 (±5e-4)
Mn-Mn	R (Å)	**4.23**	4.42	4.06	4.06
	σ^2 (Å^2)	**0.0058**	0.0013	0.0013	0.0035
Mn-S-O	R (Å)	**3.42**	3.42 (±0.03)	3.44 (±0.06)	3.44 (±0.06)
	σ^2 (Å^2)	**0.0035**	0.0020 (±1e-5)	0.0020 (±4e-5)	0.0025 (±2e-4)
Mn-O-O	R (Å)	**3.91**	4.13 (±0.23)	4.16 (±0.23)	4.16 (±0.23)
	σ^2 (Å^2)	**0.0037**	0.0033 (±3e-4)	0.0034(±3e-4)	0.0043 (±3e-4)
Error (F)		**0.372**	2.68	4.13	3.46
			[Mn$_2$(III)(μ-O)$_2$tpa$_2$]$^{2+}$		
Mn-O	R (Å)	**1.83**	1.83 (±2e-3)	1.84 (±1e-3)	1.84 (±1e-3)
	σ^2 (Å^2)	**0.0022**	0.0027 (±5e-6)	0.0027 (±0)	0.0024 (±4e-4)
Mn-N	R (Å)	**2.23**	2.24 (±0.09)	2.21 (±0.10)	2.21 (±0.10)
	σ^2 (Å^2)	**0.0280**	0.0032 (±3e-5)	0.0032 (±4e-5)	0.0030 (±3e-4)
Mn-C	R (Å)	**2.98**	3.10 (±0.10)	3.06 (±0.11)	3.06 (±0.11)
	σ^2 (Å^2)	**0.0121**	0.0036 (±2e-5)	0.0036 (±2e-5)	0.0034 (±4e-4)
Mn-Mn	R (Å)	**2.63**	2.64	2.66	2.66
	σ^2 (Å^2)	**0.0014**	0.0013	0.0013	0.0015
Mn-C-N	R (Å)	**5.10**	4.59 (±0.12)	4.61 (±0.15)	4.61 (±0.15)
	σ^2 (Å^2)	**0.0122**	0.0038 (±4e-5)	0.0038 (±4e-5)	0.0033 (±3e-4)
Error (F)		**0.662**	11.0	11.0	10.8
			[Mn$_2$(III,IV)(μ-O)$_2$tpa$_2$]$^{3+}$		
Mn-O	R (Å)	**1.80**	1.81 (±8e-3)	1.83 (±0.04)	1.83 (±0.04)
	σ^2 (Å^2)	**0.0049**	0.0026 (±1e-5)	0.0027 (±7e-5)	0.0023 (±2e-4)
Mn-N	R (Å)	**2.02**	2.10 (±0.03)	2.10 (±0.09)	2.10 (±0.09)
	σ^2 (Å^2)	**0.0128**	0.0032 (±2e-5)	0.0032 (±6e-5)	0.0027 (±3e-4)
Mn-C	R (Å)	**2.91**	2.97 (±0.08)	2.98 (±0.09)	2.98 (±0.09)
	σ^2 (Å^2)	**0.0095**	0.0037 (±7e-3)	0.0037 (±2e-5)	0.0031 (±3e-4)
Mn-Mn	R (Å)	**2.63**	2.63	2.66	2.66
	σ^2 (Å^2)	**0.0021**	0.0013	0.0013	0.0015
Mn-C-N	R (Å)	**3.21**	3.23 (±0.04)	3.24 (±0.09)	3.24 (±0.09)
	σ^2 (Å^2)	**0.0127**	0.0038 (±6e-5)	0.0038 (±6e-5)	0.0029 (±3e-4)
Error (F)		**0.429**	6.19	9.95	10.0

[a]Two paths of this type were included in the fit to the data. The corresponding distances and DW factors are

separated by commas.
[b]A measure of the error value ($x10^3$) between the experimental data and the EXAFS calculated via each method, where $F = \Sigma_i [k_i^3/(\Sigma_j k_j^3 |\chi^{expt}(k_j)|)]^2[\chi^{expt}(k_i) - \chi^{calc}(k_i)]^2$. In the case of method 1 the error is between the data and the final fit to the data.

Table 5.12. Differences between the final fit parameters and the FEFF 9 calculated parameters for the Mn dimers, using methods 2-4. Values have been obtained by subtracting the averaged fit values for a given path from the averaged calculated values for a given path.

Path		**Method 2 (absolute deviation)**	**Method 2 (percent deviation)**	**Method 3 (absolute deviation)**	**Method 3 (percent deviation)**	**Method 4 (absolute deviation)**	**Method 4 (percent deviation)**
Mn-O 1.8-2.1 Å	ΔR (Å)	-0.04 to +0.01	0 to 2%	-0.05 to +0.03	0 to 2%	-0.05 to +0.03	0 to 2%
	$\Delta\sigma^2$ (Å^2)	-0.0023 to +0.0012	23 to 75%	-0.0022 to +0.0012	23 to 75%	-0.0026 to +0.0019	9 to 119%
Mn-N 2.0-2.3 Å	ΔR (Å)	-0.03 to +0.08	0.4 to 4%	-0.04 to +0.08	0.4 to 4%	-0.04 to +0.08	0.4 to 4%
	$\Delta\sigma^2$ (Å^2)	-0.0248 to +0.0003	10 to 89%	-0.0248 to +0.0003	10 to 89%	-0.025 to +0.0006	21 to 89%
Mn-C 2.9-3.1 Å	ΔR (Å)	+0.01 to +0.12	0.3 to 4%	+0.07 to +0.09	2 to 3%	+0.07 to +0.09	2 to 3%
	$\Delta\sigma^2$ (Å^2)	-0.0085 to -0.0032	47 to 70%	-0.0085 to -0.0032	47 to 70%	-0.0087 to -0.0028	41 to 72%
Mn-Mn (short) 2.63 Å	ΔR (Å)	0 to +0.01	0 to 0.4%	+0.03	1%	+0.03	1%
	$\Delta\sigma^2$ (Å^2)	-0.0008 to -0.0001	7 to 38%	-0.0008 to -0.0001	7 to 38%	-0.0006 to +0.0001	7 to 29%
Mn-Mn (long) 4.1-4.2 Å	ΔR (Å)	+0.09 to +0.19	2 to 4%	-0.17 to -0.12	3 to 4%	-0.17 to -0.12	3 to 4%
	$\Delta\sigma^2$ (Å^2)	-0.0045 to -0.0017	57 to 78%	-0.0045 to -0.0017	57 to 78%	-0.0023 to +0.0006	20 to 40%

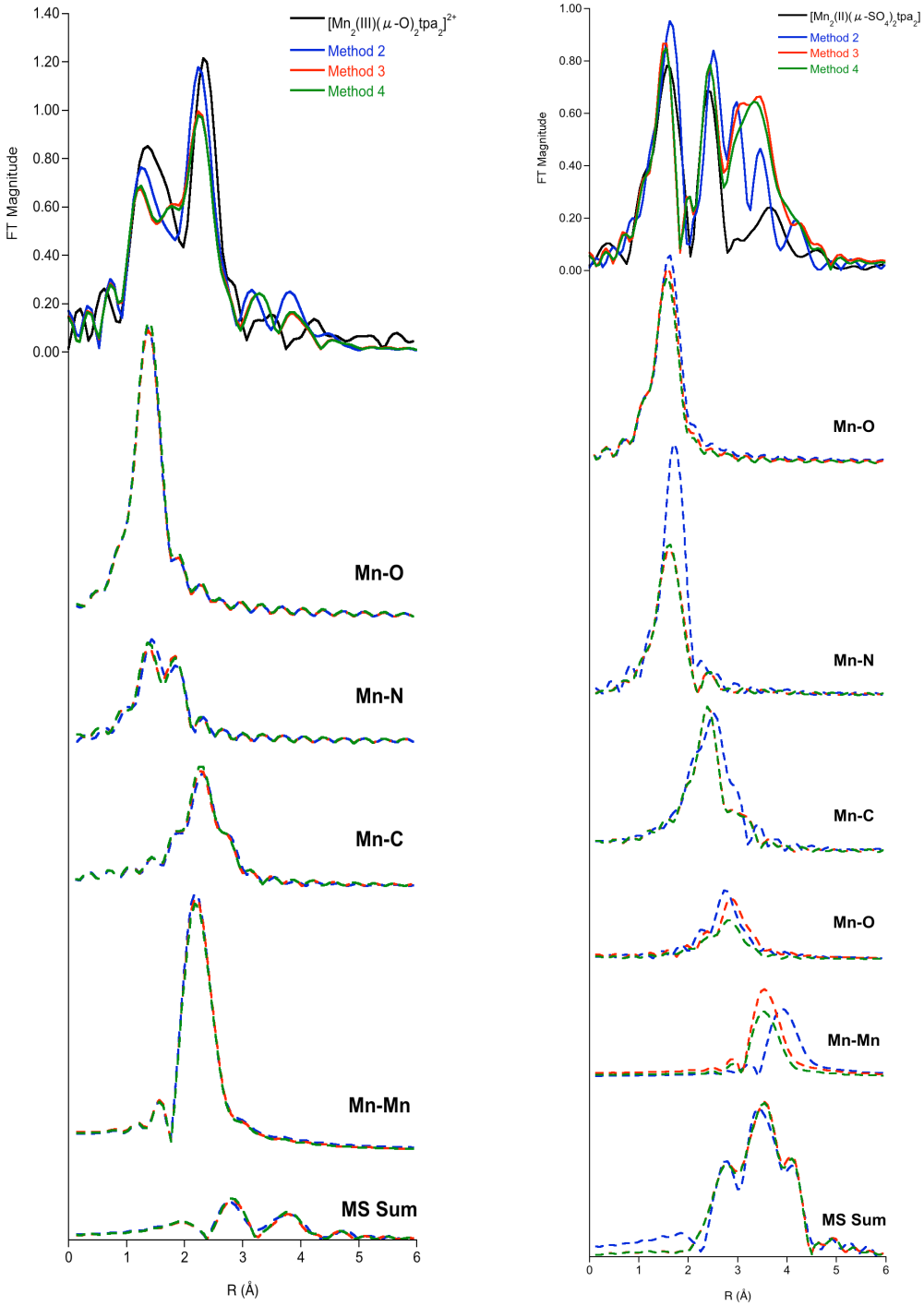

Figure 5.9. Calculated spectra and significant single and multiple scattering contributions for $[Mn_2(III)(\mu\text{-}O)_2tpa_2]^{2+}$ (left) and $[Mn_2(II)(\mu\text{-}SO_4)_2tpa_2]$ (right). The path deconvolutions for each method are the sums of the individual scattering paths of each type.

Application to the OEC. The analysis of the fits and calculations of the relatively simple model complexes can be extended to the OEC of PSII. Tables 5.5 and 5.12 show differences between calculated and fit distances and DW factors for significant paths for the monomers and dimers. These ranges of differences can be used to determine a window into which calculated EXAFS spectra of PSII models should fall in order for the proposed models to be considered reasonable when compared to the experimental data. This approach has been applied to 4 proposed models which are based on the Siegbahn, Barber II, Shen and Batista R-QM/MM models (Scheme 5.1, Models A-D, respectively). The coordinates used for models A and B were those of the optimized open cubane and closed cubane models of Pantazis et. al. that resembled the structures of Siegbahn and Barber.[24] Two model motifs, frozen and relaxed, were considered. In the frozen models, the positions of the four Mn atoms and the Ca atom were constrained to the be the same as in the 1.9 Å crystal structure (Scheme 5.1, Model C), while the positions of all other atoms in the models were allowed to relax during the geometry optimizations. In the relaxed models, all atom positions were allowed to move during the geometry optimizations, including the Mn and Ca atoms. For model D, the coordinates used were taken directly from reference 20 without any geometry optimization.

Upon relaxation, three of the Mn-Mn distances in model A decrease compared to the frozen model: the distances decrease from 2.97 Å (Mn_3-Mn_4), 2.89 Å (Mn_2-Mn_3) and 2.84 Å (Mn_1-Mn_2) in the frozen model to 2.76 Å (Mn_3-Mn_4), 2.80 Å (Mn_2-Mn_3) and 2.81 Å (Mn_1-Mn_2) in the fully relaxed model A. The Mn_1-Mn_3 distance increases from 3.29 Å to 3.38 Å going from the frozen model to model A. Thus, model A when fully geometry optimized is similar to the "dimer of dimers" models proposed by J. Yano et al.[15] As in model A, upon relaxation three of the Mn-Mn distances in model B decrease, yielding distances of 2.77 Å (Mn_2-Mn_3), 2.75 Å (Mn_1-Mn_2) and 2.89 Å (Mn_1-Mn_3). In the case of this model, the Mn_3-Mn_4 distance increases from 2.97 Å to

3.13 Å. Model B, then, is similar to other proposed models that involve a Mn_3Ca "distorted cubane" structure with a fourth "dangler" Mn atom. Relaxed structures of only models A and B were considered because a chemically reasonable relaxed structure was unable to be obtained for model C.

Figure 5.10 shows the experimental EXAFS FT of the S_2 state PSII, along with corresponding FTs of the models for comparison. All of the EXAFS of the models were calculated using FEFF 9 and the DW factors were calculated using the Correlated Debye Model.

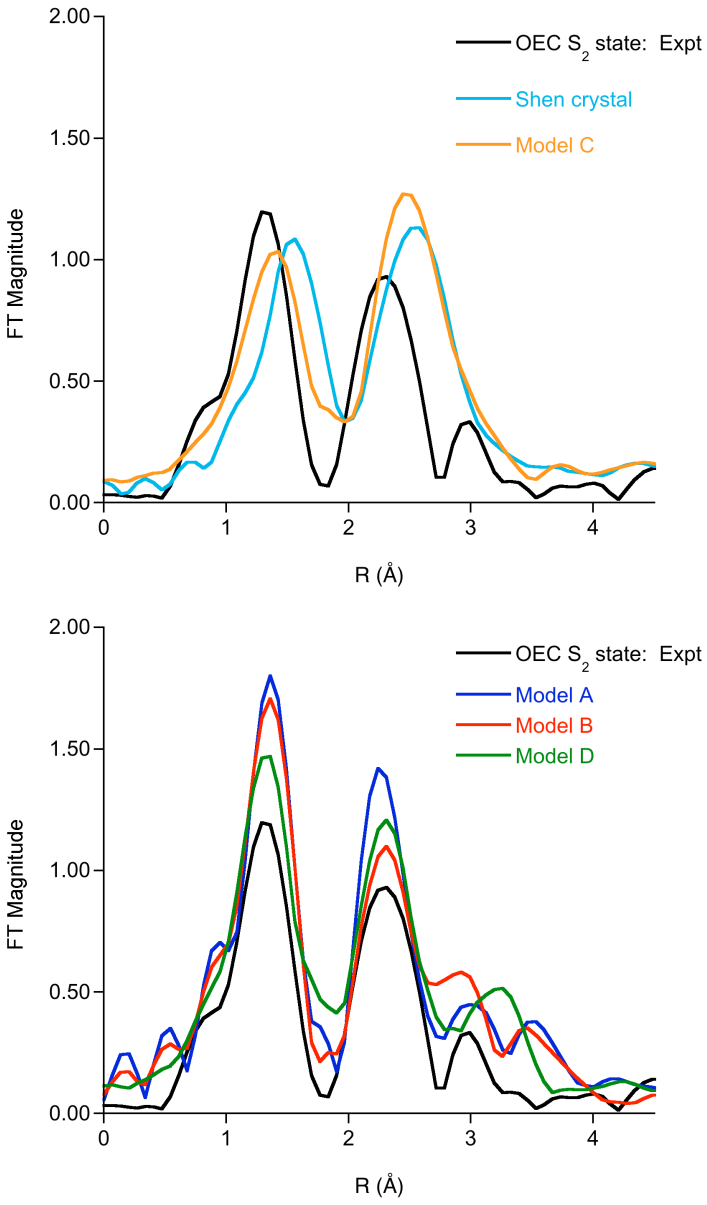

Figure 5.10. FT of the experimental EXAFS spectrum of the OEC S_2 state (black),[21] and the calculated FTs of the EXAFS of the OEC active site using the Shen crystal structure and model C (top), and the relaxed S_2 state models A and B, and model D (bottom). All spectra of the models were calculated using FEFF 9 and the Correlated Debye Model.

Clearly, both the relaxed models A and B, and model D, are qualitatively better matches to the experimental data than either the Shen crystal structure or the Shen model C using frozen Mn and Ca atoms, particularly in the second shell between 2 and 3 Å. The differences between the EXAFS of the frozen and crystal Shen models arise from shorter Mn-O distances in the frozen

model C, which results in better agreement between theory and experiment in the first shell of the FT, and also from a larger number of multiple scattering contributions between 2 and 3 Å, resulting in the second shell peak of the FT for the frozen model C shifting to lower energy and increasing in intensity compared to that of the crystal structure. This highlights the utility of EXAFS for distinguishing between slight structural variations despite the same general structural motif.

However, this alone cannot rule out a particular model given the uncertainty in predicted DW factors. In contrast, given the better accuracy in predicting distances, the Shen models can be excluded based on the second shell peak in the FT. To illustrate the uncertainty in calculated DW factors, Figure 5.11 shows the FT of the experimental S_2 state data along with the spectra of model A calculated using the upper and lower limits of the DW values based on the ranges obtained from the Mn dimer model complexes (Table 5.12). Figure 5.12 shows the corresponding EXAFS for model B.

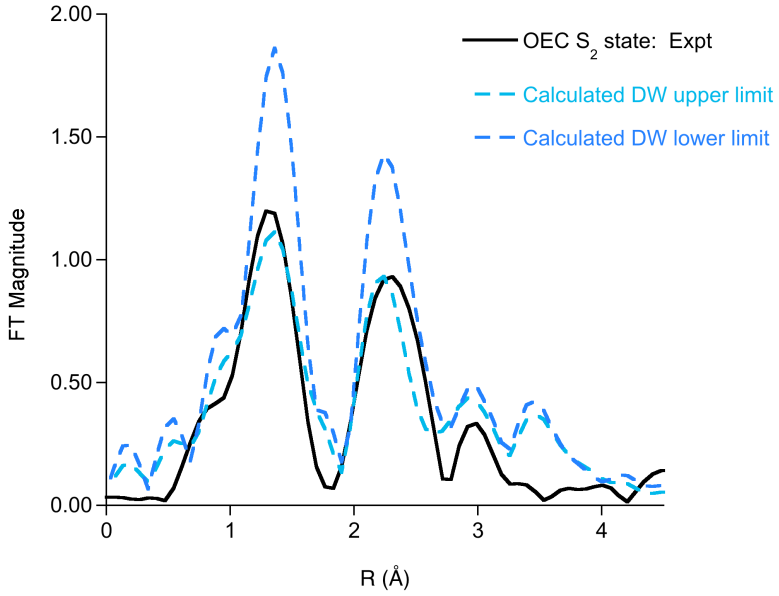

Figure 5.11. FT of the experimental EXAFS spectrum of the PS II S_2 state (black),[21] and the calculated FTs of the EXAFS of the relaxed model A using the upper and lower limits of the DW values based on those from the Mn dimer model complexes.

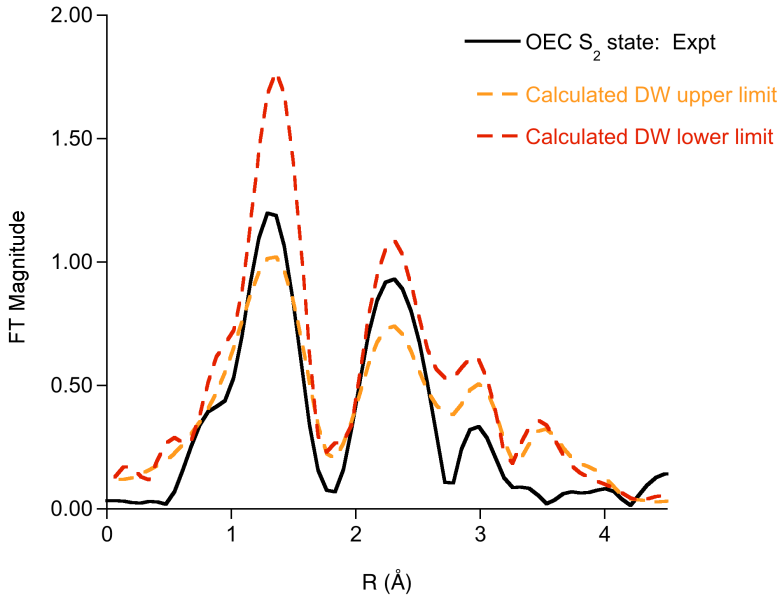

Figure 5.12. FT of the experimental EXAFS spectrum of the PS II S_2 state (black),[21] and the calculated FTs of the EXAFS of the relaxed model B using the upper and lower limits of the DW values based on those from the Mn dimer model complexes.

If one takes these ranges into account, neither the two relaxed models A and B nor model D can be considered better than the others based on EXAFS alone, further supporting the conclusion of Pantazis et. al. that structures A and B coexist in the S_2 state. This has important implications for future comparisons of experimental and calculated EXAFS data of other S-states of PSII, as well as other active sites in biological systems, such as ribonucleotide reductase, methane monooxygenase, and laccase.

Discussion and Conclusions

A study of the EXAFS of seven Mn monomers and dimers has been presented in order to assess the accuracy of spectra calculated from known crystallographic models, and by extension the accuracy of the calculated EXAFS when applied to more complex systems, such as the OEC of PSII. Four calculation methods were examined: FEFF calculated spectra using known crystal structures and the Correlated Debye (CD) model for calculating DW factors were fit to

experimental data (method 1), spectra calculated using crystallographic structures and the CD model without any fitting of parameters (method 2), and spectra calculated using geometry optimized structures and two methods for calculated DW factors, the CD model and Dynamical Matrix model that involves using frequency from DFT, in the absence of fitting (methods 3 and 4, respectively).

The values obtained from least square fitting of parameters resulted in EXAFS spectra that were in generally good agreement with the experimental data. This, however, is just the expected outcome as has been amply demonstrated in the EXAFS literature. The more intriguing question that has motivated this study – how accurately can one *predict* EXAFS spectra from first principles *without* any fitting or recourse to experimental data – has, however, a different answer. In fact, the present study demonstrates that despite all recent progress the *ab initio* prediction of the EXAFS spectra of molecules still faces significant problems and cannot be considered to be uniformly accurate. This can not be attributed to the theoretical geometry optimized structures that are generally of good to very good quality upon using present state-of-the-art DFT. The difficulty lies in predicting accurate Debye-Waller factors for the multitude of scattering pathways that underlie every EXAFS analysis. Thus, before these theoretical problems are overcome it will not be highly reliable to compare theoretically predicted EXAFS spectra to experimental ones in an attempt to validate structural proposals. While such an approach may work in selected cases, the overall situation is such that general conclusions about the quality of theoretical structures should hardly be drawn on the basis of theoretically calculated EXAFS spectra.

Specifically, the agreement between the calculated EXAFS in absence of fitting and the experimental data demonstrated that in particular the first shell (R between 0 and 2.5 Å) is predicted reasonably well. However, the agreement between calculated and fit distances

deteriorates for outer shell paths at longer distances. The largest error in the FEFF calculated spectra, however, is associated with the calculation of the DW factors. For all complexes, the DW factors calculated using the Correlated Debye model at either optimized or experimental structures were nearly identical. Using the much more sophisticated DM method (method 4) can in most cases improve the agreement between calculated and fit values but, unfortunately, not to the extent that accurate predictions of EXAFS spectra are obtained. The shortcomings of the theoretically predicted EXAFS spectra were particularly pronounced for the dimers included in this work: how well the calculated distances and DW factors were predicted depended on the bridging structure in the dimer. Both distances and DW factors were closer to those in the experiment for the shorter Mn-Mn distances resulting from the $(\mu\text{-O})_2$ bridging motif.

This point is emphasized so strongly because there are multiple attempts in the literature to back up experimentally obtained EXAFS spectra by recourse to theoretically calculated ones, in particular with respect to the oxygen-evolving complex in photosystem II. It is shown here that using such predicted spectra, it is *not* possible to properly differentiate between the main structural proposals that are presently under debate. More precisely, the "frozen models" for the OEC can, in fact, be ruled out as unreasonable based on the disagreement with the experimental data in the second shell of the FT. However, both models A and B, and model D, were all found to be reasonable based solely on the EXAFS spectra and the associated uncertainty in DW factors determined from the examination of the monomer and dimer calculations. None of those models, however, led to an accurately predicted EXAFS spectrum. In the author's opinion this reflects foremost the uncertainties in the theoretical modelling rather than the errors in the theoretical structures. However and importantly, despite the differences in the theoretical structures, their calculated EXAFS spectra are all about equally far off from experiment and hence no sound conclusions that favor one structure over the other can be drawn. Previous

attempts that claimed the contrary were all based on EXAFS modelling that was at most as sophisticated as method 3 in this chapter, but mostly invoked the even less accurate approach of using global Debye-Waller factors. Thus, the present study indicates that the conclusions derived from comparing experimental to calculated EXAFS spectra in the previous works on the OEC are not valid.

The conclusions of this work have far reaching implications for the use of theoretical EXAFS modelling, not only in biochemistry but in all major branches of chemistry where EXAFS analysis plays an important role. This work is a motivation and inspiration to direct future efforts towards improving the theoretical prediction of EXAFS spectra to make it an even more powerful partner of experimental investigations.

References

1. Wolff, T. E.; Berg, J. M.; Warrick, C.; Hodgson, K. O.; Holm, R. H.; Frankel, R. B., *J. Am. Chem. Soc.* **1978,** *100*, 4629.
2. Lieberman, R. L.; Kondapalli, K. C.; Shrestha, D. B.; Hakemian, A. S.; Smith, S. M.; Telser, J.; Kuzelka, J.; Gupta, R.; Borovik, A. S.; Lippard, S. J.; Hoffman, B. M.; Rosenzweig, A. C.; Stemmler, T. L., *Inorg. Chem.* **2006,** *45*, 8372.
3. Rudd, D. J.; Sazinsky, M. H.; Merkx, M.; Lippard, S. J.; Hedman, B.; Hodgson, K. O., *Inorg. Chem.* **2004,** *43*, 4579.
4. Younker, J. M.; Krest, C. M.; Jiang, W.; Krebs, C.; Bollinger, J. M.; Green, M. T., *J. Am. Chem. Soc.* **2008,** *130*, 15022.
5. Stone, K. L.; Behan, R. K.; Green, M. T., *Proc. Natl. Acad. Sci. U. S. A.* **2005,** *102*, 16563.
6. Behan, R. K.; Green, M. T., *J. Inorg. Biochem.* **2006,** *100*, 448.
7. Ryde, U.; Hsiao, Y. W.; Rulisek, L.; Solomon, E. I., *J. Am. Chem. Soc.* **2007,** *129*, 726.
8. Kirby, J. A.; Robertson, A. S.; Smith, J. P.; Thompson, A. C.; Cooper, S. R.; Klein, M. P., *J. Am. Chem. Soc.* **1981,** *103*, 5529.
9. Dau, H.; Andrews, J. C.; Roelofs, T. A.; Latimer, M. J.; Liang, W. C.; Yachandra, V. K.; Sauer, K.; Klein, M. P., *Biochemistry* **1995,** *34*, 5274.
10. Cinco, R. M.; Holman, K. L. M.; Robblee, J. H.; Yano, J.; Pizarro, S. A.; Bellacchio, E.; Sauer, K.; Yachandra, V. K., *Biochemistry* **2002,** *41*, 12928.
11. Mishra, A.; Yano, J.; Pushkar, Y.; Yachandra, V. K.; Abboud, K. A.; Christou, G., *Chem. Comm.* **2007**, 1538.
12. Cinco, R. M.; Robblee, J. H.; Messinger, J.; Fernandez, C.; Holman, K. L. M.; Sauer, K.; Yachandra, V. K., *Biochemistry* **2004,** *43*, 13271.
13. Cinco, R. M.; Robblee, J. H.; Rompel, A.; Fernandez, C.; Yachandra, V. K.; Sauer, K.; Klein, M. P., *J. Phys. Chem. B* **1998,** *102*, 8248.
14. Pushkar, Y.; Yano, J.; Glatzel, P.; Messinger, J.; Lewis, A.; Sauer, K.; Bergmann, U.; Yachandra, V., *J. Biol. Chem.* **2007,** *282*, 7198.
15. Yano, J.; Kern, J.; Sauer, K.; Latimer, M. J.; Pushkar, Y.; Biesiadka, J.; Loll, B.; Saenger, W.; Messinger, J.; Zouni, A.; Yachandra, V. K., *Science* **2006,** *314*, 821.
16. Dismukes, G. C.; Siderer, Y., *Proc. Natl. Acad. Sci. U.S.A.-Biol. Sci.* **1981,** *78*, 274.
17. Peloquin, J. M.; Britt, R. D., *BBA-Bioenergetics* **2001,** *1503*, 96.
18. Barber, J.; Murray, J. W., *Philos. Trans. R. Soc. B-Biol. Sci.* **2008,** *363*, 1129.
19. Loll, B.; Kern, J.; Saenger, W.; Zouni, A.; Biesiadka, J., *Nature* **2005,** *438*, 1040.
20. Sproviero, E. M.; Gascon, J. A.; McEvoy, J. P.; Brudvig, G. W.; Batista, V. S., *J. Am. Chem. Soc.* **2008,** *130*, 6728.
21. Luber, S.; Rivalta, I.; Umena, Y.; Kawakami, K.; Shen, J. R.; Kamiya, N.; Brudvig, G. W.; Batista, V. S., *Biochemistry* **2011,** *50*, 6308.
22. Siegbahn, P. E. M., *Acc. Chem. Res.* **2009,** *42*, 1871.
23. Siegbahn, P. E. M., *Chem.-Eur. J.* **2008,** *14*, 8290.
24. Pantazis, D. A.; Ames, W.; Cox, N.; Lubitz, W.; Neese, F., *Angew. Chem. Int. Ed.* **2012,** *51*, 9935.
25. Hsiao, Y. W.; Tao, Y.; Shokes, J. E.; Scott, R. A.; Ryde, U., *Phys. Rev. B* **2006,** *74*.
26. Ryde, U., *Dalton Trans.* **2007**, 607.
27. Rehr, J. J.; Kas, J. J.; Prange, M. P.; Sorini, A. P.; Takimoto, Y.; Vila, F., *C. R. Phys.* **2009,** *10*, 548.
28. Umena, Y.; Kawakami, K.; Shen, J. R.; Kamiya, N., *Nature* **2011,** *473*, 55.

29. Mantel, C.; Chen, H. Y.; Crabtree, R. H.; Brudvig, G. W.; Pécaut, J.; Collomb, M. N.; Duboc, C., *ChemPhysChem* **2005,** *6*, 541.
30. Mantel, C.; Baffert, C.; Romero, I.; Deronzier, A.; Pécaut, J.; Collomb, M. N.; Duboc, C., *Inorg. Chem.* **2004,** *43*, 6455.
31. Duboc, C.; Phoeung, T.; Zein, S.; Pécaut, J.; Collomb, M.-N.; Neese, F., *Inorg. Chem.* **2007,** *46*, 4905.
32. Oshio, H.; Ino, E.; Mogi, I.; Ito, T., *Inorg. Chem.* **1993,** *32*, 5697.
33. Hitomi, Y.; Ando, A.; Matsui, H.; Ito, T.; Tanaka, T.; Ogo, S.; Funabiki, T., *Inorg. Chem.* **2005,** *44*, 3473.
34. Towle, D. K.; Botsford, C. A.; Hodgson, D. J., *Inorg. Chim. Acta* **1988,** *141*, 167.
35. Strautmann, J. B. H.; DeBeer George, S.; Bothe, E.; Bill, E.; Weyhermueller, T.; Stammler, A.; Boegge, H.; Glaser, T., *Inorg. Chem.* **2008,** *47*, 6804.
36. Tenderholt, A.; Hedman, B.; Hodgson, K. O., PySpline: A modern, cross-platform program for the processing of raw averaged XAS edge and EXAFS data. In *X-Ray Absorption Fine Structure-XAFS13*, Hedman, B.; Painetta, P., Eds. 2007; Vol. 882, pp 105.
37. Ankudinov, A. L.; Rehr, J. J., *Phys. Rev. B* **1997,** *56*, R1712.
38. Rehr, J. J.; Kas, J. J.; Vila, F. D.; Prange, M. P.; Jorissen, K., *Phys. Chem. Chem. Phys.* **2010,** *12*, 5503.
39. George, G. N. *EXAFSPAK, SSRL, SLAC*, Stanford University: Stanford, CA, 2000.
40. Neese, F., *WIREs Comput Molec Sci* **2012,** *2*, 73.
41. Poiarkova, A. V.; Rehr, J. J., *Phys. Rev. B* **1999,** *59*, 948.
42. Roemelt, M.; Beckwith, M. A.; Duboc, C.; Collomb, M. N.; Neese, F.; DeBeer, S., *Inorg. Chem.* **2012,** *51*, 680.
43. Becke, A. D., *Phys. Rev. A* **1988,** *38*, 3098.
44. Perdew, J. P., *Phys. Rev. B* **1986,** *33*, 8822.
45. Pantazis, D. A.; Chen, X. Y.; Landis, C. R.; Neese, F., *J. Chem. Theory Comput.* **2008,** *4*, 908.
46. Weigend, F.; Ahlrichs, R., *Phys. Chem. Chem. Phys.* **2005,** *7*, 3297.
47. Klamt, A.; Schüürmann, G., *J. Chem. Soc. Perk. T. 2* **1993**, 799.
48. Lenthe, E. v.; Baerends, E. J.; Snijders, J. G., *J. Chem. Phys.* **1993,** *99*, 4597.
49. van Wüllen, C., *J. Chem. Phys.* **1998,** *109*, 392.
50. Grimme, S., *J. Comput. Chem.* **2006,** *27*, 1787.
51. Grimme, S., *J. Comput. Chem.* **2004,** *25*, 1463.
52. Grimme, S.; Antony, J.; Ehrlich, S.; Krieg, H., *J. Chem. Phys.* **2010,** *132*.

APPENDIX A

Explanation of BlueprintXAS Fitting Procedures

XAS Fitting:

For all XAS fits conducted using BlueprintXAS,[1,2] the background-subtracted, unnormalized data were used for fitting. Both the pre-edge and edge regions were fit simultaneously. For all fit components, the peak position, intensity, half-width at half-maximum, and Gaussian-Lorentzian mixing were allowed to float during fitting. For each fit, starting point values for all parameters were chosen by the program from a reasonable range of values input by the user prior to fitting.

The following equation was used for the edge fit component:

$$I0*\left((1-G0)*\left(\frac{1}{\pi}\tan^{-1}\left(\frac{x-O0}{W0}\right)+\frac{1}{2}\right)+\left(\frac{G0}{2}\right)*\left(1+erf\left(\frac{x-O0}{\left(W0/\sqrt{2\log(2)}\right)\sqrt{2}}\right)\right)\right)$$

where I, G, O and W represent the peak intensity, Gaussian-Lorentzian mixing, position, and half-width at half maximum, respectively. In the BlueprintXAS program notation, the above equation is as follows:

I0*((1-G0)*(1/pi*atan((x-O0)/W0)+1/2)+G0/2*(1+erf((x-

O0)/(W0/(sqrt(2*log(2)))*sqrt(2)))))

The equations for the remaining peaks were of the following form:

Peak 1

$$I0*I1*\left(\left(\frac{1-G1}{\pi*W1*\left(1+\left((x-O1)/W1\right)^2\right)}\right)+\left(\frac{G1*\sqrt{2\log(2)}}{W1*\sqrt{2\pi}}\right)\exp\left(-\frac{(x-O1)^2}{2*\left(W1/\sqrt{2\log(2)}\right)^2}\right)\right)$$

The expressions for all peaks are multiplied by the edge intensity, I0, for normalization purposes. The above equation in BlueprintXAS notation is:

I0*I1*((1-G1)/(pi*W1*(1+((x-O1)/W1)^2))+G1*(sqrt(2*log(2)))/(W1*sqrt(2*pi))*exp(-((x-O1)^2/(2*(W1/(sqrt(2*log(2))))^2))))

Peak 2

$$I0*I2*\left(\left(\frac{1-G2}{\pi*W2*\left(1+\left((x-O2-O1)/W2\right)^2\right)}\right)+\left(\frac{G2*\sqrt{2\log(2)}}{W2*\sqrt{2\pi}}\right)\exp\left(-\frac{(x-O2-O1)^2}{2*\left(W2/\sqrt{2\log(2)}\right)^2}\right)\right)$$

Here the position of peak 2 is relative to that of peak 1 (denoted by x-O2-O1 in the equation above). As such, the values given for O2 are not absolute energies as for peak 1, but values that indicate where peak 2 is in relation to peak 1. This is seen in the screen capture below, where the starting value of +2 for the variable O2 indicates that the starting position of peak 2 is 2 eV higher than that of peak 1:

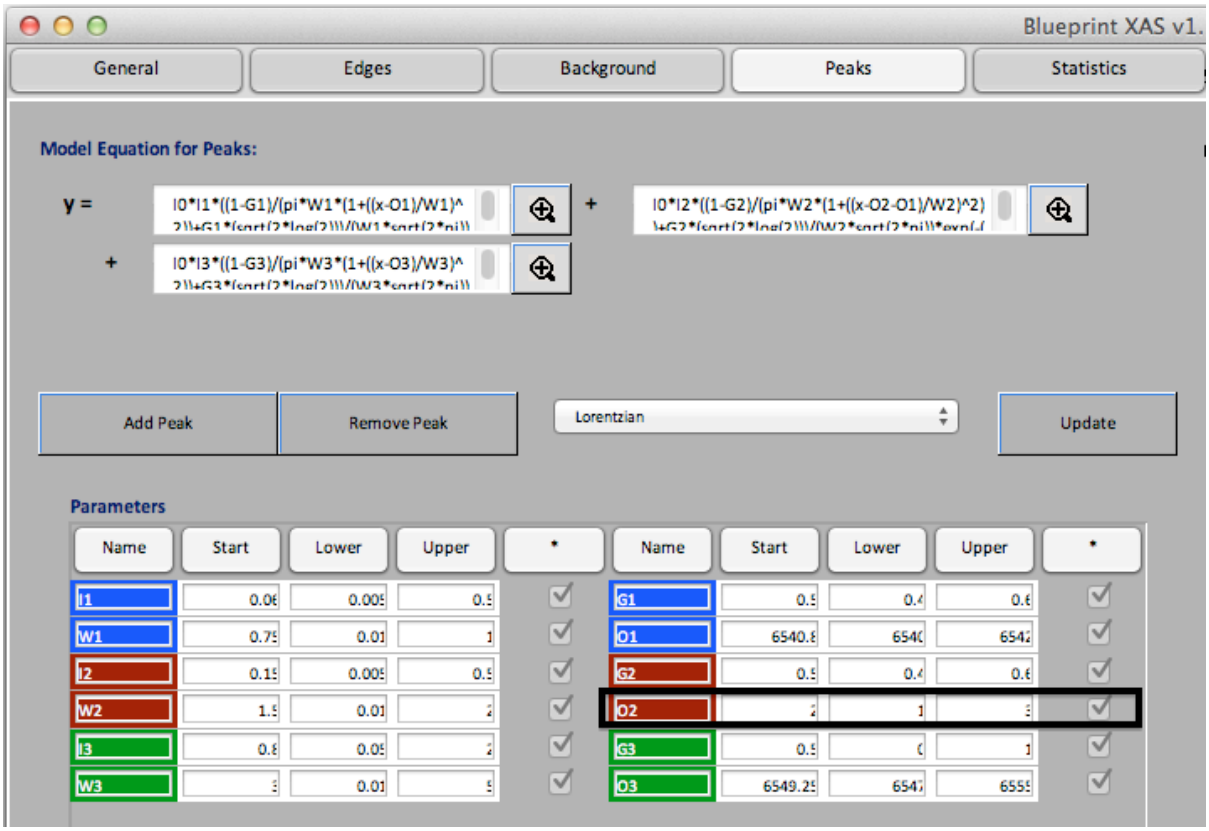

Figure A1. Screen capture of the "Peaks" input screen in the BlueprintXAS program. The variable that uses relative values for the position of Peak 2 is highlighted.

When inputting relative peak positions, positive values indicate higher relative positions, and negative values indicate lower relative positions.

XES Fitting:

For all the XES data fit in BlueprintXAS, the raw, unnormalized spectra were used for fitting using a protocol developed by Dr. Mario Delgado-Jaime. Both the main line and the valence to core region were fit simultaneously. For all fit components, the peak position, intensity, half-width at half-maximum, and Gaussian-Lorentzian mixing were allowed to float during fitting, and starting point values for all parameters were chosen by the program from a reasonable range of values input by the user prior to fitting.

The main line consists of three peaks of the following forms:

Edge 1

$$I9*I7*B8*\left(\left(\frac{1-G2}{\pi*W2*\left(1+\left((x-O2)/W2\right)^2\right)}\right)+\left(\frac{G2*\sqrt{2\log(2)}}{W2*\sqrt{2\pi}}\right)\exp\left(-\frac{(x-O2)^2}{2*\left(W2/\sqrt{2\log(2)}\right)^2}\right)\right)$$

Here I9 is the total area (main line + valence to core), I7 is the normalized valence to core area, and B8 is the normalized area of the main line peak represented as a multiple of the normalized valence to core area.

Edge 2

$$I9*I7*B6*\left(\left(\frac{1-G6}{\pi*W6*\left(1+\left((x-O6)/W6\right)^2\right)}\right)+\left(\frac{G6*\sqrt{2\log(2)}}{W6*\sqrt{2\pi}}\right)\exp\left(-\frac{(x-O6)^2}{2*\left(W6/\sqrt{2\log(2)}\right)^2}\right)\right)+B5$$

where B6 is the normalized peak area and B5 is an intensity offset to account for the background intensity in the raw data.

Edge 3

$$I9*(1-I7*(1+B8+B6))*\left(\left(\frac{1-G1}{\pi*W1*\left(1+\left((x-O1-O6)/W1\right)^2\right)}\right)+\left(\frac{G1*\sqrt{2\log(2)}}{W1*\sqrt{2\pi}}\right)\exp\left(-\frac{(x-O1-O6)^2}{2*\left(W1/\sqrt{2\log(2)}\right)^2}\right)\right)$$

Here the peak intensity is not an explicit variable, but is represented by differences of the other two main line peak areas and the valence to core area from the total area.

The valence to core region consists of a varying number of peaks all represented by equations similar to that of Edge 1. For clarity, the equations for the valence to core peaks in the fit of the $[Mn_2(IV)(\mu\text{-}O)_2(salpn)_2]$ dimer are shown below.

Peak 1

$$I9*I7*B1*\left(\left(\frac{1-G7}{\pi*W7*\left(1+\left((x-O7)/W7\right)^2\right)}\right)+\left(\frac{G7*\sqrt{2\log(2)}}{W7*\sqrt{2\pi}}\right)\exp\left(-\frac{(x-O7)^2}{2*\left(W7/\sqrt{2\log(2)}\right)^2}\right)\right)$$

where B1 is the area of Peak 1 represented as a fraction of the normalized total valence to core

area.

Peak 2

$$I9*I7*B3*\left(\left(\frac{1-G3}{\pi*W3*\left(1+\left((x-O3-O7)/W3\right)^2\right)}\right)+\left(\frac{G3*\sqrt{2\log(2)}}{W3*\sqrt{2\pi}}\right)\exp\left(-\frac{(x-O3-O7)^2}{2*\left(W3/\sqrt{2\log(2)}\right)^2}\right)\right)$$

where the position of Peak 2, O3, is relative to the position of Peak 1, O7.

Peak 3

$$I9*I7*B2*\left(\left(\frac{1-G8}{\pi*W8*\left(1+\left((x-O8-O9)/W8\right)^2\right)}\right)+\left(\frac{G8*\sqrt{2\log(2)}}{W8*\sqrt{2\pi}}\right)\exp\left(-\frac{(x-O8-O9)^2}{2*\left(W8/\sqrt{2\log(2)}\right)^2}\right)\right)$$

where the position of Peak 3, O8, is relative to the position of Peak 5, O9.

Peak 4

$$I9*I7*B4*\left(\left(\frac{1-G4}{\pi*W4*\left(1+\left((x-O4-O8-O9)/W4\right)^2\right)}\right)+\left(\frac{G4*\sqrt{2\log(2)}}{W4*\sqrt{2\pi}}\right)\exp\left(-\frac{(x-O4-O8-O9)^2}{2*\left(W4/\sqrt{2\log(2)}\right)^2}\right)\right)$$

where the position of Peak 4, O4, is relative to the position of Peak 3, O8.

Peak 5

$$I9*I7*(1-B1-B2-B3-B4)*\left(\left(\frac{1-G9}{\pi*W9*\left(1+\left((x-O9)/W9\right)^2\right)}\right)+\left(\frac{G9*\sqrt{2\log(2)}}{W9*\sqrt{2\pi}}\right)\exp\left(-\frac{(x-O9)^2}{2*\left(W9/\sqrt{2\log(2)}\right)^2}\right)\right)$$

where the area of Peak 5 is calculated by the differences of the areas of Peaks 1-4 from the total valence to core area.

References

1. Delgado-Jaime, M. U.; Kennepohl, P., *J. Synchrot. Radiat.* **2010,** *17*, 119.
2. Delgado-Jaime, M. U.; Mewis, C. P.; Kennepohl, P., *J. Synchrot. Radiat.* **2010,** *17*, 132.

APPENDIX B

Example FEFF 9 Input Files and Procedure for Running DMDW Calculations

FEFF 9 input file for a calculation using the Correlated Debye model:

```
* This feff9 input file was modified from that generated by dym2feffinp

TITLE KMnO4 ORCA OPT Structure
TITLE dymfile name:  Need to fix
TITLE absorbing atom:   0

EDGE      K
S02       1.0000

*             pot    xsph     fms   paths  genfmt  ff2chi
CONTROL         1       1       0       1       1       1
PRINT           1       0       0       0       0       0

RPATH       5.0
EXAFS      12.0

DEBYE     10.0  1000.0

*SIG2 0.0025

CRITERIA 5 5

NLEG 3


POTENTIALS
    0   25   Mn
    1    8    O

ATOMS
    0.00000    0.00000    0.00000    0   Mn  0.00000    0
   -0.47842   -0.51443   -1.45285    1    O  1.61378    1
   -0.56920   -0.99781    1.13354    1    O  1.61385    2
    1.61260    0.02119    0.06096    1    O  1.61389    3
   -0.56936    1.48864    0.25529    1    O  1.61412    4
END
```

Figure B1. Example FEFF 9 Input File for a calculation using the Correlated Debye model.

FEFF 9 input file for a calculation using the Dynamical Matrix (DM) model:

```
* This feff9 input file was modified from that generated by dym2feffinp

TITLE KMnO4 ORCA OPT Structure
TITLE dymfile name:  Need to fix
TITLE absorbing atom:   0

EDGE      K
S02       1.0000

*             pot    xsph     fms   paths  genfmt  ff2chi
CONTROL         1       1       0       1       1       1
PRINT           1       0       0       0       0       0

RPATH       5.0
EXAFS      12.0

DEBYE     10.0  1000.0  5  feff.dym  6  0  1

*SIG2 0.0025

CRITERIA 5 5

NLEG 3


POTENTIALS
    0   25   Mn
    1    8    O

ATOMS
    0.00000    0.00000    0.00000    0   Mn  0.00000    0
   -0.47842   -0.51443   -1.45285    1    O  1.61378    1
   -0.56920   -0.99781    1.13354    1    O  1.61385    2
    1.61260    0.02119    0.06096    1    O  1.61389    3
   -0.56936    1.48864    0.25529    1    O  1.61412    4
END
```

Figure B2. Example FEFF 9 Input File for a calculation using the Dynamical Matrix model.

Explanation of the FEFF input file using the DM model:

The calculation using the DM model requires a .dym file (here called feff.dym) that contains the numerical frequencies from the ORCA frequency calculation. The DEBYE card is structured as follows (for more information see FEFF 9 manual):

DEBYE Temp Debye_Temp [DW_Opt [dymFile DMDW_Order DMDW_Type DMDW_Route]]

Thus the input file for the calculation in Figure B2 uses a temperature of 10 K, and a Debye temperature of 1000 K. The value of 5 for Dym_Opt indicates that the DM model should be used to calculate DW factors (using the DMDW code and the dymfile file feff.dym).

DMDW_Order value of 6 indicates that a Lanczos recursion order of 6 should be used (well converged results are usually obtained for DMDW_Order values between 6 and 10, default value is 2). DMDW_Type value of 0 indicates that the type of the DW calculation should be Parallel s^2 (default). DMDW_Route selects which paths should be calculated independently in the DMDW module. DMDW_Route values are as follows:

1 = all SS paths from the photoabsorber.

2 = all SS + all DS paths from the photoabsorber.

3 = all SS + all DS + all TS paths from the photoabsorber

11 = all SS paths

12 = all SS + all DS paths

13 = all SS + all DS + all TS paths

For the EXAFS calculations conducted in Chapter 5, using DMDW_Route values of 2 or 3 did not significantly affect the resulting EXAFS, as the most significant contributions to the overall EXAFS were from single scattering paths.

Creating the .dym file and running the FEFF calculation using the DM model:

The ORCA frequency calculation is run by including "! NumFreq" in the header of the ORCA input file. The relevant files from the completed frequency calculation are the .out and .hess files (the .hess file contains the ORCA hessian that has all of the numerical frequencies from the calculation).

The numerical frequencies in the ORCA hessian are converted into a format similar to that of the FEFF 9 .dym file using a bash script written by Dr. William Ames called "orca2dym". When in the directory where the .hess and .out files are located, the script is executed in the command line as follows:

orca2dym examplefile.hess examplefile.out

In order for the script to be properly executed, the entire path file of the orca2dym program was typed into the command line (e.g. if the orca2dym program is located on the Desktop: /Users/beckwith/Desktop/orca2dym examplefile.hess examplefile.out). However if the script is correctly pathed in the computer, the entire path need not be explicitly typed. Upon completion of the script, a .dym file is generated with the same filename as the .hess and .out files (e.g. examplefile.dym) that contains the xyz coordinates from the ORCA output file and the numerical frequencies from the ORCA hessian.

The frequency blocks in the .dym file generated by orca2dym are not in the correct order for usage with the FEFF 9 DMDW code, and the FEFF calculations will not run properly unless the frequency blocks are in the correct order. However, there is an executable file in the installation folder of the JFEFF program called "dym2feffinp" that uses the information in the orca2dym generated .dym file to create a new adjusted .dym file that has the correct ordering of frequency blocks. In addition to the new .dym file, dym2feffinp also creates a FEFF .inp file. To execute the script, the following is typed in the command line:

dym2feffinp --d newfile.dym examplefile.dym

As with orca2dym, the entire path for the dym2feffinp program was typed into the command line. This generates an adjusted .dym file called newfile.dym and also a feff.inp file that can be used in FEFF 9. Figure B4 in the next section shows a screenshot of part of the adjusted feff.dym file used in the FEFF calculation for the input file in Figure B2. If desired, the name of the new feff.inp file can be modified by typing the following:

dym2feffinp --d newfile.dym --f newfile2.inp examplefile.dym

which creates a FEFF input file newfile2.inp along with newfile.dym.

In the coordinates block of the adjusted .dym and .inp files, the origin of the coordinate system

is chosen to be the first atom in the xyz coordinate block given in examplefile.dym. This same atom is also automatically made to be the absorbing atom and given the potential index 0. To center the feff.inp file on a different absorbing atom, type the following:

dym2feffinp --d newfile.dym --c iAbs examplefile.dym

Here iAbs is the number corresponding the desired central atom (e.g. typing --c 2 will center the molecule on the second atom in the xyz coordinate block and make atom 2 the new absorbing atom). In this case, newfile.dym and newfile.inp will have the xyz coordinates in a different order than in the unadjusted examplefile.dym, because the molecule is now centered on the new photoabsorber, atom 2. Because of this reordering of coordinates, the assigned potential indices may be different as well (see Figure B3).

```
POTENTIALS
    0    8    O
    1   25   Mn
    2    8    O

ATOMS
    0.00000    0.00000    0.00000    0    O  0.00000    0
   -1.61260   -0.02119   -0.06096    1   Mn  1.61389    1
   -2.18181   -1.01900    1.07258    2    O  2.63611    2
   -2.09102   -0.53562   -1.51381    2    O  2.63645    3
   -2.18196    1.46745    0.19432    2    O  2.63669    4
END
```

Figure B3. Potential indices and xyz coordinates in the feff.inp file generated by dym2feffinp using the coordinates and numerical frequencies in the original dym file for $KMnO_4$, but specifying atom 2 as the photoabsorber. Note that the atoms are ordered such that the coordinates for the new photoabsorber appear in the first line in the xyz coordinates, regardless of the order of the original xyz coordinates.

The FEFF 9 calculations using the DMDW code were run using the program JFEFF. In order for the calculations to run correctly, it is essential that the feff.dym file be in the same directory as the corresponding feff.inp file.

Important Note: The newly generated feff.inp file does not automatically incorporate the necessary keywords in the DEBYE card needed to run the calculation using the Dynamical Matrix model (Figure B2), therefore the keywords in the feff.inp file need to be adjusted for each individual calculation. In addition, the atom order in the xyz coordinates must match in both the feff.inp file and the feff.dym file, with the photoabsorber located at the origin, or the calculation will not run correctly. This means that for molecules with multiple photoabsorbers, such as the Mn dimers in Chapter 5, two separate feff.dym and feff.inp files were needed, one each for the two Mn centers (e.g. Mn1.dym and the corresponding Mn1.inp both centered on photoabsorber Mn1, as well as Mn2.dym and the corresponding Mn2.inp both centered on photoabsorber Mn2).

Structure of the feff.dym file used for the FEFF 9 DMDW calculations:

Figure B4 shows a screenshot of part of the feff.dym file used in the FEFF calculation for the input file in Figure B2. The feff.dym file is structured as follows:

Line 1 = Dynamical matrix file type (default = 1). Cannot currently be modified.

Line 2 = Number of atoms in the system

Following Lines (in order) = Atomic numbers, Atomic masses (amu), Atomic xyz coordinates (in Bohr), and the Dynamical matrix in atom pair block format (atomic units) that contains the numerical frequencies from the ORCA calculation.

```
  1
  5
 25
  8
  8
  8
  8
 54.940000
 15.999000
 15.999000
 15.999000
 15.999000
  0.00000000    0.00000000    0.00000000
 -0.90408300   -0.97213800   -2.74548500
 -1.07564000   -1.88558800    2.14207200
  3.04738000    0.04004100    0.11519800
 -1.07593100    2.81312200    0.48241900
  1    1
 6.545460E-01  2.980000E-04  1.090000E-04
 2.300000E-04  6.540150E-01 -8.550000E-04
-8.250000E-04 -9.100000E-05  6.530510E-01
  1    2
-8.777900E-02 -2.901300E-02 -8.195700E-02
-2.920500E-02 -9.203400E-02 -8.856000E-02
-8.258200E-02 -8.842100E-02 -3.105490E-01
  1    3
-9.915500E-02 -6.746500E-02  7.624400E-02
-6.720600E-02 -1.786040E-01  1.341120E-01
 7.659600E-02  1.344310E-01 -2.130370E-01
  1    4
-3.686650E-01 -3.696000E-03 -1.156400E-02
-4.134000E-03 -6.063400E-02  6.900000E-05
-1.045100E-02 -4.060000E-04 -6.114300E-02
  1    5
-9.896100E-02  1.002460E-01  1.711300E-02
 1.003570E-01 -3.228300E-01 -4.495100E-02
 1.709500E-02 -4.573300E-02 -6.856800E-02
  2    1
-8.829100E-02 -2.731300E-02 -8.260300E-02
-2.778600E-02 -9.287400E-02 -8.861000E-02
-8.543500E-02 -9.006100E-02 -3.109150E-01
  2    2
 7.486600E-02  3.202100E-02  9.578900E-02
 3.245500E-02  8.036600E-02  1.029260E-01
 9.892800E-02  1.042860E-01  3.338970E-01
  2    3
 1.111400E-02  8.757000E-03  3.700000E-03
 8.877000E-03  1.680600E-02  9.647000E-03
 2.504000E-03  8.020000E-03 -2.713400E-02
  2    4
-8.817000E-03 -8.857000E-03 -2.519500E-02
-8.220000E-03  4.989000E-03  1.370000E-04
-2.356000E-02  1.620000E-04  5.102000E-03
  2    5
 1.115300E-02 -4.547000E-03  8.306000E-03
-5.298000E-03 -9.135000E-03 -2.403200E-02
 7.693000E-03 -2.230900E-02 -8.020000E-04
  3    1
-1.012120E-01 -6.694000E-02  7.623600E-02
-6.666700E-02 -1.805550E-01  1.332390E-01
 7.807700E-02  1.370950E-01 -2.119220E-01
  3    2
 1.111900E-02  9.005000E-03  2.503000E-03
 8.834000E-03  1.691000E-02  7.985000E-03
 3.639000E-03  9.540000E-03 -2.730400E-02
  3    3
 8.962400E-02  7.779400E-02 -8.841100E-02
 7.760800E-02  1.818710E-01 -1.547170E-01
-9.044500E-02 -1.589050E-01  2.191590E-01
  3    4
-1.181700E-02 -1.726700E-02  1.897400E-02
-1.606400E-02  5.137000E-03 -1.552000E-03
 1.763200E-02 -1.391000E-03  7.793000E-03
```

Figure B4. Screenshot of part of the feff.dym file used for the DMDW calculation corresponding to the input file in Figure B2. The feff.dym file contains the number of atoms, atomic numbers and masses, xyz coordinates, and the dynamical matrix (in atom pair block format) with the numerical frequencies from the ORCA frequency calculation.